UNIVERSITÀ DEGLI STUDI DI MILANO

SCUOLA DI DOTTORATO
FISICA, ASTROFISICA E FISICA APPLICATA

DIPARTIMENTO DI FISICA

CORSO DI DOTTORATO DI RICERCA IN
FISICA, ASTROFISICA E FISICA APPLICATA
CICLO XXIII

Nuclear Collective Modes at finite temperature as a probe of nuclear structure and dynamics

Settore Scientifico disciplinare FIS/04

Supervisore: Prof. Franco Camera

Coordinatore: Prof. Marco Bersanelli

Tesi di Dottorato di:

Anna Maria Corsi

Anno Accademico 2009-2010

Contents

Introduction

The framework of this Thesis is the study of nuclear structure and reaction dynamics through gamma spectroscopy measurements in fusion-evaporation reactions.

Soon after heavy ions collide, a variety of single and collective modes of the nucleons are induced in the complete fusion channel and lead to the formation of a thermalized system known as compound nucleus (CN). One of these modes, excited by differences of local neutron over proton densities, is particularly strong and coherent when projectile and target have a different N/Z ratio, with N and Z being the neutron and proton numbers, respectively. It is known as Dynamical Dipole (DD) since it appears as a collective dipolar oscillation that is a source of γ emission.

Due to their coherence, the last degrees of freedom to attain equilibration in the CN are the collective ones, i.e. the Giant Resonances. The γ emission associated with the decay of the Giant Resonances is a probe of the bulk properties of the nuclei. It depends on the structure of initial and final states and on the selection rules associated with the specific transition. In the case of isovector transitions the selection rules for isospin quantum number I prescribe $I_{final}=I_{initial}\pm 1$, in self-conjugate nuclei. Therefore, γ decay in self-conjugate nuclei mediated by the isovector Giant Dipole Resonance (GDR) is forbidden from an $I_{initial}=0$ to an $I_{final}=0$ state.

The detailed study of GDR spectral shape and multiplicity is a very good tool to study the role of the nuclear interaction in compound nucleus formation and decay as will be discussed in this Thesis with two examples, namely a measurement of DD gamma emission and GDR decay from an I=0 CN.

In fact DD oscillation is ruled by the symmetry term of the nuclear force that drives the proton and neutron densities toward a configuration that minimizes the potential energy of the system. The hindrance of GDR gamma decay from a self-conjugate CN (with I=0) is due to a partial restoration of isospin symmetry at high nuclear temperature (T), since the excited compound nucleus lifetime is too short for the relatively weak Coulomb interaction to mix states with different isospin. In fact the typical timescale for isospin mixing in the CN under study in this Thesis, ^{80}Zr at T$\sim$ 2 MeV, is $\sim 6\ 10^{-20}$ s as deduced from the value of the Coulomb spreading width, while the one for CN decay is $\sim 3\ 10^{-21}$ s.

In this Thesis two experiments will be discussed, both performed at Laboratori Nazionali di Legnaro (LNL) with the GARFIELD-HECTOR apparatus. This detection apparatus includes a γ detector with good efficiency and timing performance, a detector for evaporation residues in order to select the fusion channel and a detector for light charged particles accounting for the other components of the decay. The first one is the HECTOR array of

BaF_2 scintillators [1], the second ones are the PHOSWICH scintillators [2] and the third one is the GARFIELD ΔE-E array of microstrip gas chambers coupled to CsI scintillators [3].
In this kind of measurements the system of interest has to be studied together with a reference system whose γ decay is expected to be well reproducible by the standard Statistical Model [4]. The two systems have to be as similar as possible as far as mass, excitation energy and spin population are concerned. This in order to be able to extend the Statistical Model calculation tuned on the reference system to the one of interest.
In the case of DD measurement, the reaction of interest was ^{16}O+^{116}Sn while the reference was ^{64}Ni+^{68}Zn, both systems producing ^{132}Ce* CN. Results of the Statistical Model analysis of the γ decay of ^{132}Ce* produced in ^{64}Ni+^{68}Zn reaction [1] are the basis for the subsequent analysis of DD, that can be pinned down only by subtracting the statistical contribution from the measured γ spectrum. Beam energy dependence is closely related to the onset and damping of DD oscillation as a collective mode. As theoretical calculations confirm, it exists in a range of beam energies where the collective oscillation is the preferred mechanism to restore N/Z balance, and, consequently, a stronger γ emission is expected. From the experimental point of view this allows an improved sensitivity to the restoring force. In this Thesis the results obtained with the ^{16}O+^{116}Sn reaction at beam energies of 8.1, 12 and 15.6 MeV/u will be presented together with theoretical calculations of γ emission performed applying the Bremsstrahlung formula to the dipolar oscillation calculated within the Boltzmann-Nordheim-Vlasov approach [5, 6, 7]. Details on the calculation of γ multiplicity, spectral shape and angular distribution will be presented. The angular distribution, besides being a further signature of the dipolar nature of this emission mechanism, is also sensitive to the timescale of DD oscillation and therefore of the charge equilibration process [8].
In the case of isospin mixing measurement, the system under study is the self-conjugate nucleus ^{80}Zr* produced at E*=83 MeV (corresponding to T$\sim$2 MeV) with the fusion reaction ^{40}Ca+^{40}Ca. The reference system is ^{81}Rb* produced with ^{37}Cl+^{44}Ca fusion reaction. For this analysis a modified version of standard Statistical Model calculation is demanded. It has been implemented by [9, 10] and it divides according to isospin the phase-space population in two classes that are mixed according to the Coulomb spreading width given as input of the calculation. Theoretical models predict a decrease of isospin mixing with increasing CN temperature [11, 12] and existing measurements [13] confirm a stronger hindrance of first step γ decay from the I=0 CN due to the selection rules for E1 transitions forbidding I=0 → I=0 transitions. Up to now, measurements have been done in systems with mass $A\leq60$, so the aim of the measurement with a heavier system is to investigate how isospin mixing depends on A and Z of the nucleus. Going to heavier systems keeping N=Z also involves approaching the proton drip line (beginning at N=37 for Z=40) where nuclei cannot be populated at zero temperature. In this Thesis, data reductions and Statistical Model analysis will be presented for both systems ^{80}Zr* and ^{81}Rb*.
In summary, in Chapt. 1 and 2 we will describe the physics cases and in Chapt. 3 we will describe the GARFIELD-HECTOR array. Following, in Chapt. 4 we will presents the results of the measurement and calculations of DD emission and the same in Chapt.

5, 6, 7 for the measurement of isospin mixing. In the Appendixes we will give some more details on the BNV simulation and on the Statistical Model calculation.

Chapter 1

Isospin equilibration in fusion reactions: Dynamical Dipole mode

1.1 Heavy-ion fusion reactions

Heavy-ion ($A \geq 4$) fusion reactions are the most efficient reaction mechanism to produce highly excited compound nucleus (CN), i.e. a long-lived system at thermal equilibrium (see Sect. 2.3) whose features and decay mode do not depend on the entrance channel of the reaction except for energy, parity and angular momentum conservation. In heavy-ion fusion a deep potential well is built up from the overlap of the potentials of the two reaction partners. Inside this well the kinetic energy carried by the projectile is dissipated in collisions between nucleons originating from different fragments (projectile or target), until thermal equilibrium is achieved. The equilibrium configuration corresponds to the one that minimizes the energy of the system as far as shape and isospin density are concerned.
From this picture it can be deduced that the complete fusion (i.e. leading to CN formation) cross section depends simultaneously on:

- incoming kinetic energy of the projectile
- mass and charge asymmetry between projectile and target
- impact parameter of the collision

There is a linear relation between the square of the maximum angular momentum built up in complete fusion and kinetic energy in the center of mass of the colliding system, as is illustrated in Fig. 1.1. This relation holds up to a given angular momentum beyond which the fission barrier becomes smaller than the neutron binding energy (typically 8 MeV for nuclei in the valley of β stability) and fission becomes the preferred decay mode. This value of the angular momentum depends only on A and Z of the nucleus and is plotted in Fig. 1.2 for nuclei in the valley of stability and for N=Z nuclei (deviating from the valley of stability for $A>40$).

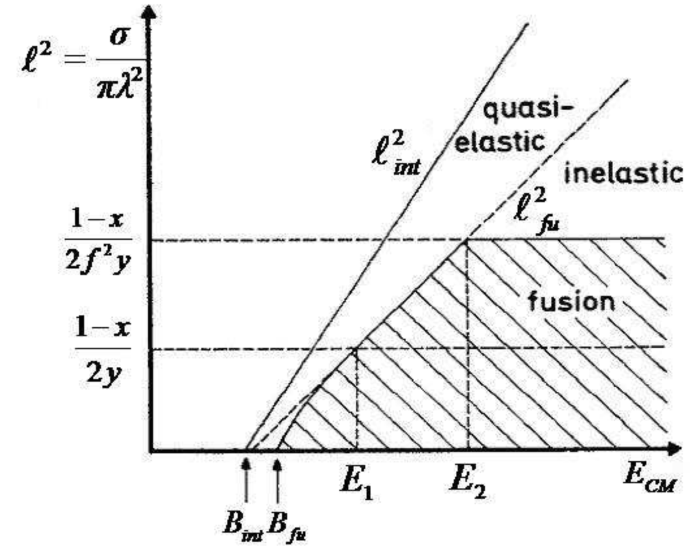

Figure 1.1: Relation between center-of-mass energy and maximum angular momentum ℓ attained by the reaction product. Maximum angular momentum for fusion (including complete fusion and fusion-fission reactions) increases up to E_2 where it saturates [14].

1.2 Dynamical Dipole mode in fusion reactions

When a heavy-ion reaction is performed, the neutron excess of the projectile and the target may be different. When the two heavy ions interact, the density of neutron excess changes very rapidly in time until it reaches an equilibrium value. This value is a property of the compound nucleus and corresponds to the configuration that minimizes the energy of the system. This process known as charge or N/Z equilibration is particularly relevant if the colliding nuclei have a different N/Z ratio. In this case, it has been predicted that the equilibration should take place with a collective oscillation. Since 1993, several experiments [16, 17, 18, 19, 20, 21] have measured an extra yield in γ emission that has been associated with this pre-equilibrium dipole mode and named Dynamical Dipole emission. The extra yield can be pinned down by comparing the γ decay from similar CN produced with and without N/Z asymmetry in the entrance channel. An alternative way to account for N/Z asymmetry between projectile and target is to define the dipole moment D(t=0) of the system when the colliding nuclei (approximated with rigid spheres of radius $r=r_0(A_p^{1/3}+A_t^{1/3})$ get in contact [6]:

$$D(t=0) = \frac{NZ}{A}|X_Z(t=0) - X - N(t=0)| = \frac{r_0(A_p^{1/3} + A_t^{1/3})}{A} Z_p Z_t |\frac{N_t}{Z_t} - \frac{N_p}{Z_p}| \quad (1.1)$$

where X_N and X_P are the proton and neutron coordinates in the center-of-mass reference frame and the subscripts *p, t* refer to projectile and target, respectively. The value of D

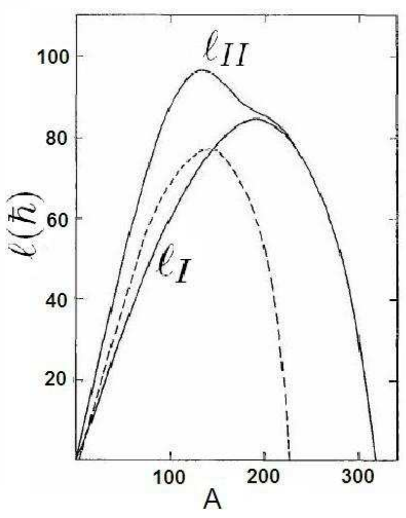

Figure 1.2: The maximum angular momentum that a stable nucleus can support surviving fission is shown with a dashed line. It corresponds to the value of the angular momentum where the height of the fission barrier is equal to 8 MeV, corresponding to the average neutron binding energy. The barrier vanishes at the continuous line labeled ℓ_{II}, while for angular momentum higher than the one labeled with ℓ_I the nucleus undergoes a transition to a triaxial shape [15].

in the systems where DD emission has been studied ranges from 8.4 fm in ^{16}O+^{98}Mo [17] to 22.1 fm in ^{40}Ca+^{100}Mo [16].
Fig. 1.3 shows the first evidence of DD emission obtained for the N/Z asymmetric ^{40}Ca+^{100}Mo reaction (D=22.1 fm), compared with the N/Z symmetric one ^{36}S+^{104}Pd (D=0.5 fm).

The extra-gamma yield is usually expressed in terms of the increase relative to the statistical decay. If we take a and b as the integrals of the γ yield for the N/Z asymmetric and symmetric reaction, the increase is defined as:

$$Increase = \frac{a-b}{b} \tag{1.2}$$

The increase due to DD emission has been measured up to now for the systems listed in Tab. 1.1.

Recently, also the angular distribution of the γ-ray emission produced by DD oscillation has been measured [19, 21]. In both measurements the angular distribution displays a maximum at θ=90° with respect to the beam axis. This is in agreement with the theoretical models predicting that the DD initially is preferentially oriented along the beam axis and then performs a rotation with an angular momentum depending on the relative velocity and impact parameters. As can be intuitively inferred from Fig. 1.4, large

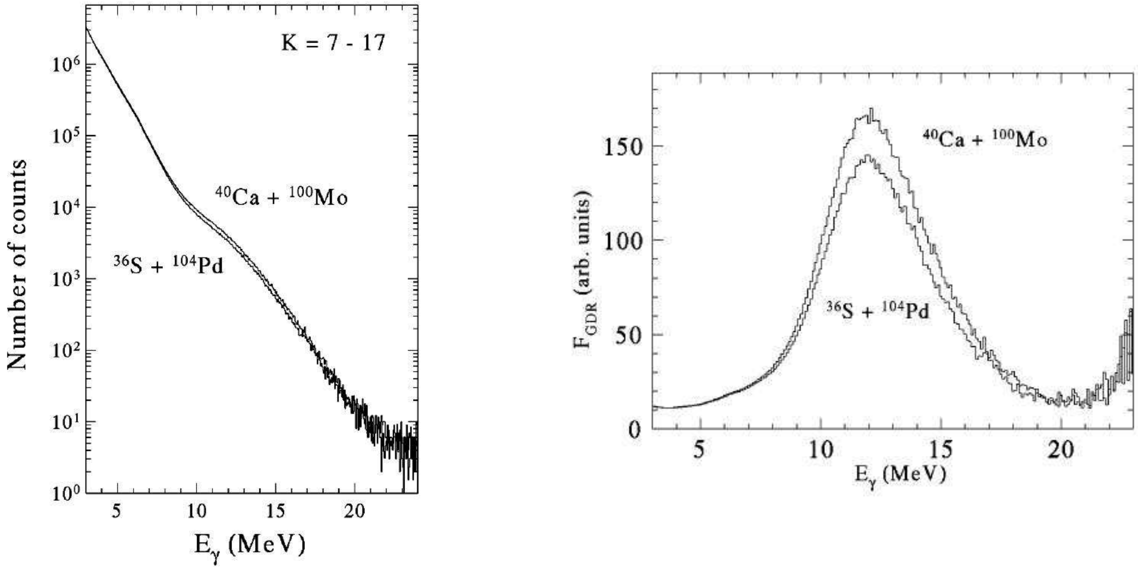

Figure 1.3: γ spectrum obtained from the events with multiplicity 7-17 of γ detected (left) and linearized plot of the measured γ spectrum [16]. The different yield between the N/Z asymmetric reaction ^{40}Ca+^{100}Mo and the N/Z symmetric one ^{36}S+^{104}Pd is associated with DD emission.

angles with respect to the beam axis are probed mostly in a peripheral collision or in the latter stages of a DD oscillation, when the γ-emission probability is reduced. Details and examples of how the angular distribution can be theoretically predicted will be given in Sect. 1.3 and Chapt. 4.

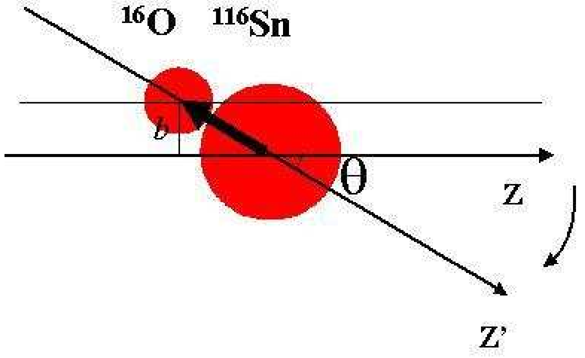

Figure 1.4: Pictorial view of the fusion reaction: the projectile ^{16}O impinges on the target ^{116}Sn with a given impact parameter b. For impact parameter b>0 a finite angular momentum is transferred to the system.

reaction	E_{beam}(MeV/u)	D(fm)	increase	Ref.
^{40}Ca+^{100}Mo	4.5	22.1	0.16	[16]
^{36}S+^{104}Pd	4.0	0.5	(8-18 MeV)	
^{16}O+^{98}Mo	8.1	8.4	0.36	[17]
^{48}Ti+^{64}Ni	5.0	5.2	(8-20 MeV)	
^{32}S+^{100}Mo	6.1	18.2	0.016	[18]
^{36}S+^{96}Mo	6.7	1.7	(8-21 MeV)	
^{32}S+^{100}Mo	9.3	18.2	0.25	[18]
^{36}S+^{96}Mo	8.9	1.7	(8-21 MeV)	
^{36}Ar+^{96}Zr	16.0	20.6	0.138	[19]
^{40}Ar+^{92}Zr	15.0	4.0	(8-21 MeV)	
^{16}O+^{116}Sn	8.1	8.6	0.08	[21]
^{64}Ni+^{68}Zn	4.7	1.2	(10-22 MeV)	
^{16}O+^{116}Sn	15.6	8.6	0.11	[21]
^{64}Ni+^{68}Zn	7.8	1.2	(10-22 MeV)	
^{16}O+^{116}Sn	12	8.6	0.16	Preliminary,
^{64}Ni+^{68}Zn	6.2	1.2	(10-22 MeV)	this work

Table 1.1: The systems for which DD emission has been measured are listed in the first column and are followed by the beam energy of the reaction and the dipole moment D defined as in Eq. 1.1. The increase of γ emission associated to DD mechanism is presented in the third column and followed by the reference.

Several models have been developed to describe Dynamical Dipole emission, both statistical [16] and dynamical. In particular, semi-classical transport models have been successfully developed in recent years to describe heavy-ion nuclear reactions at intermediate and high energies. These are, for example, Boltzmann-Nordheim-Vlasov (BNV) model [6], Time-Dependent Hartree-Fock model [22, 23] and Constrained Molecular Dynamics model [24]. In the next section, we will focus on BNV model and make some preliminary discussion on DD features based on results obtained with a numerical simulation where this model is implemented.

1.3 BNV simulation of fusion dynamics

The reaction dynamics within BNV model is described in a Stochastic Mean Field approach, extension of the microscopic Boltzmann-Nordheim-Vlasov transport equation. Nuclear dynamics follows Boltzmann-Langevin equation, which includes in a self-consistent way the mean field (U) and two-body collisions (via the collision integral I_{coll}) [6].

$$\frac{\partial f(\vec{r},\vec{p},t)}{\partial t} = -\frac{\partial f(\vec{r},\vec{p},t)}{\partial \vec{r}}\frac{\vec{p}}{m} + \frac{\partial f(\vec{r},\vec{p},t)}{\partial \vec{p}}\frac{\partial U}{\partial \vec{r}} - \frac{\partial f(\vec{r},\vec{p},t)}{\partial \vec{r}}\frac{\partial U}{\partial \vec{p}} + I_{coll}[f(\vec{r},\vec{p},t)] \qquad (1.3)$$

The collision integral is calculated using in-medium reduced nucleon-nucleon cross sections. It depends on nucleon isospin as well as energy and angle of the collision as parameterized in [25, 26]. The mean field is built from Skyrme forces; details on the parameterization of the symmetry term will be given in Subsect. 1.3.1.

The solution of Boltzmann-Langevin equation is the one-body distribution $f(\vec{r}, \vec{p}, t)$ for a system of A nucleons. This is defined with the technique of test particles, consisting in representing each nucleon with a set of N_{test} test particles in order to achieve more continuity in the nucleon distribution within the nuclear volume. The resulting nucleon distribution is obtained as the sum on $N_{test}A$ distributions that are the product of a Dirac δ in momentum space and a Gaussian $G(\vec{r})$ in real space.

$$f(\vec{r},\vec{p},t) = \frac{1}{N_{test}}\sum_{i=1}^{N_{test}A} G(\vec{r}-\vec{r}_i(t))\delta(\vec{p}-\vec{p}_i(t)) \qquad (1.4)$$

Macroscopic quantity as the dipole moment of the dinuclear system D(t) are calculated for each simulated event at each time step t averaging over all nucleons with the function $f(\vec{r},\vec{p},t)$ and then normalized to obtain a result that does not depend on N_{test} (see Fig. 1.5, left panel). The spiral evolution of the dipole moment in phase space (see Fig. 1.5, central panel) is a signature of the collective character of the DD oscillation. The γ emission associated with the DD mode is calculated with the Bremsstrahlung formula [27]:

$$\frac{dP}{dE_\gamma} = \frac{2e^2}{3\pi\hbar c^3 E_\gamma}(\frac{NZ}{A})^2|D''(\omega)|^2 \qquad (1.5)$$

where $D''(\omega) = \int_{t_0}^{t^{max}} D''(t)e^{i\omega t}dt$ is the Fourier transform of the dipole acceleration $D''(t)$. An example of γ spectrum obtained with this approach is plotted in the right panel of Fig. 1.5. The times t_0 and t_{max} correspond to the onset and the damping of the collective oscillation and have to be evaluated event by event.

Within Bremsstrahlung approach we can evaluate the time evolution of the emission probability for each time interval centered at t_i, corresponding to a mean orientation Φ_i of the dipole axis with respect to the beam axis. The rotation of the dipole axis can be determined from the nucleon distribution $f(\vec{r}, \vec{p}, t)$ and depends mainly on the impact parameter and the relative velocity of projectile and target. The instant emission probability is $P(t) = \int_{t_0}^{t^{max}} |D(t)''|^2 dt/P_{tot}$, with P_{tot}=P(t_{max}), and the probability of emission for the i^{th} interval becomes β_i=P(t_i)-P(t_{i+1}). The time evolution of cos(Φ) and P(t) for

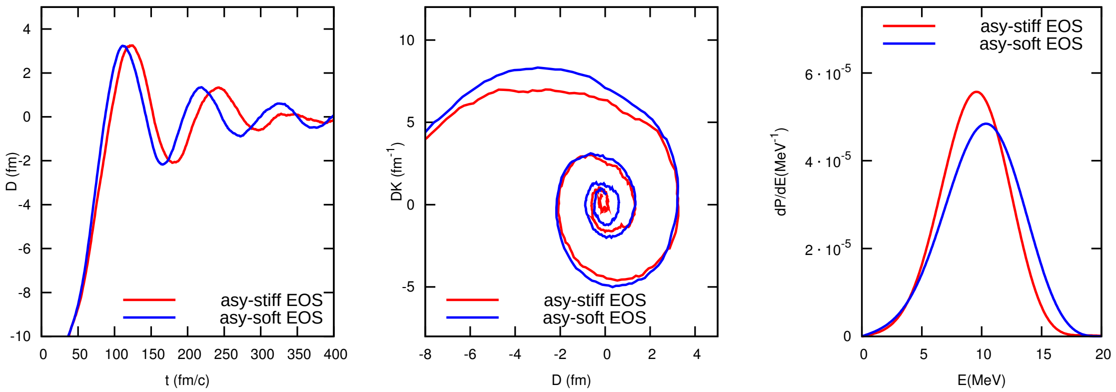

Figure 1.5: Left and center: dipole moment evolution with time and in phase space from a BNV simulation for a ^{16}O+^{116}Sn reaction at projectile energy 15.6 MeV/u and impact parameter 4 fm. Right: γ-emission probability calculated with the Bremsstrahlung formula as described in the text.

the system ^{132}Sn+^{58}Ni are plotted in the left panels Fig. 1.6.
These ingredients are necessary to properly evaluate the angular distribution. The angular distribution of the photons emitted by an oscillating dipole is:

$$W(\theta) = \frac{3}{2}(1 - P_2(cos(\theta))) \tag{1.6}$$

where P_2(x) is the second-order Legendre Polynomial. If the dipole axis is rotating with respect to a fixed axis (e.g. the beam axis), the resulting angular distribution with respect to the beam axis is smeared and becomes:

$$W(\theta) = \frac{3}{2}(1 - a_2 P_2(cos(\theta))) \tag{1.7}$$

where a$_2$=$\frac{1}{4} + \frac{3}{4}x$ and $x = cos(\phi_f + \phi_i)\frac{sin(\phi_f - \phi_i)}{\phi_f - \phi_i}$ with ϕ_i and phi_f as the initial and final angle of the dipole axis with respect to the beam axis. The resulting angular distribution with respect to the beam axis can be calculated as a weighted average of the angular distribution corresponding to the different orientations probed by the dipole, with weight given by β:

$$W(\theta) = \sum_{i=1}^{t_{max}} \beta_i W(\theta, \Phi_i) \tag{1.8}$$

An example of an angular distribution calculated with this approach is given in Fig. 1.6 for collisions at impact parameters b=2 and 4 fm.

In order to reproduce the measured observables, simulations are performed at all impact parameters relevant for fusion and the results are finally averaged. The average is performed with a weight proportional to the cross section corresponding to each impact parameter. For central collisions this is well approximated with annuli, but as soon as we

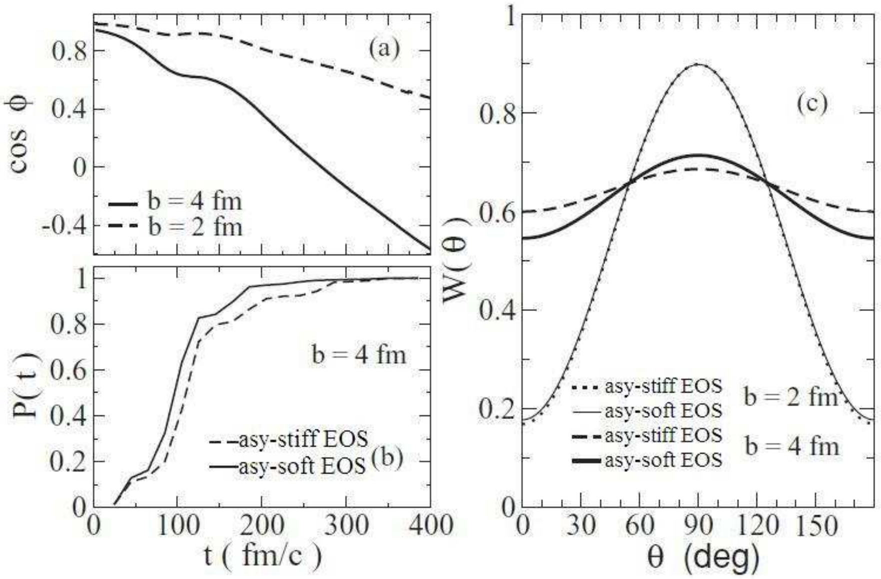

Figure 1.6: Results of the analysis of BNV simulation for the reaction ^{132}Sn+^{58}Ni at 10 MeV/nucleon. (a) Time dependence of the rotation angle at b = 2 fm(dashed line) and b = 4 fm(solid line). (b) Time evolution of the emission probability P(t), see text, for b = 4 fm impact parameter. (c) Weighted angular distributions for b = 2 fm and b = 4 fm and for different choices of the parameterization of the EOS, namely dashed lines for the asy-stiff choice and solid lines for asy-soft (see Fig. 1.8 and [8]).

move to more peripheral collisions (quasi-)fission and break-up may compete with fusion and therefore the annuli overestimate the fusion cross section.

A method to extract the fusion cross section for peripheral impact parameters (4.5-8 fm) within BNV approach is currently under study [28]. In particular, the focus of this work is to evaluate the transition between fusion and break-up dominance at peripheral impact parameters . The method is based on a phase-space analysis of quadrupole collective modes in the first 200-300 fm/c after the collision. In particular, positive values of the derivative of the quadrupole moment Q(t) reflect instability of the system leading to break up or fast fission that displays also a dependence on the parameterization of the symmetry term (see Fig. 1.7).

1.3.1 Role of the Equation of State

Two different Skyrme parameterizations of the symmetry term of the Equation of State are implemented within BNV simulation, namely an asy-stiff and an asy-soft one [29]. The symmetry term is usually split in a potential and kinetic part:

$$\frac{E_{symm}}{A} = \frac{E_{symm}}{A}(kin) + \frac{E_{symm}}{A}(pot) = \frac{\epsilon_F}{3} + \frac{C(\rho)}{2\rho_0}\rho \tag{1.9}$$

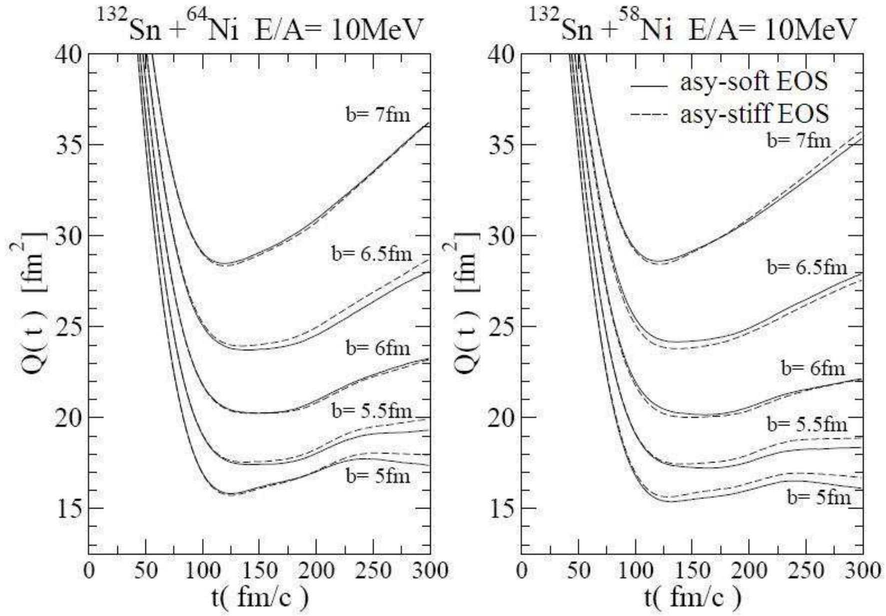

Figure 1.7: Time evolution of the quadrupole moment Q(t) in real space for different impact parameters b and for the asy-stiff (dashed line) and asy-soft (full line) parameterization of the EOS. Left panel: ^{132}Sn+^{64}Ni, right panel: ^{132}Sn+^{58}Ni [28].

with $C(\rho)/\rho_0$=a-bρ (with a=482 MeV fm^{-3} and b=-1638 MeV fm^{-6}) giving an asy-soft density dependence and C=32 MeV giving an asy-stiff density dependence. The two parameterizations cross at the saturation density ρ=0.145 fm^{-3} and are plotted in Fig. 1.8

The sensitivity of DD to the density dependence of the symmetry term of the EOS has been investigated in [8] with a system displaying a high N/Z asymmetry corresponding to D(t=0)=45 fm (calculated with Eq. 1.1). Such an asymmetry can be achieved only using a radioactive isotope as a projectile, that in this case was ^{132}Sn. For comparison, the system with D(t=0)=45 fm is studied together with the one with D(t=0)=33 fm produced with the stable projectile ^{124}Sn impinging on the same target ^{58}Ni. The observables that display sensitivity to the different parameterizations of the density dependence of the EOS are:

- centroid, width and integral of the γ spectrum (see Fig. 1.9)
- evolution of emission probability (see Fig. 1.6, bottom-left panel)
- competition between fusion and break up at peripheral impact parameters (see Fig. 1.7)

An asy-soft parameterization yields an higher restoring force for density lower than saturation (where DD oscillation develops) and therefore an higher frequency and a faster

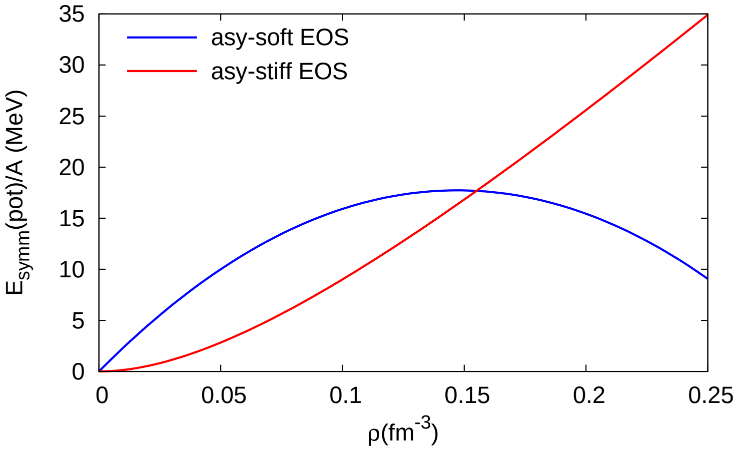

Figure 1.8: Symmetry energy as a function of density for asy-soft and asy-stiff parameterization of the EOS.

damping of the oscillation, corresponding respectively to an higher centroid ($\sim$ 1 MeV) and larger width of the γ emission spectrum. An asy-stiff parameterization corresponds to a slower dynamics and therefore a delayed emission probability, that may exhibit some second-order effect in the angular distribution.

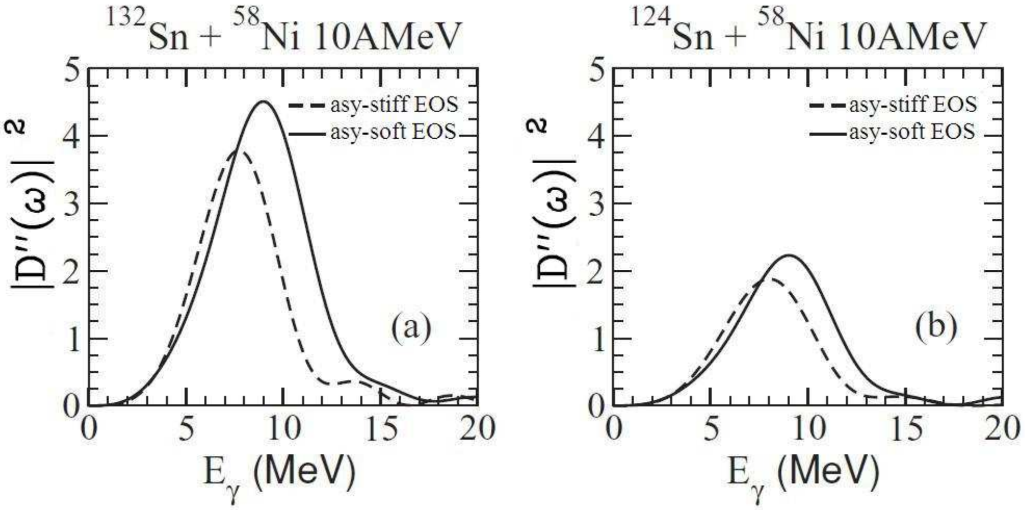

Figure 1.9: Power spectra of the dipole acceleration at b = 4 fm (in c^2 units) for the ^{132}Sn+^{64}Ni reaction (a) and for the ^{124}Sn+^{58}Ni (b). Solid lines correspond to asy-soft EOS and the dashed lines to asy-stiff EOS [8].

1.4 Systematics with ^{132}Ce

Six of the reactions listed in Tab. 1.1 produce the CN ^{132}Ce, with beam energies ranging from 6 to 16 MeV/u. This allows to make several observations on entrance-channel and beam-energy dependence of DD emission. The beam-energy dependence observed with the systems ^{32}S+^{100}Mo [18] and ^{36}Ar+^{96}Zr [19] (with a very similar dipole moment D=18.2 and 20.6 fm, respectively) displays a rise and fall behavior (see Fig. 1.10) already theoretically predicted for the DD emission of other systems [6]. This is expected to be a universal trend. The decrease for decreasing beam energy is attributed to a slow dynamics in the neck region between projectile and target, where the DD oscillation develops, and therefore a reduced dipole acceleration results (see Eq. 1.5). The decrease for increasing beam energies is due to the damping related to fast processes like pre-equilibrium neutron emission and nucleon-nucleon direct collisions that will reduce the N/Z asymmetry and damp the isovector oscillation.

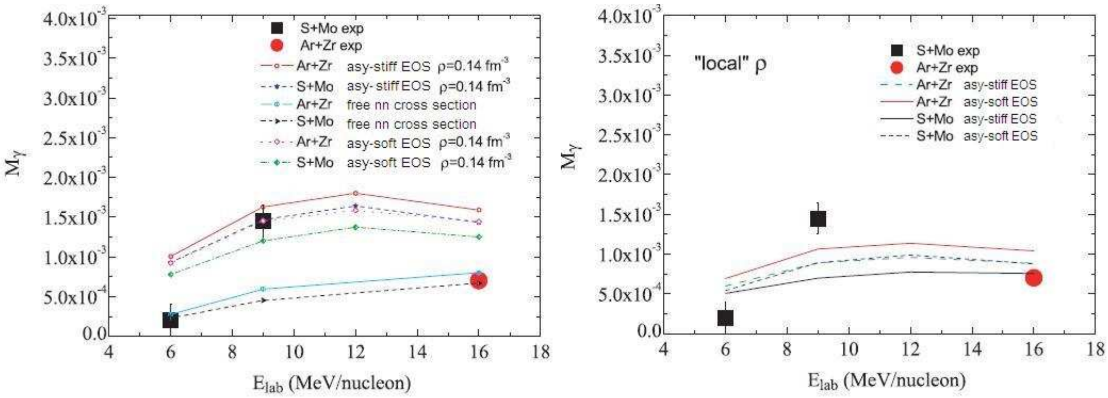

Figure 1.10: Measured DD γ multiplicity is compared with the one calculated with BNV model and Bremsstrahlung approach. The BNV simulations are performed with free nucleon-nucleon cross section (left panel) and with in-medium cross section, both at a fixed density 0.14 fm^{-3} (left panel) and at the local density calculated within the simulation (right panel) [20].

In Chapt. 4 the results obtained for the DD multiplicity in the system ^{16}O+^{116}Sn at 8 and 15 MeV/nucleon will be summarized. The results obtained for the angular distribution of DD emission at 15 MeV/nucleon and the preliminary analysis of the measurement performed at beam energy 12 MeV/nucleon will be presented and discussed.

Chapter 2

Isospin mixing in compound nucleus: Giant Dipole Resonance

2.1 Isospin formalism

In the isospin formalism, neutrons and protons are assumed to be different states of the nucleon with values 1/2 and -1/2 of the projection I_z of the isospin operator I. According to this definition, the projection of isospin operator for a nucleus can be written as:

$$I_z = \frac{N - Z}{2} \tag{2.1}$$

Isospin symmetry is largely preserved by nuclear interactions and the main violations of isospin symmetry are due to the Coulomb interaction [30]. The effect of isospin symmetry violation is that isospin is not a completely good quantum number for the nucleus, but in many cases this effect can be neglected or is small enough to be treated in a perturbative way.

As discussed in Subsect. 1.3.1, the nuclear force drives the nuclei towards a configuration with the lowest possible imbalance between protons and neutrons, that means the lowest possible I_z. The tendency of the nuclear force towards nuclei with N=Z is opposed by the Coulomb force, which favors an excess of neutrons over protons. Since the Coulomb force does not saturate, its effect becomes eventually dominant for large A (approximately A>40), leading to a deviation of the β-stability valley from the N=Z line. The relation between N and Z yielding the higher binding energy for a given mass A can be obtained from Weizsäcker's formula for nuclear masses and is the following:

$$N - Z = \frac{0.4A^2}{200 + A} \tag{2.2}$$

Furthermore, within a given nucleus, the nuclear force prefers the states with the lower possible I consistent with the given I_z, that is I_0=I_z. The "lowest possible isospin" rule holds well for all even-even and odd-mass nuclei and it breaks down only in several odd-odd self-conjugate nuclei like ^{34}Cl, ^{42}Si, ^{42}Sc and ^{46}V, where I=0 and I=1 states are almost degenerate [31].

2.2 Isospin at low and intermediate temperature

In first-order perturbation theory the admixture of I=I$_0$+1 states into I=I$_0$ states can be written as

$$(\alpha^{I_0+1})^2 = \sum_{I_0+1} \frac{|\langle I = I_0+1|H_c|I=I_0\rangle|^2}{(E_{I=I_0+1}-E_{I=I_0})^2} \tag{2.3}$$

where H$_c$ is the isovector part of the Coulomb potential. Since the Coulomb potential preserves angular momentum J and parity π, it can couple only states with the same J$^\pi$ and, more efficiently, with similar spatial wave function. Such states at low excitation energy usually lie at rather different energy, so the mixing probability α^2 is kept small by the large denominator of Eq. 2.3. At higher excitation energy, the levels come closer and also develop a finite width Γ. This fact can be still accounted for in first-order perturbation theory introducing a complex energy.

$$(\alpha^{I_0+1})^2 = \sum_{I=I_0+1} |\frac{\langle I = I_0+1|H_c|I=I_0\rangle}{(E_{I=I_0+1}+i\Gamma_{I=I_0+1}/2)-(E_{I=I_0}+i\Gamma_{I=I_0}/2)}|^2 \tag{2.4}$$

The maximum of α^2 is expected to occur when level spacing became similar to the width of the state [32].

2.2.1 Theoretical models of isospin mixing in nuclear ground state

Theoretical calculations of isospin mixing in the ground state are usually performed in limited single-particle spaces either with the fully symmetry-conserving shell model, or with projected mean-field model approach. The results of theoretical calculations of isospin mixing in ^{80}Zr are summarized in Tab. 2.1 and range from 1% to 4.5%.

Fig. 2.1 displays the Z (or, equivalently, A) dependence of the isospin mixing probability found by [35] (upper panel) and [37] (lower panel) for several self-conjugate nuclei with Z up to 50. In Ref. [35], the focus is on the sensitivity of the isospin mixing to the quadrupole deformation of the Hartree-Fock solutions. Smaller values of isospin-mixing probability are systematically found for deformed Hartree-Fock solutions. In Ref. [37], isospin mixing has been evaluated for the first time in a non-perturbative way taking fully into account to all orders long-range polarization effects associated with the Coulomb force. Spurious isospin-mixing effects are eliminated with a rediagonalization of the total Hamiltonian in the good-isospin basis. Spurious mixing leads to a suppression of Coulomb-induced mixing as can be seen in the lower panel of Fig. 2.1 by comparing the results obtained before and after rediagonalization (hollow and filled triangles respectively).
In literature the isospin-mixing probability has been labeled with different notations. In the case of Fig. 2.1 the quantity plotted on the y axis corresponds to the probability of finding components with I=I$_0$+1 (upper panel) or with I > I$_0$ (lower panel) in the ground

$\alpha^2_{I_0+1}$(%)	method	interaction	Ref.
1	analytic		[33]
3.6	HF+TDA	SG2	[34]
3.1	HF+TDA	SIII	[34]
3	HF spherical	SIII	[35]
2.5	HF deformed	SIII	[35]
3.9	HF	SIII	[36]
2.21	analytic		[36]
4.5	EDF	SLy4	[37]

Table 2.1: Available theoretical calculations of $\alpha^2_{I_0+1}$ are quoted from the references listed in the last column. The abbreviation HF stands for Hartree-Fock, EDF for Energy Density Functionals, TDA for Tamm-Dancoff approximation. In the third column the parameterization of Skyrme interaction used is given only for non-analytic approaches.

state. Since the contribution to the isospin mixing decreases with increasing I (e.g. in the work of [37] only I≤5 is found to contribute to the ground-state mixing), the two quantities are substantially equivalent. Strictly speaking, in the first case a lower limit to the isospin-mixing probability is obtained.

2.2.2 Extrapolation of isospin mixing at finite temperature

A method to extrapolate at finite temperature the isospin-mixing probability calculated for the nuclear ground state has been developed in [12] on the basis of the projected mean-field approach described in a previous work [38]. The method has been applied to ^{208}Pb [12] and the results of the extrapolation are shown in Fig. 2.2. We have applied this same procedure to ^{80}Zr with several simplifying approximations. The results are presented in Sect. 7.4.

Within the approach of [38, 12] the nuclear Hamiltonian is divided in two parts:

$$H = H_0 + H_1 \tag{2.5}$$

where H_1 is the isospin violating part while H_0 conserves isospin. The whole space is built up of eigenstates of H_0 and is divided into two parts, P and Q space

$$\begin{aligned} |P\rangle &= \{|\pi\rangle, |IAS\rangle\} \\ |Q\rangle &= 1 - |P\rangle = \{|q\rangle\} \end{aligned} \tag{2.6}$$

where $|\pi\rangle$ is the parent state and IAS stands for Isobaric Analog State. In fact the physical IAS is almost an eigenstate of H_0 with $|I, I-1\rangle$ and it develops a finite width due to H_1, that connects P and Q spaces. Fig. 2.3 represents a scheme of the P and Q spaces.

The spreading width of the IAS can be written as:

$$\Gamma^{\downarrow}_{IAS}(E) = -2Im \sum_q \frac{|\langle IAS|H_1|q\rangle|^2}{E - E_q + i\Gamma_q(E)/2} = \sum_q \Gamma_q(E) \frac{|\langle IAS|H_1|q\rangle|^2}{(E-E_q)^2 + (\Gamma_q(E)/2)^2} \tag{2.7}$$

where Γ_q and E_q are the total width and the energy of the states belonging to Q space. For many nuclei near the shell closure, the dominant contribution to the sum in Eq. 2.7 comes from the isovector monopole state (IVM) with isospin I_0-1, I_0, I_0+1 and therefore

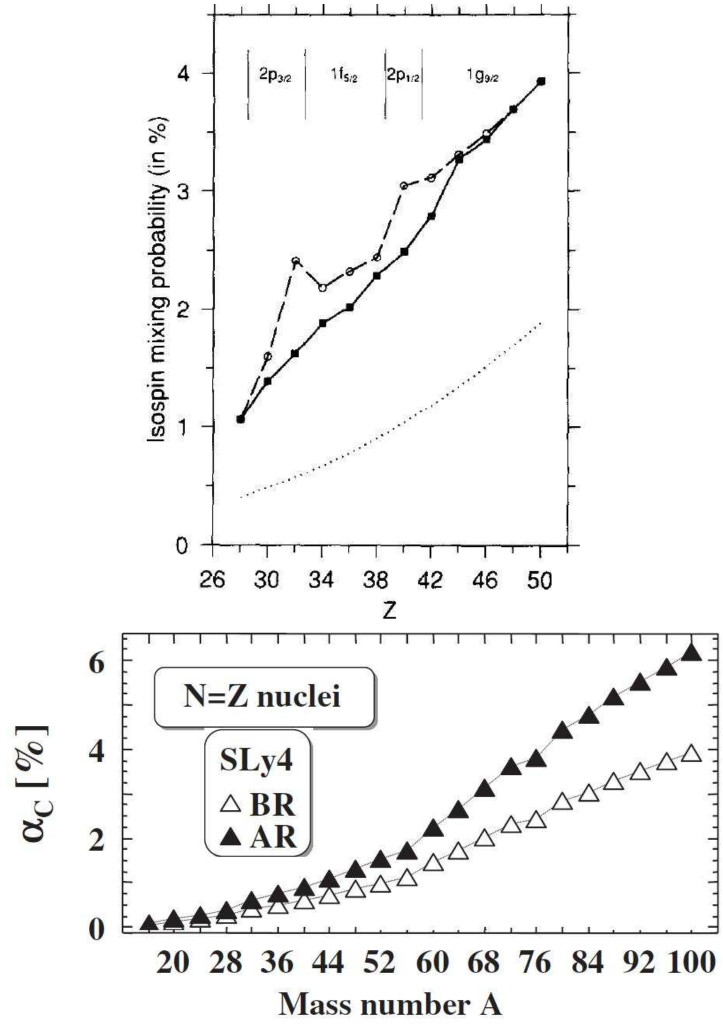

Figure 2.1: Isospin-mixing probability in the nuclear ground state defined as explained in the text. Upper panel: results quoted from Ref. [35] for spherical (hollow circles) and deformed (full squares) Hartree-Fock solutions. Deformation is prolate for ^{76}Sr, ^{80}Zr,^{92}Pd and oblate for ^{84}Mo. The dotted curve shows the results obtained with a spherical hydrodynamical model where the polarization effects due to the isovector-monopole modes are employed to estimate the isospin mixing [33]. Lower panel: results quoted from Ref. [37]; the points plotted with full triangles are the ones obtained after correcting for spurious isospin-mixing effects, that would produce a lower isospin-mixing probability (hollow triangles).

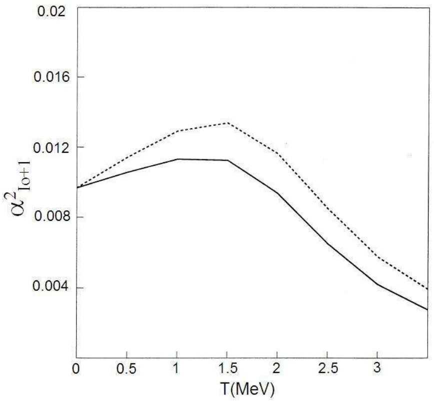

Figure 2.2: Temperature dependence of isospin-mixing probability in ^{208}Pb [12]. Solid and dashed curves correspond to two different parameterizations of the (mild) temperature dependence of $\Gamma^{\downarrow}_{IAS}$ and Γ_{IVM} adopted in [12].

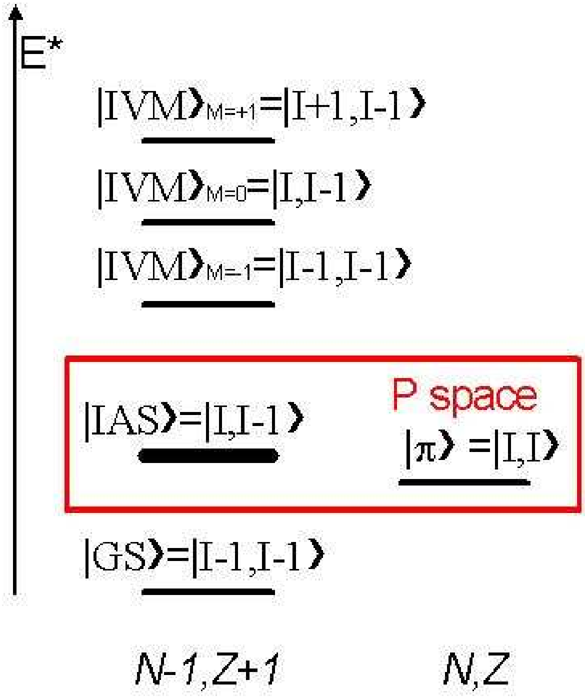

Figure 2.3: Scheme of the P and Q states. The scheme is drawn keeping in mind a scenario where the IAS is populated via (p,n) or (^{3}He,t) reaction on the parent state.

Eq. 2.7 can be rewritten as:

$$\Gamma^{\downarrow}_{IAS}(E_{IAS}) = \sum_M \Gamma_M(E_{IAS}) \frac{|\langle IAS|H_1|M\rangle|^2}{(E_{IAS}-E_M)^2+(\Gamma_M(E_{IAS})/2)^2} \tag{2.8}$$

$\Gamma_M(E_{IAS})$ is the width of the IVM state at the energy of the IAS. The energy of the IVM state is usually parameterized [39] in terms of the mass A as:

$$E_{IVM} = 88A^{-1/6}(1 + \frac{14}{3}A^{-1/3})^{-1/2}MeV \tag{2.9}$$

and is higher than the energy of the IAS. For example, Eq. 2.9 for ^{208}Bi yields 27 MeV while the IAS has been measured at lower energy, 15.14 MeV (with respect to the ground state of ^{208}Bi). Since Γ_{IVM} is proportional to the density of doorway states to which it may couple [40], then $\Gamma_{IVM}(\mathrm{E}_{IVM}) > \Gamma_{IVM}(\mathrm{E}_{IAS})$. Keeping in mind Eq. 2.4, this approach leads to the following formula for IAS spreading width as a function of the isospin mixing parameter α^2, the width of the IVM resonance and the isospin I of the parent state:

$$\Gamma^{\downarrow}_{IAS} = \Gamma_M(E_{IAS})(\alpha^{I_0+1})^2(I_0+1)F(I_0) \tag{2.10}$$

The isospin dependence of the width of the IVM has been factored in the F(I$_0$) isospin geometrical factor that can be neglected. This relation can be extrapolated at finite temperature in order to calculate the IAS built on an excited state, and it becomes:

$$\Gamma(E*)^{\downarrow} = (\Gamma_M(E^*) + \Gamma^{\uparrow}_{CN}(E^*))(\alpha^{I_0+1})^2(I_0+1)F(I_0) \tag{2.11}$$

where E* is the sum of the IAS energy and the excitation energy of the nucleus, that at finite temperature also develops a decay width $\Gamma^{\uparrow}_{CN}$. The isospin mixing parameter α^2 as a function of E* can be then obtained inverting Eq. 2.11.

$$(\alpha^{I_0+1})^2 = \frac{1}{(I_0+1)F(I_0)}\frac{\Gamma^{\downarrow}_{IAS}(E^*)}{\Gamma^{\uparrow}_{CN}(E^*) + \Gamma_M(E^*)} \tag{2.12}$$

2.3 Isospin at high temperature

With increasing excitation energy, the level width Γ becomes larger than the spacing. Therefore, a description in terms of single levels is not convenient anymore and is replaced by a description in terms of level density. The nuclear level density plays an important role in the statistical compound nucleus theory. Compound nucleus theory has been developed by N. Bohr to describe neutron capture in long-lived resonant states and later extended to describe the intermediate state populated in heavy ions fusion-evaporation reactions. The lifetime of this state is long enough to allow internal degrees of freedom (both single particle and collective ones) to achieve thermal equilibrium [41] . CN is well described in a thermodynamical approach with the formalism of Microcanonical ensemble [42], where temperature T and level density ρ can be deduced from the entropy S of the system:

$$T = (\frac{\delta S}{\delta E^{int}})^{-1} \tag{2.13}$$

$$\rho = \rho_0 exp^{S(E^{int})} \tag{2.14}$$

For high enough values of mass and excitation energy of the nucleus, as in the cases of interest, a good approximation to the entropy S of the nucleus is the entropy of a Fermi gas in the Grand-canonical ensemble: [1]

$$S = 2\sqrt{aE^{int}} \tag{2.15}$$

where a=A/16-A/8 is the level density parameter. Level density parameterization as a function of nuclear temperature and mass has been the subject of several studies [43, 44] and is an important ingredient of Statistical Model calculations (see App. B for level density parameterization in CASCADE code).
According to the definition 2.15 of S, T and ρ become:

$$T = \sqrt{E^{int}/a}$$

$$\rho = \rho_0 exp^{2\sqrt{aE^{int}}} \tag{2.16}$$

CN can directly decay via particle emission. The decay process can be described associating to the states a finite decay width $\Gamma^{\uparrow}$ corresponding to a lifetime τ through the Heisenberg rule:

$$\Gamma^{\uparrow} \sim 2\hbar/\tau \tag{2.17}$$

Due to the limited CN lifetime, a time-dependent approach to the isospin mixing problem is demanded as suggested by Wilkinson [31] and later formalized by Harney, Richter and Weidenmüller [11]. In this approach, the mixing probability is determined by the competition between CN lifetime and the timescale of isospin mixing process.
What the timescale of isospin mixing corresponds to can be better understood in a picket-fence model. The starting point of this description is an eigenstate of the nuclear Hamiltonian with I=1 embedded in a set of eigenstates with I=0 equally spaced with energy spacing D. As we switch on a perturbation (e.g. the isovector part of the Coulomb potential) coupling states with I=0 and I=1 with non-diagonal matrix elements v>D, the probability $P_{T=1}$(E) of the T=1 configuration per energy interval is:

$$P_{T=1}(E) = \frac{1}{2\pi}\frac{\Gamma_c^{\downarrow}}{(E_{T=1}-E)^2 + (\Gamma_c^{\downarrow}/2)^2} \tag{2.18}$$

where $\Gamma_c^{\downarrow}$ is the Coulomb spreading width of T=1 state ($\Gamma_>^{\downarrow}$ in Subsect. 2.3.1). The probability at the time t of finding the system initially populated in the T=1 state still in the T=1 state is given by the Fourier transform of Eq. 2.18:

$$\widehat{P_{T=1}}(t) = exp(-\frac{\Gamma_c^{\downarrow}}{2\hbar}t - \frac{i}{\hbar}E_{T=1}t) \tag{2.19}$$

---

[1] Microcanonical ensemble has fixed energy and particle number while Grand-canonical ensemble has fixed temperature and chemical potential but is free to exchange energy and particles. Microcanonical ensemble is the most adequate to describe the nuclear systems but the Grand-canonical ensemble is still a good approximation giving a simpler form for the Fermi-gas entropy.

from where one can deduce that a relation similar to 2.16 also links the Coulomb spreading width $\Gamma_c^{\downarrow}$ and the timescale τ_{mixing} of isospin mixing:

$$\Gamma_c^{\downarrow} \sim 2\hbar/\tau_{mixing} \tag{2.20}$$

With increasing temperature, CN lifetime becomes too short to allow a complete mixing, therefore a decrease of isospin mixing parameter α^2 is expected, corresponding to a partial restoration of isospin symmetry at high temperature. This trend is also predicted by Eq. 2.12, where $\Gamma^{\uparrow}$ in the denominator increases with increasing T. The values of CN decay width, Coulomb spreading width and corresponding timescales are listed in Tab. 2.2 for three different temperatures along the decay path of the CN ^{80}Zr studied in this Thesis.

T(MeV)	$\Gamma_{CN}^{\uparrow}$(MeV)	τ(s)	$\Gamma_c^{\downarrow}$(MeV)	τ_{mixing}(s)
2.1	0.23	2.8 10^{-21}	0.01	6.4 10^{-20}
1.9	0.15	4.4 10^{-21}	0.01	6.4 10^{-20}
1.8	0.13	4.9 10^{-21}	0.01	6.4 10^{-20}

Table 2.2: The CN decay width $\Gamma_{CN}^{\uparrow}$(MeV) and Coulomb mixing width $\Gamma_c^{\downarrow}$ followed by the corresponding lifetime τ and τ_{mixing} for the CN ^{80}Zr calculated within the Statistical Model. The temperatures calculated with Eq. 5.2 are the ones of the CN and the CN after 1 neutron and 1 proton emission.

2.3.1 Parameterization of Harney, Richter and Weidenmüller

Harney, Richter and Weidenmüller [11] take into account two classes of CN states with pure isospin, $|I_<\rangle$=$|I, I_z\rangle$ and $|I_>\rangle$=$|I+1, I_z\rangle$. By analogy with other symmetry breaking mechanisms, they describe the isospin mixing of states $|I_<\rangle$ into states $|I_>\rangle$ in terms of a spreading width $\Gamma_c^{\downarrow}$ defining the timescale of symmetry breaking induced by the Coulomb interaction H$_c$:

$$\Gamma_>^{\downarrow} = 2\pi\overline{|\langle I_>|H_c|I_<\rangle|^2}\rho(I_<) \tag{2.21}$$

$\Gamma_>^{\downarrow}$ is physically equivalent to the spreading width of the isobaric analog state (IAS) and changes only slowly (if at all) with excitation energy. This has been seen experimentally (see systematics in [11]) and justified theoretically by the fact that all the terms in Eq. 2.8 are rather constant with excitation energy. In fact, the intrinsic properties of the IVM resonance (width Γ_M, centroid E_M and sum rule $\sum_M |\langle IAS|H_1|M\rangle|^2$) do not depend significantly on the excitation energy of the compound nucleus.
$\Gamma_<^{\downarrow}$ can be defined exchanging > and < and is linked to $\Gamma_>^{\downarrow}$ by the detailed balance:

$$\Gamma_<^{\downarrow} = \frac{\rho(I_>)}{\rho(I_<)}\Gamma_>^{\downarrow} \tag{2.22}$$

Within the S-matrix formalism, the fraction $\alpha^2_<$ of states $|I_<\rangle$ that mix to states $|I_>\rangle$ can be written in terms of the Coulomb spreading width $\Gamma^{\downarrow}_c$ and CN decay width $\Gamma^{\uparrow}$ as:

$$\alpha^2_< = \frac{\Gamma^{\downarrow}_{c,<}/\Gamma^{\uparrow}_<}{1+\Gamma^{\downarrow}_{c,<}/\Gamma^{\uparrow}_< + \Gamma^{\downarrow}_{c,>}/\Gamma^{\uparrow}_>} \tag{2.23}$$

Similarly, the fraction $\alpha^2_>$ of states $|I_>\rangle$ that mix to states $|I_<\rangle$ is:

$$\alpha^2_> = \frac{\Gamma^{\downarrow}_{c,>}/\Gamma^{\uparrow}_>}{1+\Gamma^{\downarrow}_{c,>}/\Gamma^{\uparrow}_> + \Gamma^{\downarrow}_{c,<}/\Gamma^{\uparrow}_<} \tag{2.24}$$

2.4 Measurement of isospin mixing via forbidden transitions

Typically, isospin mixing can be observed via forbidden transitions, i.e. transitions that are forbidden by the isospin Clebsch-Gordan coefficients unless mixing of states with different isospin is taken into account. This is the case of E1 γ decay in I_z=0 nuclei, that is forbidden by the selection rules in the long wavelength approximation ($\lambda \gg$ nuclear dimension[2]) but has been observed both at finite and zero temperatures and used to evaluate the degree of isospin mixing of the decaying nucleus [9, 10, 13, 45, 46, 47]. The E1 γ decay from highly excited nuclei is associated with the decay of the Giant Dipole Resonance.

2.4.1 Giant Dipole Resonance properties

Giant Dipole Resonance on the ground state

Isovector Giant Dipole Resonance (GDR) is an isovector mode that can be excited by an electric field uniform on nucleus dimension. Protons are moved in the direction of the electric field while neutrons are shifted in the opposite direction in order to keep the center of mass at rest. Historically, GDR has been observed as a strong peak in the photoabsorption cross section that is a signature of the presence of a resonance. For spherical nuclei with mass > 40 the photoabsorption cross section is well parameterized by a single Lorentzian distribution

$$\sigma_{abs}(E_\gamma) = \sigma_o \frac{E^2_\gamma \Gamma^2}{(E^2_\gamma - E^2_{GDR})^2 + E^2_\gamma \Gamma^2} \tag{2.25}$$

with centroid E_{GDR} and width Γ. The centroid depends on the mass A of the nucleus on the top of which the oscillation is built (the relation $E_{GDR} \sim 79A^{-1/3}$ works well for intermediate and high-mass nuclei), and varies from $\sim$ 24 MeV in ^{16}O to $\sim$ 13 MeV in ^{208}Pb (Fig. 2.4).

---

[2] $\lambda \sim$100 fm for a E_γ=15 MeV, while the radius of a mass=80 nucleus is $\sim$ 5 fm.

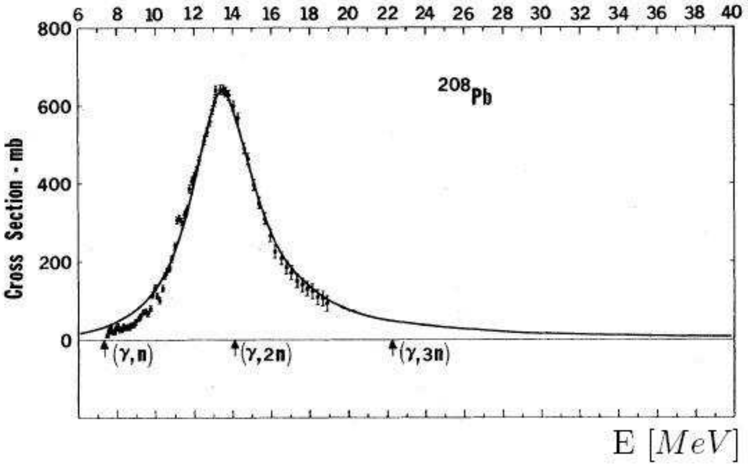

Figure 2.4: Experimental γ-absorption cross section for ^{208}Pb [48].

The isovector nature of GDR transitions implies the isospin selection rule ΔI=± 1, 0, with $0 \rightarrow 0$ transitions forbidden. Since the isospin is usually the lowest possible one, only ΔI=1,0 transitions are allowed for N $\neq$ Z nuclei, while only ΔI=1 is allowed for N=Z nuclei. In the first case, the energy splitting between the ΔI=1 and ΔI=0 components is

$$E_{I+1} - E_I = \frac{V(T+1)}{A} \tag{2.26}$$

where V corresponds to the Lane symmetry potential, renormalized including the effect of the particle-hole interaction [49, 50].
In case of statically deformed nuclei, the photoabsorption cross section is characterized by the superposition of up to 3 Lorentzian peaks with different centroids corresponding to the different axes of the oscillation (see Fig. 2.5).

The expected total strength of the GDR is given approximately by the classical Thomas-Reiche-Kuhn energy-weighted sum rule:

$$\int_0^{30MeV} \sigma_{abs}(E_\gamma)dE_\gamma = \frac{16\pi^3}{9\hbar c}\sum_f (E_f - E_i)B(E1, i \rightarrow f) = \frac{2\pi^2 e^2 \hbar NZ}{mcA} = 60\frac{NZ}{A}MeV.mb \tag{2.27}$$

where m is the nucleon mass and B(E1, $i \rightarrow f$) is the matrix element of the dipole operator between the ground state and all the available excited states. The measured strength divided by the expected one (usually named strength S) is usually found to be $\sim$1 for nuclei with mass $>$ 90, meaning that the GDR is a highly collective state (see Fig. 2.6, left panel).
Microscopically the GDR is described as a coherent superposition of one particle-one hole

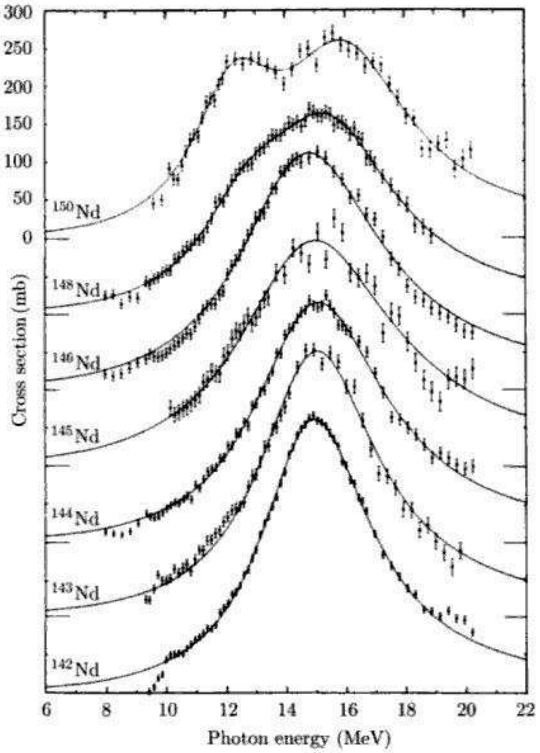

Figure 2.5: Experimental γ-absorption cross section for seven Nd isotopes. The development of a static deformation for increasing number of neutrons can be observed as a splitting of the GDR peak [39].

configurations. This state mixes with more complicated configurations (n particle-n hole with n ≥ 2), adding width (spreading width $\Gamma^{\downarrow}$) to the resonance, that sums up to the decay width of the resonance $\Gamma^{\uparrow}$ to give the total width Γ:

$$\Gamma = \Gamma^{\downarrow} + \Gamma^{\uparrow} \tag{2.28}$$

The width Γ of the GDR built on the ground state of a nucleus varies from $\sim$ 4 to 8 MeV, with the narrowest widths found in magic nuclei (see Fig. 2.6, right panel).

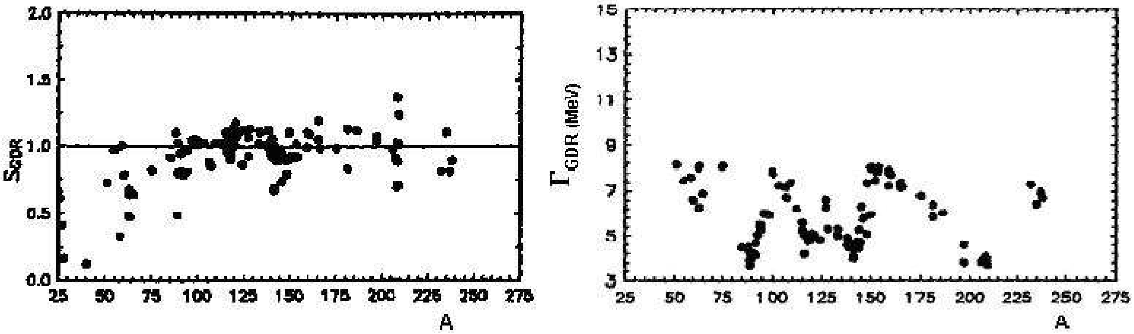

Figure 2.6: Measured strength (left panel) and width (right panel) of the GDR as a function of nuclear mass A. [51].

Giant Dipole Resonance on excited states

In 1955, David Brink suggested that *"the energy dependence of the photoeffect is independent of the detailed structure of the initial state so that, if it were possible to perform the photoeffect on an excited state, the cross section for absorption of a photon of energy E_γ would still have an energy dependence given by ...(Eq. 2.25)."* This hypothesis, known as "Brink-Axel hypothesis", together with the detailed balance, implies that the high-energy γ decay of excited compound nuclei formed in nuclear reactions should show an enhancement at $E_\gamma \sim E_{GDR}$ determined by the average behavior of the GDR built on excited states.
Newton *et al.* measured in 1981 for the first time the decay of the GDR built on excited CN states produced in a fusion-evaporation reaction [52].
The energy dependence of this γ emission can be deduced from these two hypotheses and is the following:

$$\sigma_{decay}(E_\gamma) = \sigma_{abs}(E_\gamma)\frac{\rho(E_f^*)}{\rho(E_i^*)} = \sigma_o \frac{E_\gamma^2\Gamma^2}{(E_\gamma^2 - E_{GDR}^2)^2 + E_\gamma^2\Gamma^2} exp(-E_\gamma/T) \tag{2.29}$$

where ρ is the level density defined in Sect. 2.3, E_γ is the energy of the γ transition and T is the average nuclear temperature. If excitation energy is higher than the threshold for particles emission, γ decay competes with particle decay. The branching ratio between γ and neutron decay (the preferred decay mode for stable nuclei) is usually $\sim 10^{-3}$. Parameterizing the neutron emission cross section as a Maxwellian distribution depending on binding energy B_n and temperature T

$$\sigma_n \sim T^2 exp[(E_n - B_n)/T] \sim T^2 exp(-B_n/T) \tag{2.30}$$

we obtain the following energy dependence for the ratio between γ and neutron emission cross sections:

$$\frac{\sigma_\gamma}{\sigma_n}(E_\gamma) \sim \frac{E_\gamma^2 \Gamma^2}{(E_\gamma^2 - E_{GDR}^2)^2 + E_\gamma^2 \Gamma^2} T^{-2} exp(-(E_\gamma - B_n)/T) \tag{2.31}$$

Eq. 2.31 allows us to interpret the typical GDR energy spectrum and to divide it into three regions as shown in fig 2.7:

a) $E_\gamma < B_n$: the argument of the exponential function in Eq. 2.31 is > 0, therefore the cross section is dominated by the emission from the last decay steps at lower temperature.

b) $E_\gamma > B_n$: the argument of the exponential function in Eq. 2.31 is < 0, therefore the cross section is dominated by the emission from the first decay steps at higher temperature.

c) $E_\gamma > 30$ MeV: the GDR cross section becomes small and the measured spectrum is dominated by γ-ray produced in nucleon-nucleon Bremsstrahlung and cosmic-ray background, if the latter is not effectively suppressed by anticoincidence shielding technique.

The GDR built on a CN state has a width Γ greater than the one found in the ground state and increases with nuclear temperature and angular momentum [1, 53, 54]. The increase of GDR with temperature is shown in Fig. 2.8

This is not in contrast with Brink-Axel hypothesis: the broadening of the GDR peak is only due to the fact that the nucleus experiences a continuous range of deformations and space orientations as described by the Thermal Fluctuation Model (TFM) [51]. Each deformation is parameterized in terms of the Bohr-Wheeler coordinates β,γ and populated with a probability depending on the associated free energy at the temperature T:

$$P(\beta, \gamma) \sim exp(-F(T, \beta, \gamma)/T) \tag{2.32}$$

The resulting GDR strength function is given by the weighted superposition of Lorentzian distributions corresponding to all the different deformations that are experienced by the nucleus:

$$\sigma(E) = \int \sum_{k=1}^{3} \sigma_k(E, \beta, \gamma) P(T, \beta, \gamma) \beta^4 |sin(3\gamma)| d\beta d\gamma \tag{2.33}$$

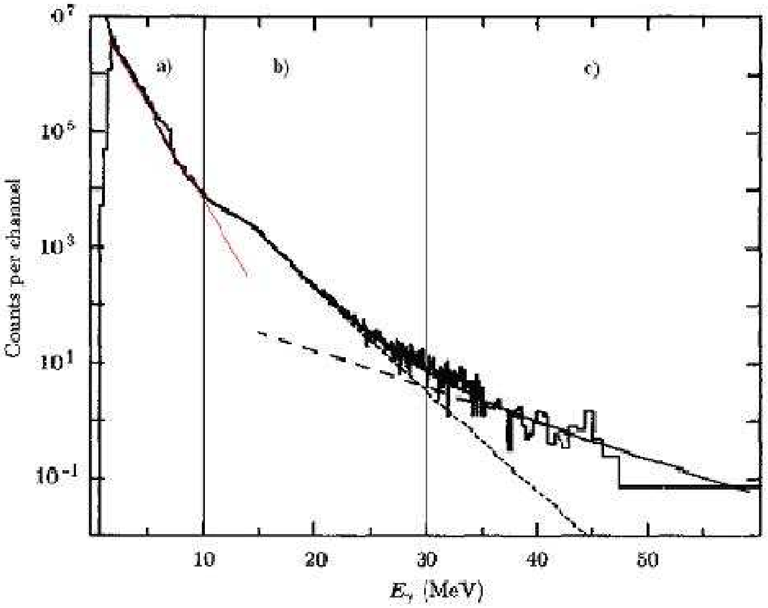

Figure 2.7: γ-ray spectrum from ^{16}O+^{116}Sn fusion reaction at E_{beam}=200 MeV, corresponding to an excitation energy of 165 MeV [39]. The full line is a fit to the data obtained summing a Bremsstrahlung component (long-dashed line) to the spectrum obtained with a Statistical Model calculation (short-dashed line). The three regions discussed in the text are explicitly indicated.

Each Lorentzian distribution has an intrinsic width that differs from the one at T=0 (Eq. 2.28) only due to the fact that both initial and final CN states may have a decay width [56]:

$$\Gamma = \Gamma^{\downarrow} + 2\Gamma^{\uparrow} \tag{2.34}$$

A linear relation between the average nuclear deformation $\langle\beta(\mathrm{J,T,A})\rangle$ and the increase of the FWHM of the Lorentzian distribution used to reproduce the GDR spectrum has been proposed in [57] and plotted in Fig. 2.9. In the same paper [57] is presented a parameterization of the average deformation $\langle\beta(\mathrm{J,T,A})\rangle$ based on Liquid Drop and Thermal Fluctuation Models that will be used in Subsect. 5.2.3 in order to make predictions for the systems under analysis.

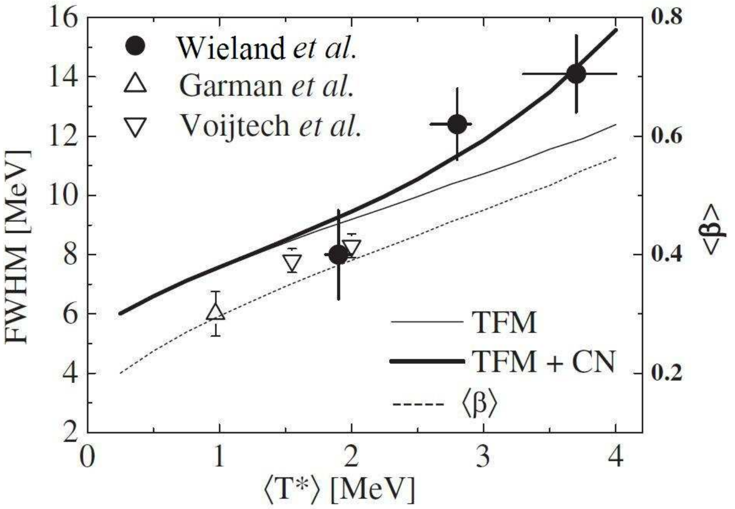

Figure 2.8: Comparison between measured and calculated GDR widths as a function of the effective nuclear temperature T [1, 55]. The data are taken at $\langle J \rangle$=45 $\hbar$ (filled dots), $\langle J \rangle$=8-16 $\hbar$ (up-pointing triangle), $\langle J \rangle$=23-27 $\hbar$ (down-pointing triangle). The thin (thick) continuous line shows TFM calculations without (with) CN decay width, while the dashed line shows the average deformation $\langle \beta \rangle$ calculated with TFM.

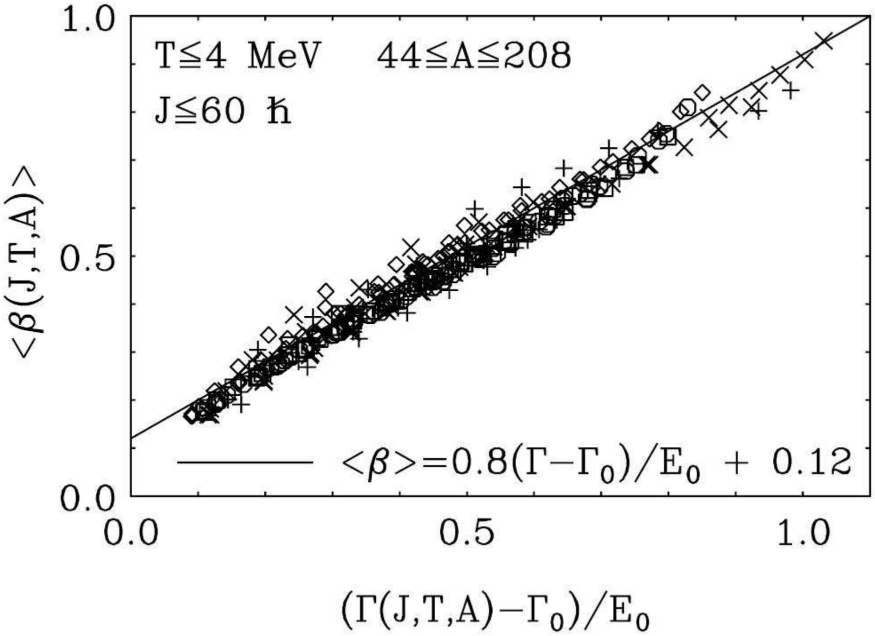

Figure 2.9: Linear relation between average nuclear deformation $\langle\beta(\mathrm{J,T,A})\rangle$ and GDR width Γ(J,T,A) (continuous line), valid for mass $44 \leq \mathrm{A} \leq 208$, $\mathrm{T} \leq 4$ MeV and $\mathrm{J} \leq 60$ $\hbar$. The symbols represent ^{44}Ti ($\times$), ^{90}Zr ($+$), ^{120}Sn ($\diamond$), ^{168}Er ($\Box$), ^{208}Pb ($\circ$) [57].

Chapter 3

GARFIELD-HECTOR apparatus at LNL

The experiments analyzed in this Thesis were performed at Laboratori Nazionali di Legnaro in the third experimental hall during the period 2008-2009. HECTOR (and lately HELENA) scintillator arrays have been coupled to GARFIELD (General ARray for Fragment Identification and for Emitted Light particles in Dissipative collision) array inside the GARFIELD scattering chamber (a cylinder of $\sim$ 3 m of diameter and 5 m of length). Also, 32 PHOSWICH scintillators have been placed inside the scattering chamber. All these detectors operated under vacuum ($\sim 10^{-5}$ mbar) and therefore demand either dedicated electronics (GARFIELD and PHOSWICH) or to transport the electric signal to Voltage Dividers placed outside the scattering chamber (HECTOR).

3.1 HECTOR detector

The HECTOR array is composed of 8 BaF_2 scintillators, each of $\sim$ 3 dm^3 of volume.
BaF_2 scintillator are characterized by high efficiency, due to the high atomic number (Z=74) and density of the material (4.88 g/cm^3), and by good timing performances (resolution $\leq$ 1 ns). Both features are very useful in the detection of high-energy γ rays emitted by excited nuclear states in competition with other kinds of emission, in particular neutrons. In fact, pair-production cross section, which is the dominant interaction process for $E_\gamma > 5$ MeV, scales as $\sim Z^2$ while the good time resolution allows to perform a clean neutron-γ discrimination via Time of Flight (Fig. 6.12). The drawback of BaF_2 is the poor energy resolution, that is $\sim$ 12 % at 1 MeV, but this is not critical since we are going to measure a continuum spectrum.
In this experimental campaign HECTOR scintillators operated under the high vacuum ($\sim 10^{-5}$ mbar) of GARFIELD scattering chamber. To avoid overheating of the electronics, the voltage divider was placed outside the chamber and the light signal from the photomultiplier was sent via dedicated cables.
Two signals are provided by the voltage divider, a fast and a slow one, collected at the anode and at an intermediate dynode, respectively. The fast signal is sent also to the

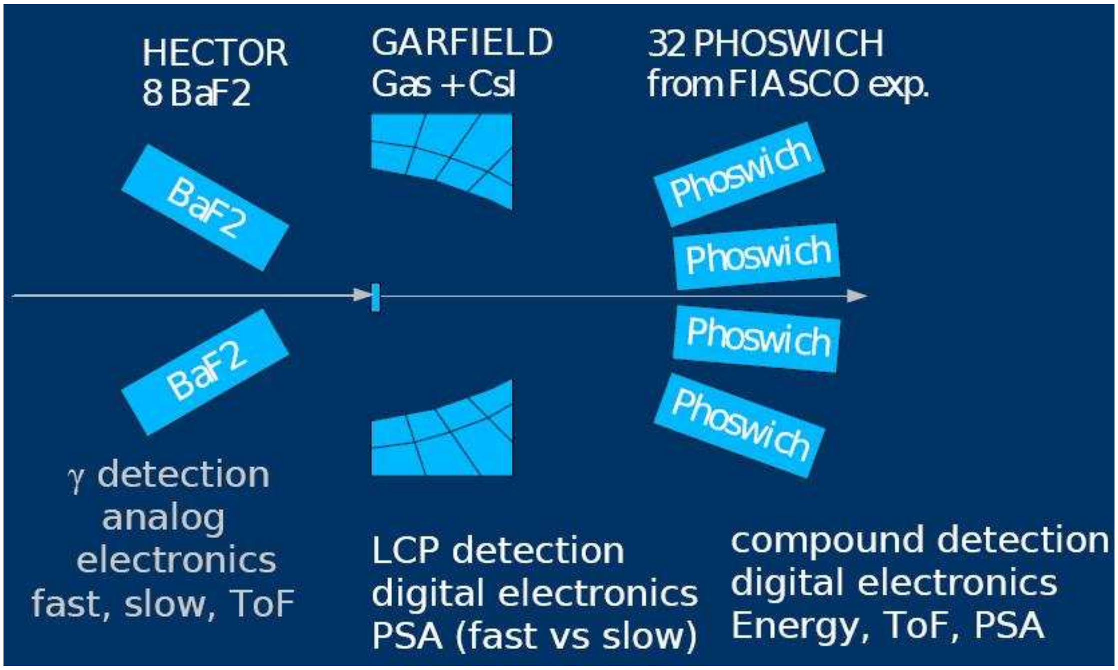

Figure 3.1: Schematic layout of GARFIELD-HECTOR apparatus.

temporal chain, while the slow one is used to build the energy chain, both operating with analog electronics.

HECTOR was placed inside GARFIELD scattering chamber in backward position with respect to the target, as shown in Figs. 3.1, 3.2 and 3.5. The central angles of all scintillator detectors are listed in Tab. 3.1.

# BaF_2	1	2	3	4	5	6	7	8
θ	160°	137°	124°	150°	150°	124°	137°	160°

Table 3.1: θ is the angle of each scintillator with respect to the beam axis.

This configuration was indeed determined by the space constraint inside the scattering chamber, but also allows to minimize the detection of light particles that are focused in forward direction by the kinematics of the reaction. In order to stop light charged particles, low-energy γ rays and electrons, the frontal face of HECTOR detectors is also shielded with lead.

The efficiency of HECTOR array in the present configuration is about $\sim 3\%$ at 10 MeV. The response function has been calculated with GEANT3 libraries [58] and folded in the calculations. The deformation of the γ-ray spectrum emitted by the CN induced by the detection process is shown in Fig. 3.3.

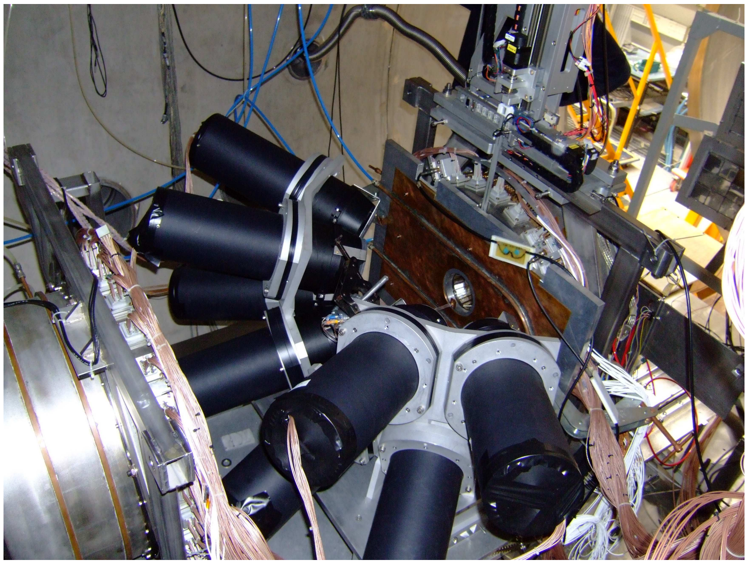

Figure 3.2: Picture of HECTOR scintillator detectors mounted inside GARFIELD scattering chamber. The scintillators point to the target position.

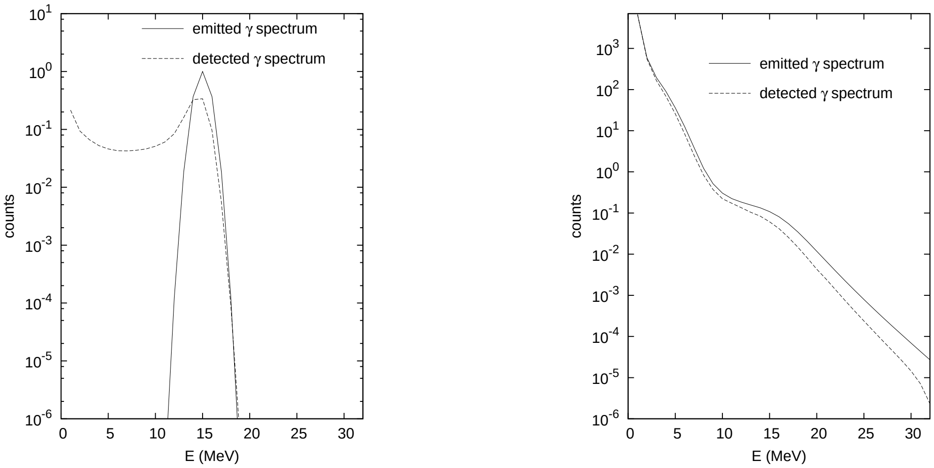

Figure 3.3: Effect of the response function of HECTOR apparatus on a Gaussian peak (left) and GDR decay spectrum (right). The spectra are normalized on the total number of counts in order to focus the attention on the distortion induced on the spectral shape.

3.2 HELENA detector

In the last measurement of the campaign, whose preliminary results are presented in Chapt. 4, BaF_2 scintillators from HELENA array were also employed. Due to their

smaller volume (~ 77 cm^3), these scintillators have lower efficiency for high energy γ-rays detection than the HECTOR ones but a slightly better time resolution, since the light has to travel a shorter path before attaining the photocathode.
The goal of this upgrade of the apparatus was twofold.
On one side, 5 detectors placed close to the target (named HELENA BACKWARD, see Fig. 3.5) were intended to be used as alternative time reference with respect to RF, that may induce a loss of time resolution as described in Sect. 6.5. The reference in this case is linked to the physical process, i.e. the emission of a high multiplicity of low energy γ rays from de-excited CN.
On the other side, 7 detectors placed in forward direction at ~ 80 cm from the target (named HELENA FORWARD) were dedicated to measure neutrons via time of flight (ToF). Neutron emission is the most important contribution in pre-equilibrium and equilibrium emission from CN (see Chapt. 1, 2). Therefore, in order to extract pre-equilibrium energy loss it is important to benchmark theoretical calculations with experimental data.
In both cases it was a challenging trial, since HELENA detectors are not equipped with electronics dedicated to work under vacuum. A cooling system has been developed in order to avoid overheating but still discharges in photomultipliers prevented almost half of the detectors from working properly.
This implies a low efficiency that prevented us to analyze the data relying on HELENA detectors as time reference. We have anyway verified that, even with low statistics, the ToF obtained with HELENA time signal has the same resolution as the one obtained with the radio frequency (RF) signal associated with the pulsed beam delivered by the Tandem-Alpi accelerator, as is shown in Fig. 3.4.

The analysis of the data collected by the detectors placed in the forward direction is in progress.

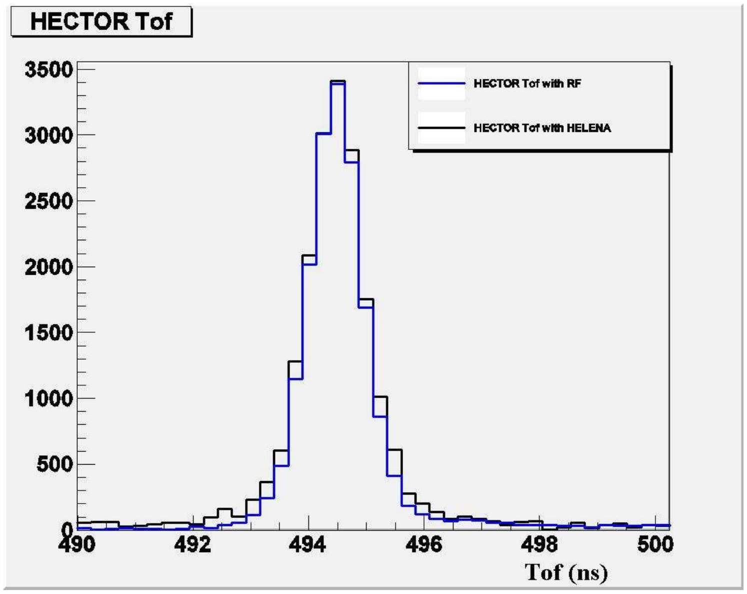

Figure 3.4: Time of flight obtained using the RF signal (blue line) and the HELENA time signal (black line) as reference. The FWHM of the peaks is the same, ~ 0.7 ns.

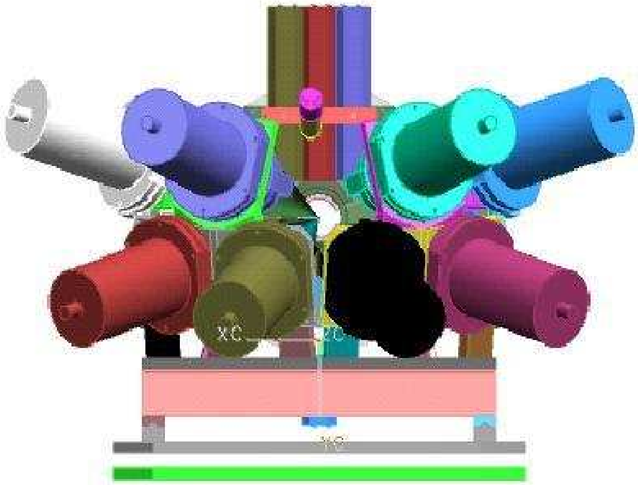

Figure 3.5: HECTOR (8 big scintillator detectors in the backward hemisphere) and HELENA BACKWARD (5 small scintillator detectors, seen in a vertical position in the figure) surrounding the target on the side of the incoming beam.

3.3 GARFIELD detector

GARFIELD is a high-granularity 4π array dedicated to charged-particle identification [3]. Isotopic identification can be achieved with ΔE-E technique or with pulse shape analysis of the signal coming from the stop detector (E). The setup is conceived in order to allow the simultaneous identification, with low energy threshold, of both light charged particles and heavy ions with an only two-stage telescope. In fact, the detector is characterized by a wide acceptance in Z, from 1 up to at least 28, with an identification and detection threshold of about 1-2 MeV/nucleon.
In these experiments only the forward chamber (see Fig. 3.6), covering angles $0° < \phi < 360°$ and $30° < \theta < 85°$ was used (HECTOR detectors stood in the place of the backward chamber). The high granularity of GARFIELD is achieved dividing it in sectors of $\Delta\phi$=15°, each containing a 4 CsI detectors centered at different angles θ=75°, 60°, 47°, 35°.

CsI(Tl) scintillators, which act as E detectors, have a good energy resolution (3% for α particles at 5.5 MeV), high stopping power and are not very sensitive to radiation damage. Their scintillation light has two components, a fast ($\sim$ 700 ns) and a slow ($\sim$ 2 μs) one, allowing to perform pulse-shape analysis (psa) and particle identification as shown in Fig. 3.7.

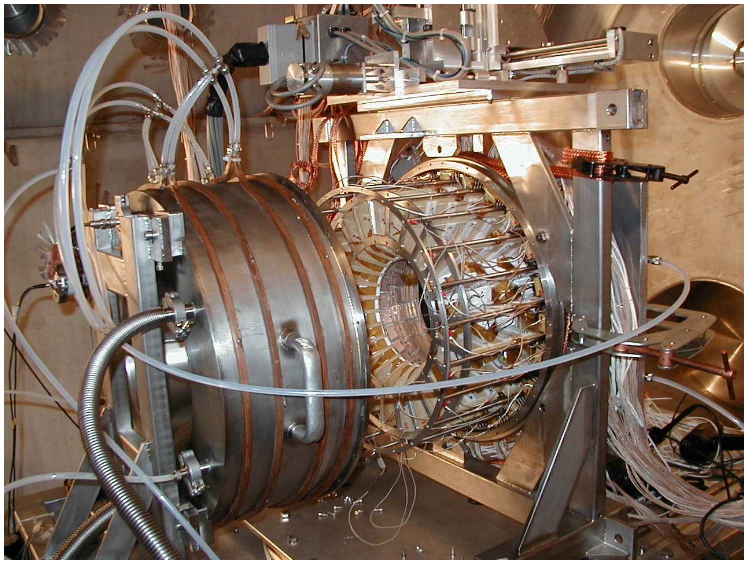

Figure 3.6: Forward chamber of GARFIELD detector.

The ΔE detector is a MicroStrip Gas Chamber (MSGC), a gas detector whose qualifying features are a large dynamical range, a small signal-to-noise ratio for the low ionizing ions and a low detection threshold. The filling gas is CF_4, characterized by high stopping power and drift velocity (10 cm/μs at 1 V/cm.Torr) of the electrons produced in the ionization process. These features allow to work at relatively low pressures (50 - 200 mbar) and

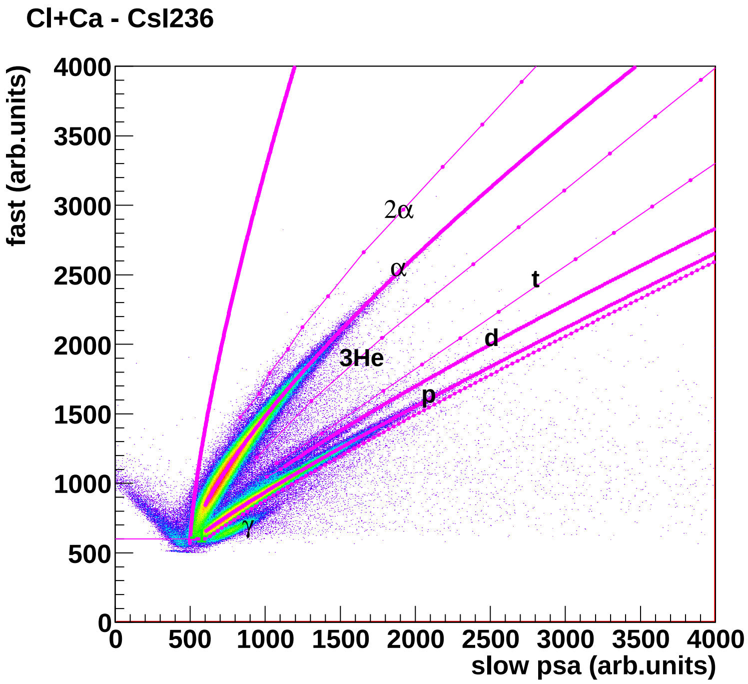

Figure 3.7: Fast vs slow psa correlation, with slow psa=3.5 × (slow - 4 × fast), for ^{37}Cl(E$_{beam}$=153 MeV)+^{40}Ca reaction. Ridges corresponding to different isotopes are labeled and tracked with identification lines; the outer lines delimit the region of the matrix where light charged particles lie from the region where neutrons, γ's and badly shaped events are found.

therefore at a lower voltage, reducing the potential damage associated with discharges. Each MSGC is divided in four regions of charge collection that we label up-right, up-left, bottom-right and bottom-left. Left and right parts give a division in the ϕ angle, while bottom and up part are the ones closer to the entrance window and to the CsI, respectively (see Fig. 3.8, bottom).

A telescope is built up combining one microstrip up-right (left), one microstrip down-right (left) and one CsI as shown in Fig. 3.8, giving a total of 192 telescopes (24 sectors × 4 CsI × 2 microstrip) in the forward chamber.

The combined information of the CsI and the MSGC can be used to improve the position resolution beyond the angular span of each CsI detector. The resolution in ϕ can improve from 15° up to 7.5° using the left-right division of the MSGC, while a better resolution in θ can be achieved using the information of the electron drift time in MSGC, related to the position of the ionization track with respect to the microstrip. This information is reliable only for high-ionization particles. Therefore, it has not been used in the analysis described in this Thesis since only light charged particles (up to Z=2) are emitted with a significant multiplicity in the reactions studied.

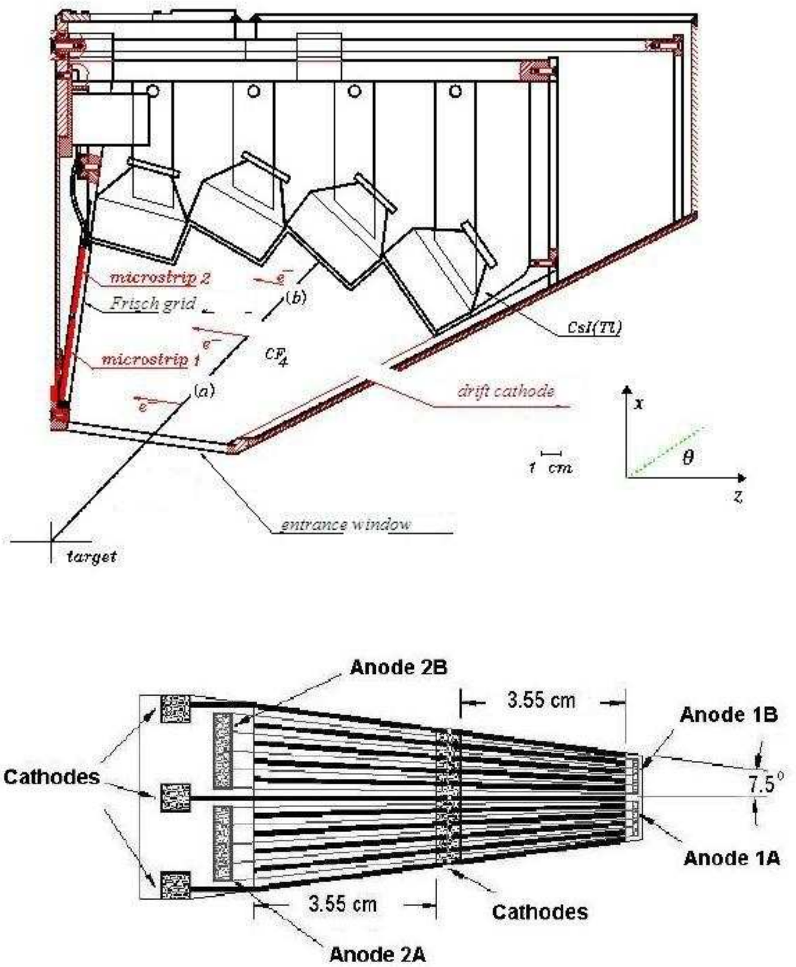

Figure 3.8: Scheme of a sector of GARFIELD detector for a fixed azimuthal angle ϕ (top) and of a MSGC (bottom). Before reaching one of the four CsI detectors, the particle entering the telescope has to cross the gas chamber. The electrons produced by ionization are collected by the four anodes constituting the MSGC. The MSCG sketched in the lower panel has to be turned sideways and integrated in the plane labeled as "microstrip 1" and "microstrip 2" as shown in the upper scheme.

Since its setting-up, the GARFIELD electronics has been upgraded from analog to digital signal elaboration. Details on signal processing are given in Sect. 3.5 and in [59, 60, 61].

3.4 PHOSWICH detectors

PHOSWICH scintillators [2] were arranged in 4 boxes surrounding the beam line at a distance of ~ 160 cm from the target and covering a polar angle between ~ 5° and 13°, in a configuration sketched in Fig. 3.9 and 3.10. Inside one of the PHOSWICH boxes, at an angle of ~ 2° with respect to the beam axis, was also placed a fast plastic scintillator of small dimensions, meant to detect the elastically scattered beam and to be used as beam monitor.

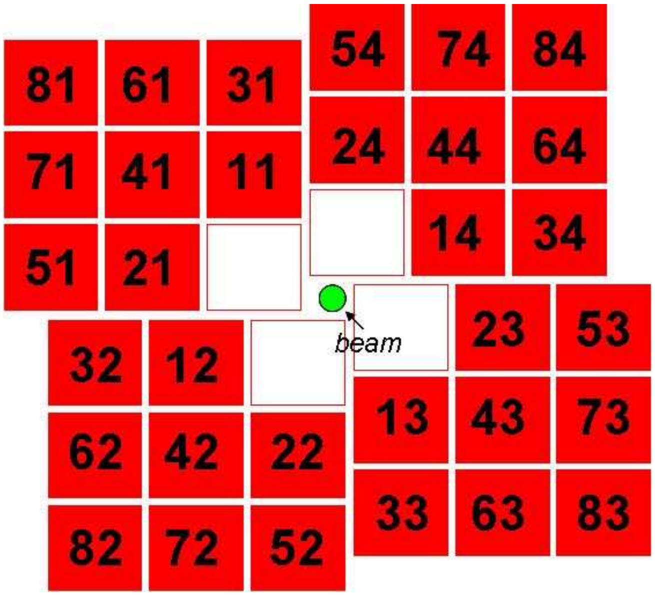

Figure 3.9: Scheme of the PHOSWICH wall around the beam axis. PHOSWICH detectors were grouped in 4 boxes, each hosting 8 detectors (the position closest to the beam was left empty since the elastic scattering cross section was too high at such a small angle ~ 3°).

The efficiency as a function of the polar angle θ has been calculated with a Monte Carlo simulation [62] and is plotted in Fig. 3.11.

PHOSWICH detectors consist of three coupled stages of scintillators followed by one photomultiplier, as sketched in Fig. 3.12 (top). The scintillation light of the different stages has different decay constants as detailed in Fig. 3.12 (bottom).

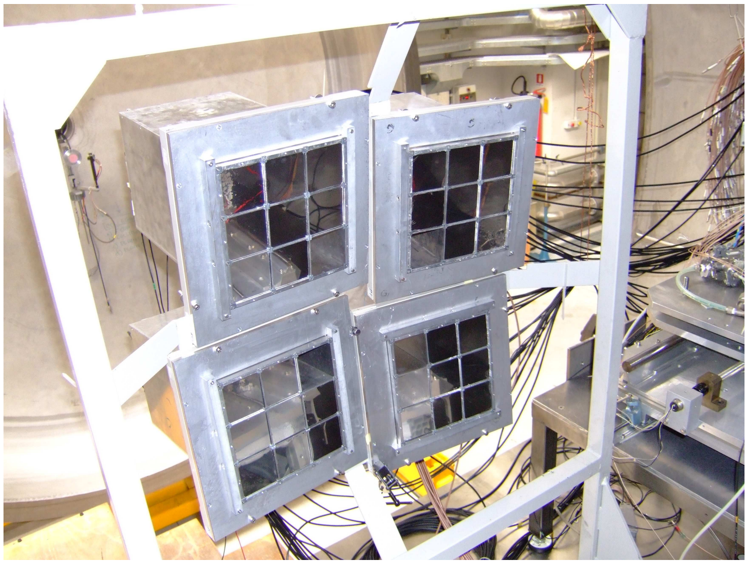

Figure 3.10: Picture of the PHOSWICH wall around the beam axis.

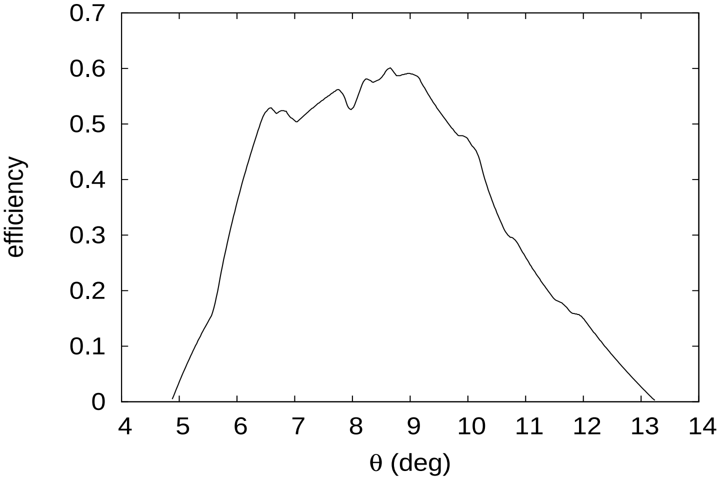

Figure 3.11: Percentage of coverage of ϕ angle for each θ value in the range covered by the PHOSWICH detectors [62].

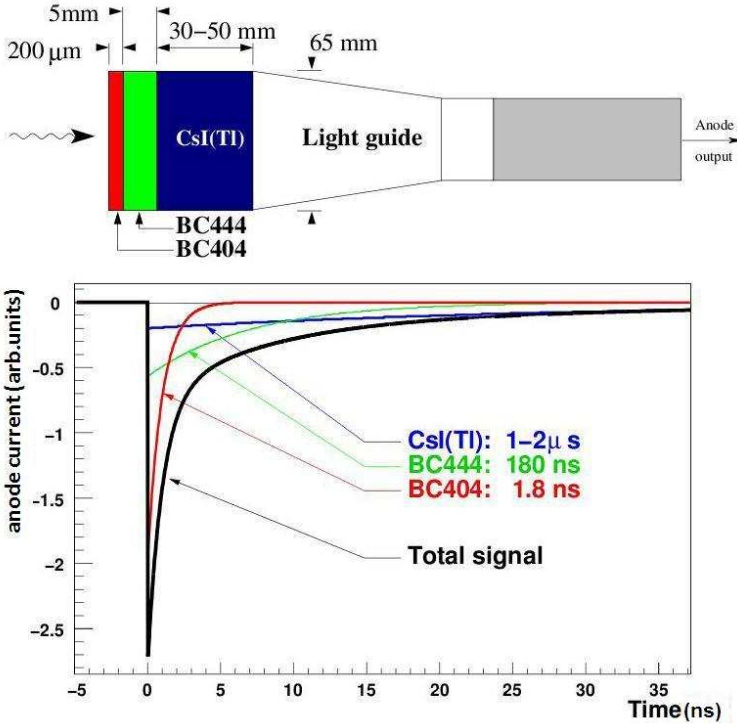

Figure 3.12: Layout of the PHOSWICH detectors (top): three stages of different scintillators are followed by a light guide and a phototube. The three scintillators have different decay constants (bottom), allowing to disentangle the three components of the light output performing an integration on different intervals of the detected signal.

The light output is integrated in three different gates labeled as A, B and C, each maximizing the light output from one stage and minimizing the ones from the others. An example of how the integration is performed is given in Fig. 3.13.

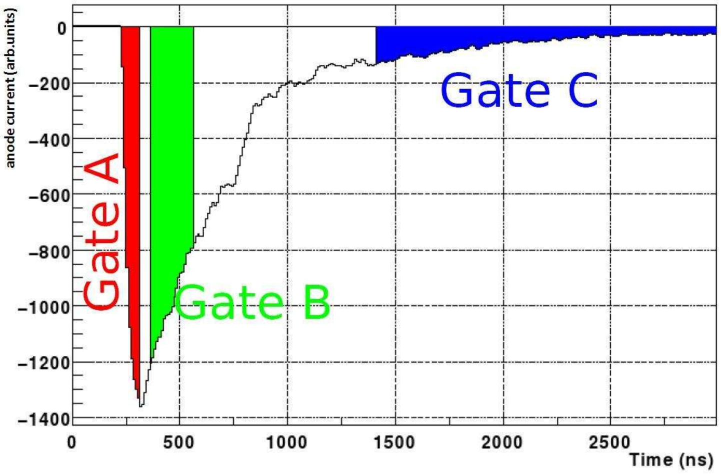

Figure 3.13: The three intervals of integration of PHOSWICH signals (labeled GA, GB, GC) for a signal produced by a Z=1 particle.

Details on signal processing are given in Sect. 3.5 and in [59, 60, 61].

3.5 Digital electronics

GARFIELD and PHOSWICH detectors are equipped with a digital electronics system based on the use of fast sampling ADC (Analog to Digital Converter) and DSP (Digital Signal Processor) developed in Sezione di Firenze of INFN. The digitizer is sketched in Fig. 3.14 and is composed of the following main blocks:

- the ADC samples the analog input coming from preamplifiers with a frequency of 125 MHz
- the Shift-Register continuously retains the last 512 samples sent by the ADC and needed for baseline extrapolation
- the FIFO (First In First Out) is used for temporary storage of data and is filled when a validation signal is sent by the trigger box
- the DSP reads the signal from FIFO and processes it online
- after being processed, data are sent to acquisition.

The DSP system is ”triggered”, i.e. the FIFO is filled and the signal is processed only when a validation signal is received. This validation can come from the main trigger

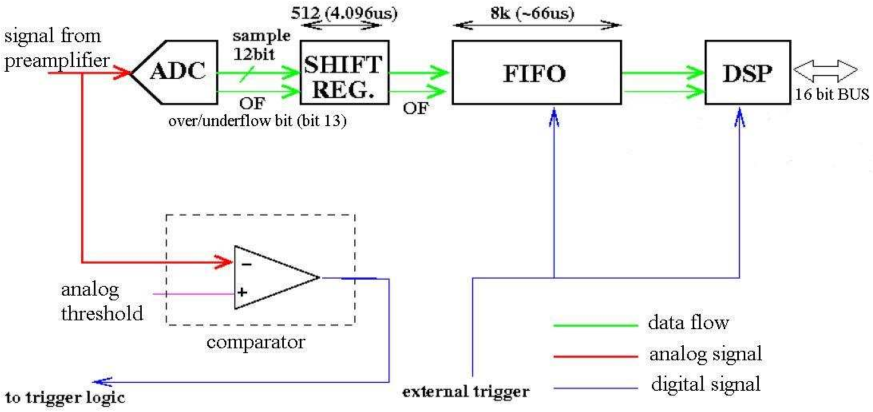

Figure 3.14: Scheme of the blocks composing the digitizer.

(case of PHOSWICH and, since 2009, GARFIELD) or from the single detector (case of GARFIELD up to 2008). Elaboration is performed online and only one out of 1024 signals is fully stored for monitoring. Twelve algorithms are available for signal processing, among them a digital CDF based on linear interpolation (Fig. 3.15) and the ones used to compute baseline, GA, GB, GC of PHOSWICH, fast and slow signal of CsI, etc. Baseline treatment

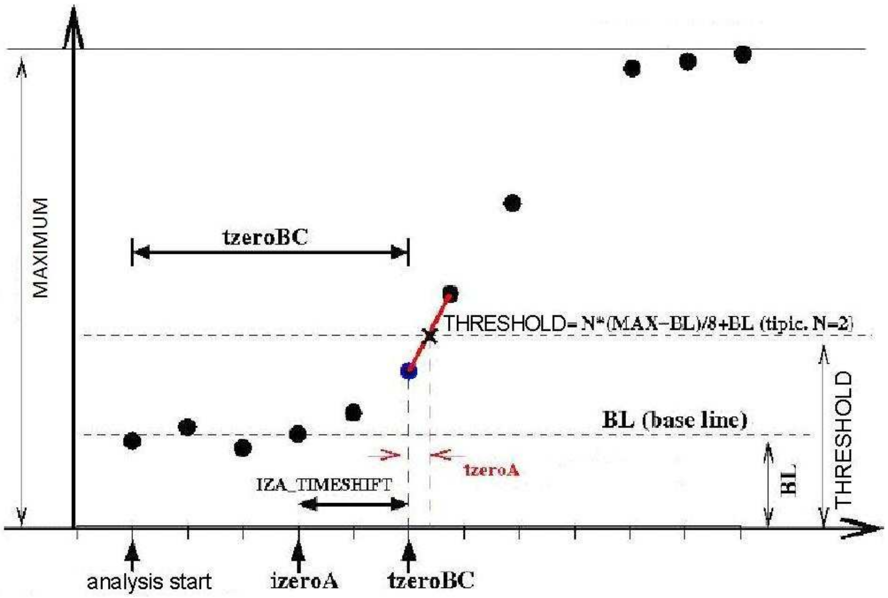

Figure 3.15: Time from digital CFD is obtained with an algorithm based on linear interpolation. The crossing of the threshold (calculated as written above) gives t_{CFD} and the start for the first interval of integration of the signal (GA).

is a very delicate issue in the signal processing. By definition, the baseline is calculated from the first 256 samples of the signals and has to be subtracted, sample by sample, from the signal either online or offline, as one can infer from Fig. 3.16.

Therefore, problems affecting the sampling of the baseline may have severe consequences on the processing of the whole signal. In these experiments two kinds of problems occurred:

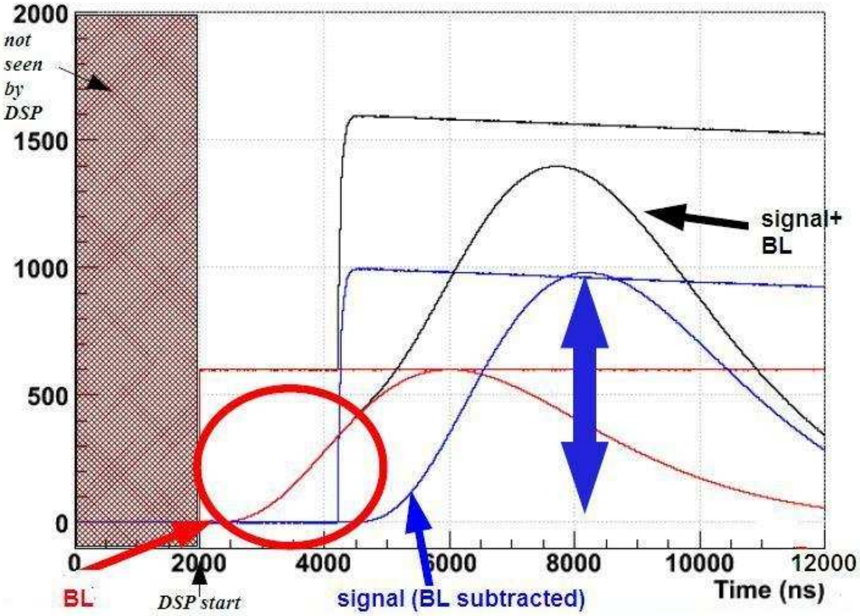

Figure 3.16: Input signal (step function) and after shaping (Gaussian like). Red line corresponds to baseline only, black to the whole signal (including baseline) and blue to a baseline-subtracted signal.

- part of the signal enters in the window dedicated to the sampling of the baseline (both for PHOSWICH and GARFIELD CsI)
- due to problems in the AC coupling at high counting rate, the ADC may go in underflow; the value sent to the DSP for the underflow sample is 4096 as shown in Fig. 3.17 (for GARFIELD CsI).

In both cases, the integral of the baseline deviates from the expected Gaussian shape, developing a bump on the right side or satellite peaks in the case of underflow in the ADC. The events affected by these problems can be discarded by applying a cut on the baseline as shown in Fig. 3.18. Since 2009, modifications have been introduced in the DSP algorithms in order to avoid the consequences of the underflow and the start of the processing has been anticipated of 20 samples in order to avoid interference between baseline and signal.

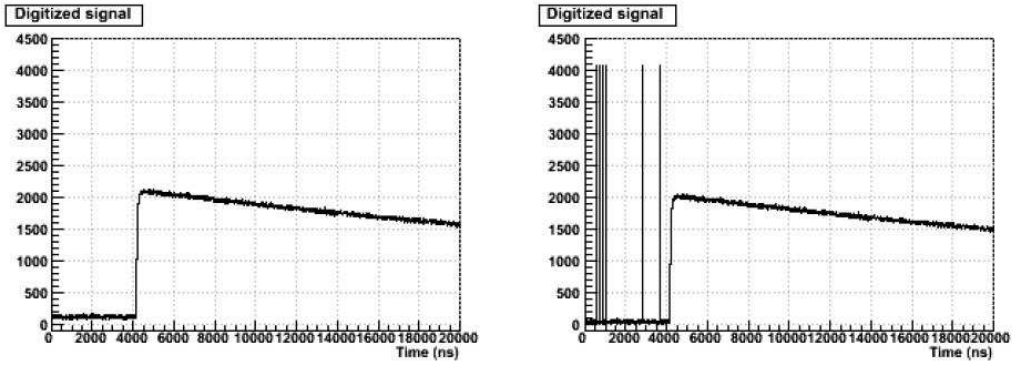

Figure 3.17: Signal sampled by DSP. The samples at 4096 correspond to ADC underflow.

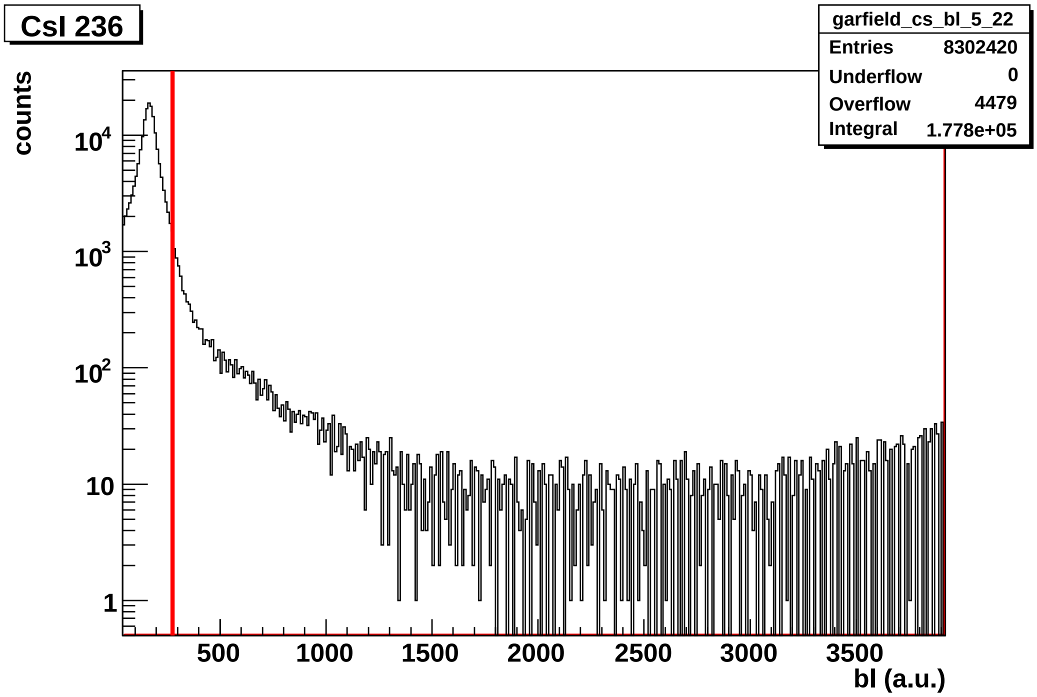

Figure 3.18: Baseline signal of one CsI detector. Since the statistics of light charged particles was high enough and the analysis described in Chapt. 6 was not aimed at calculating their absolute multiplicity, we decided to apply a "safe" cut on baseline values. An example of these cuts, which have been tuned on each CsI in order to discard events where the baseline may include part of the signal or ADC underflow occurred, is drawn with a red line.

The timing information from the different detectors has to be synchronized with a reference that is the same for all detectors. After 1100 samplings of the signal, corresponding to a window of 8800 ns, an analog sinusoidal signal is sampled for about 10 μs. The phase ωt_0 of this sinusoidal signal in the reference frame of each digitizer provides the offset of the channel with respect to the reference and we call it t_{ref} (Fig. 3.19).
In the experiment each channel is synchronized with respect to the RF signal obtained from the accelerator, which is treated as a signal coming from a detector and has its own t_{ref}, that for the sake of clarity we call t_{sync}. Finally, the ToF from the i^{th} detector is obtained as:

$$ToF = (t_{CFD} + t_{ref}) - (t_{RF} + t_{sync}) \tag{3.1}$$

where t_{CFD} and t_{RF} are, respectively, the digital (obtained as in Fig. 3.15) and analog time signals from detectors and RF, respectively.

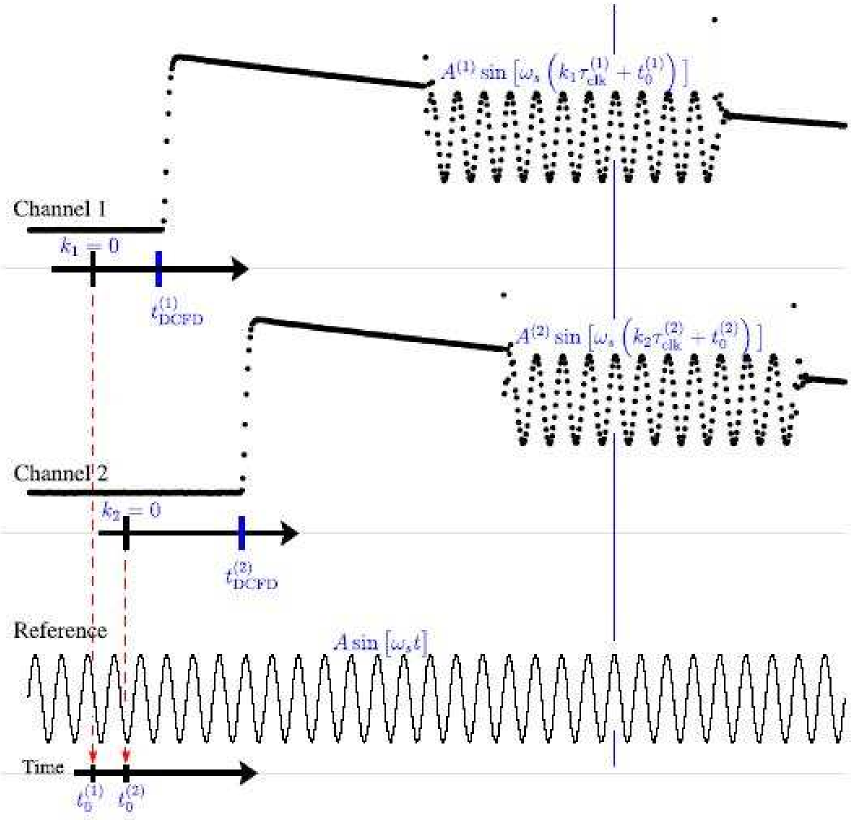

Figure 3.19: Signals from two detectors (up and middle) are synchronized using a common reference signal (bottom). After sampling the signals from the detectors for $\sim$ 10 μs, each DSP samples the same reference signal for $\sim$ 10 μs. $\omega_s \mathrm{t}_0^{(1)}$ and $\omega_s \mathrm{t}_0^{(2)}$ are the phases of the reference signal in the reference frame of digitizers (1) and (2) and have been named t_{ref} in Eq. 3.1 [59].

3.6 Data-acquisition system

The main goal of a good data-acquisition system is to efficiently (i.e. with a dead time as low as possible) recognize and collect the events corresponding to the physical process under study. A specific trigger signal is associated with each detector. The selection of the events is performed in the "trigger box" by requiring that the combination of the trigger signals coming from the different detectors satisfies given conditions. Fusion-evaporation events are characterized by a heavy residue, emitted preferentially in the forward direction, associated with light charged particles and γ's emitted isotropically in the residue's reference frame. Therefore, fusion-evaporation events can be selected by requiring the coincidence of signals from PHOSWICH and GARFIELD or from PHOSWICH and HECTOR detectors (indeed also triple coincidences are good events but have a low probability). When the energy deposited in the detector produces an electronic signal higher than a given threshold (usually set just above the level of the electronic noise or the internal radioactivity in the case of HECTOR detectors), a logical signal produced by the CFD (analog or digital) is sent to the trigger box (Fig. 3.21). In the case of the phoswich detectors also a higher threshold is implemented and a logical signal is sent to the trigger box only when the electronic signal falls between the low and high thresholds. This is meant to avoid that, besides low-energy electronic noise, also elastic scattering (that has a higher cross section at forward angles) might induce spurious coincidences. The region of GA vs ToF matrix populated by signals falling between the two thresholds is the shaded one in Fig. 3.20, while the signals falling outside are registered only as due to a random coincidence.

The acquisition system, based on FAIR front-end (Fast Advanced Interface Read-out) developed by INFN Sezione di Napoli, is an ECL BUS dedicated to the fast read-out of electronic data-acquisition modules. The transmission velocity of data on the BUS is 1.25 GBits/s and the architecture of the system is organized on two levels:

- at low level, the single electronic modules labeled by a VSN (Virtual Station Number) are grouped in segments. Every group is controlled by its own Segment Controller.
- at high level, every Segment Controller can communicate with the System Controller.

Segment controllers allow to associate with each event written on disk a trigger pattern, accounting for the combination of trigger signals received by the trigger box. The triggers used in February 2008 were the following:

1. OR.GARFIELD
2. OR.PHOSWICH_FUSED
3. OR.HECTOR
4. PULSER_HECTOR
5. OR.HECTOR.AND.OR.PHOSWICH_FUSED

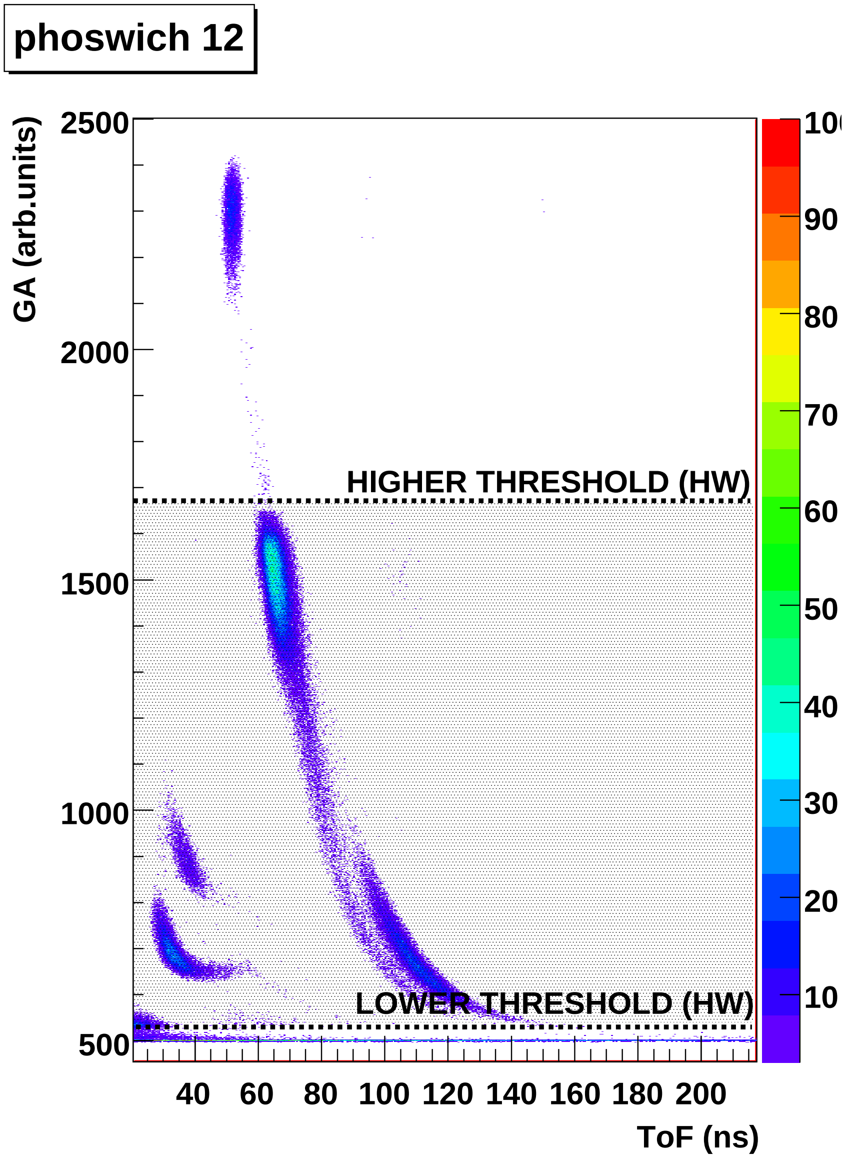

Figure 3.20: The effect of the lower and upper thresholds can be seen on GA vs ToF matrix. The position of the thresholds is marked with dotted lines, while the shaded area in between corresponds to signals that may trigger the data acquisition.

6. OR.GARFIELD.AND.OR.PHOSWICH_FUSED
7. not used
8. PLASTIC

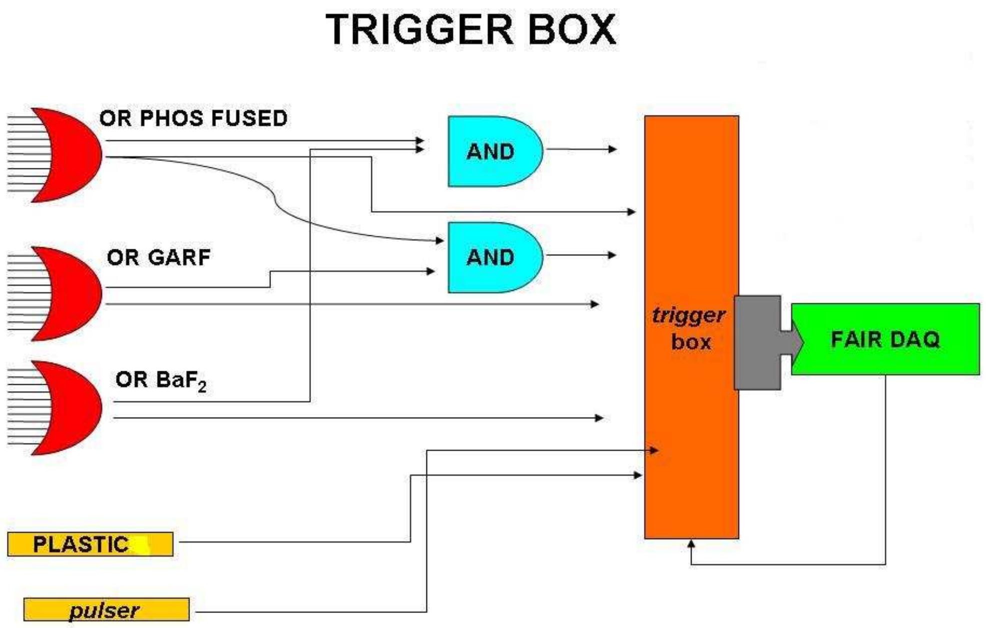

Figure 3.21: Scheme of the trigger box: the logical signals coming from the detectors (both singles and coincidences) are sent to the trigger box. The trigger box sends a validation signal (common start) to the data-acquisition system, corresponding to the logical OR of the incoming signals. In order to have an efficient collection of coincidences, the singles were downscaled by a factor D=2^n ($5 < n < 10$). Therefore, as far as singles are concerned only one signal out of D was giving valid trigger and was written on disk.

while in May 2009:

1. PULSER_HECTOR
2. OR.PHOSWICH_FUSED
3. OR.HECTOR
4. OR.GARFIELD
5. OR.HECTOR.AND.OR.PHOSWICH_FUSED
6. OR.GARFIELD.AND.OR.PHOSWICH_FUSED
7. OR.HELENA_FORW.AND.OR.PHOSWICH_FUSED

8. PLASTIC

Data were collected in common-start configuration, meaning that the start signal is given by the logical OR of the trigger signals, while the stop signal is given, for each detector, by the signal itself (if a signal has been measured in the detector) after applying a fixed delay. Due to the combination of delays and finite width of the logical signals, the RF signal used as a time reference (that is always the first full one after the trigger signal, see Fig. 3.22) depends on the trigger which caused the validation of the event. In particular, we have observed that the events triggered by OR.GARFIELD.AND.OR.PHOSWICH_FUSED take as reference the RF signal arriving 200 ns later with respect to all other triggers. This causes a shift of 200 ns backward in the ToF spectra (see Fig. 6.18) and has to be accounted for in the analysis, especially in order to extract multiplicities. Online as well as data stored on disk can be sent via a software called fair_dispatcher to a program for online visualization, called garfield_monitor [63]

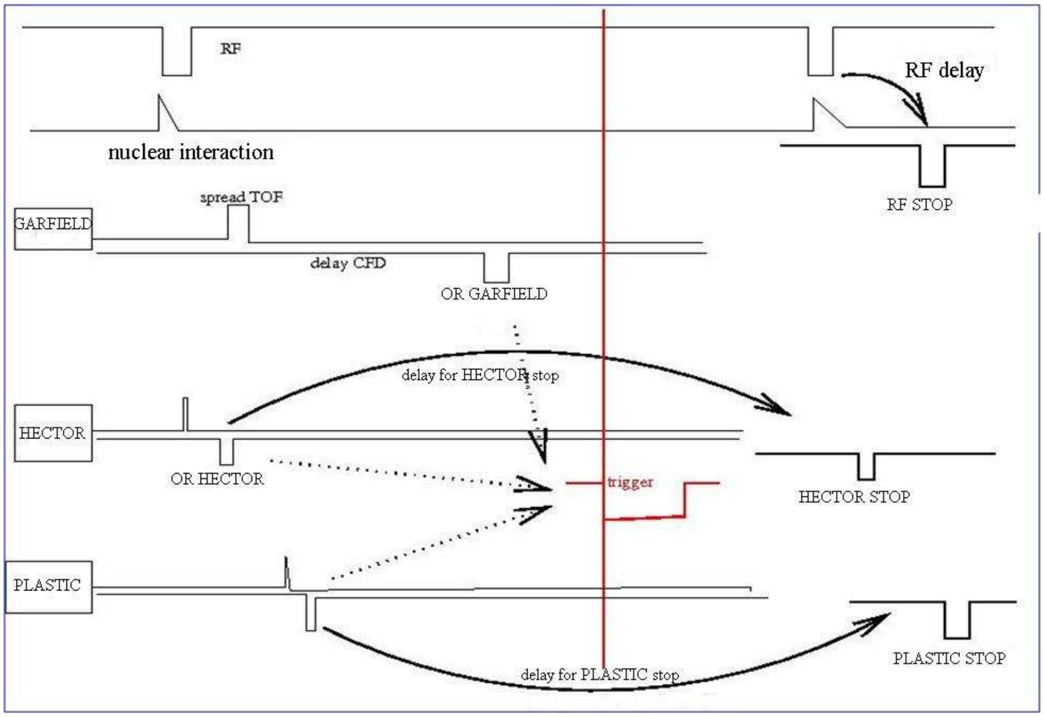

Figure 3.22: The time of each detector is the difference of the trigger signal (common start) and the delayed CFD signal of each detector (stop from each detector). RF is handled as a detector signal.

Chapter 4

^{132}Ce experimental campaign: results and ongoing analysis

In the last years, a series of measurements has been performed at Laboratori Nazionali di Legnaro with GARFIELD-HECTOR array in order to study the fusion and the decay of CN ^{132}Ce produced with different entrance channels and beam energies. The reactions used are listed in Tab. 4.1.

Reaction	E_{beam}(MeV/u)	E^*(MeV)	D(fm)	Δ	pre-eq.
^{64}Ni+^{68}Zn	4.7	100	1.2	0.01	/
^{64}Ni+^{68}Zn	6.2	150	1.2	0.01	/
^{64}Ni+^{68}Zn	7.8	200	1.2	0.01	α
^{16}O+^{116}Sn	8.1	100	8.6	0.32	p,α, γ
^{16}O+^{116}Sn	12	155	8.6	0.32	p,α, γ
^{16}O+^{116}Sn	15.6	206	8.6	0.32	p,α, γ

Table 4.1: The reactions used to populate ^{132}Ce are listed together with the beam energy, the CN excitation energy, the dipole moment D defined as in Eq. 1.1 and the mass asymmetry between projectile and target $\Delta = \frac{A_t^{1/3} - A_p^{1/3}}{A_t^{1/3} + A_p^{1/3}}$. In the last column the kind of pre-equilibrium emission that has been measured is listed.

In order to study the statistical decay of CN one has to pin down beforehand the pre-equilibrium contribution. Both light particles and γ rays can be emitted before CN thermalization adding a non-evaporative contribution to the measured spectra, that can be evaluated once the shape of the evaporative contribution is known. In the reactions discussed in this Chapter the mass loss due to pre-equilibrium particle emission is at most of $\sim$ 2 units of mass and is therefore negligible as far as the Statistical Model analysis is concerned. Pre-equilibrium light-particle emission has the effect of cooling down the compound nucleus, while the γ-emission multiplicity in the cases under analysis is too low to have a significant effect on the excitation energy of the CN. From this statement we can deduce that the information needed in order to extract the DD emission in ^{16}O+^{116}Sn is:

- the energy loss associated with pre-equilibrium light-particle emission
- the statistical γ emission from ^{132}Ce at the proper excitation energy

4.1 Light-particle emission

The measured α and proton spectra have been analyzed with the moving-source fit technique [64] that has been already used in order to study the light-particle spectra in fusion-fission reactions [65]. The global spectrum measured at 4 different angles θ=75°, 60°, 47° and 35° with respect to the beam axis is fitted with the sum of two distributions, one corresponding to an evaporative source and one to a pre-equilibrium source. The measured spectra together with the moving source fit are shown in Fig. 4.1. The energy loss can be calculated with Eq. 4.1

$$E_{loss} = (E_{kin,n}+BE_n)\times m_{PE,n}+(E_{kin,p}+BE_p)\times m_{PE,p}+(E_{kin,\alpha}+BE_\alpha)\times m_{PE,\alpha} \quad (4.1)$$

where E$_{kin}$ is the average kinetic energy, BE is the binding energy and m is the multiplicity. For αs and protons both E$_{kin}$ and m come from Moving Source Fit, while for neutrons we rely on the systematics [65]. The global energy losses are listed in Tab. 4.2. It can be noted that, for similar E$_{beam}$ $\sim$ 8 MeV/nucleon, pre-equilibrium particle emission is stronger in the mass-asymmetric channel. For the same system, its multiplicity increases with increasing beam energy.

Reaction	E$_{beam}$(MeV/u)	E*(MeV)	E$_{loss}$(%)	E$^*_{CN}$(MeV)
^{64}Ni+^{68}Zn	7.8	200	3.6±2	195.69±4
^{16}O+^{116}Sn	8.1	100	5.6±2.9	94.40±2.9
^{16}O+^{116}Sn	12	155	17	129
^{16}O+^{116}Sn	15.6	206	19.9±3.4	201.90±7

Table 4.2: The percentage of energy loss due to pre-equilibrium light-particle emission is listed for the reaction where it has been observed. The excitation energy left in the CN E$^*_{CN}$ is also displayed. As far as light charged particles are concerned, pre-equilibrium energy loss is the one extracted from measured data [64] except for ^{16}O+^{116}Sn at 12 MeV/u. The last one in fact is still under analysis and we are temporarily adopting the value extrapolated from systematics [64, 65].

The pre-equilibrium energy loss has been subtracted from excitation energy of ^{132}Ce* produced in the ^{16}O+^{116}Sn in order to obtain the excitation energy of the thermalized CN.

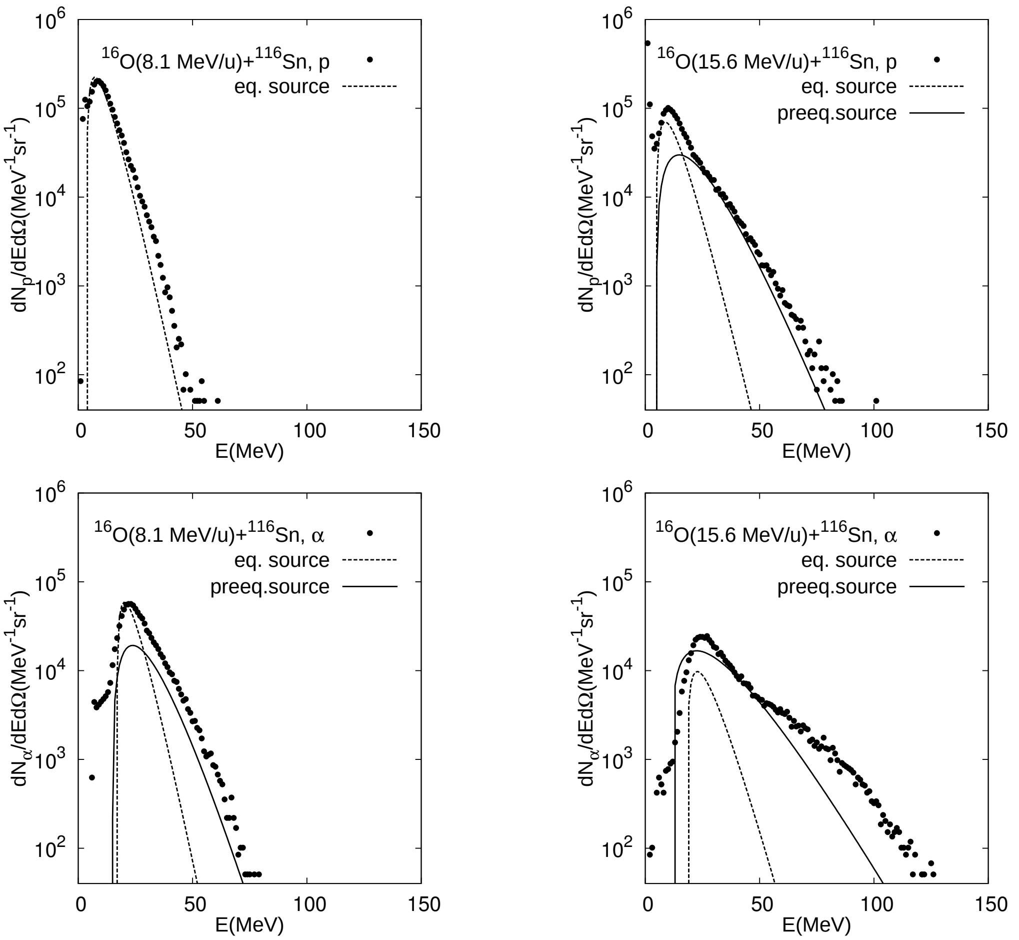

Figure 4.1: Spectra of protons (top panels) and α particles (bottom panels) in the laboratory frame measured at 29°-41° degrees in coincidence with evaporation residues for the reaction ^{16}O + ^{116}Sn at the two beam energies of 8.1 MeV/nucleon (left panels) and 15.6 MeV/nucleon (right panels). The dashed lines represent the emission from the evaporative source while the continuous lines the emission from the pre-equilibrium source.

4.2 ^{64}Ni+^{68}Zn entrance channel

From Tab. 4.1 it can be seen that the effect of pre-equilibrium emission can essentially be neglected for the ^{64}Ni+^{68}Zn system. The measured γ spectra are well reproduced by the Statistical Model and therefore an accurate evaluation of GDR parameters has been done [1]. Strength, width and centroid of GDR were used as free parameters in DCASCADE calculation (see App. B) and the best fitting values were obtained with χ^2 minimization technique. The strength was kept fixed at 1, corresponding to 100% of the EWSR, in agreement with the systematics plotted in Fig. 2.6. The best fitting values for the ^{132}Ce*

CN are listed in Tab. 4.3:

Reaction	E*(MeV)	$< T >$(MeV)	S	E$_{GDR}$(MeV)	Γ(MeV)
^{64}Ni+^{68}Zn	100	1.9	1	14	8±1.5
^{64}Ni+^{68}Zn	150	2.8	1	14	12.4±1.2
^{64}Ni+^{68}Zn	200	3.7	1	14	14.1±1.3

Table 4.3: GDR parameters (width Γ and centroid E$_{GDR}$) for the ^{132}Ce* CN at the three measured excitation energies and effective temperature $< T >$.

An increase of the CN width with increasing temperature up to almost 4 MeV can be inferred from these data, as discussed in [1, 55].

4.3 ^{16}O+^{116}Sn entrance channel

Statistical emission calculated with DCASCADE code has been subtracted from the total measured spectrum in order to pin down the DD contribution. The input parameters for DCASCADE code are the same as used to reproduce the γ-decay spectrum of the CN ^{132}Ce produced in the ^{64}Ni+^{68}Zn reaction except for excitation energy and the excitation energy-dependent GDR width. The latter has been obtained by linear interpolation of the width obtained for ^{132}Ce* populated with ^{64}Ni+^{68}Zn. In this limited excitation energy range the linear interpolation is equivalent to a 2^{nd}-order polynomial, as can be seen in Fig. 4.2.

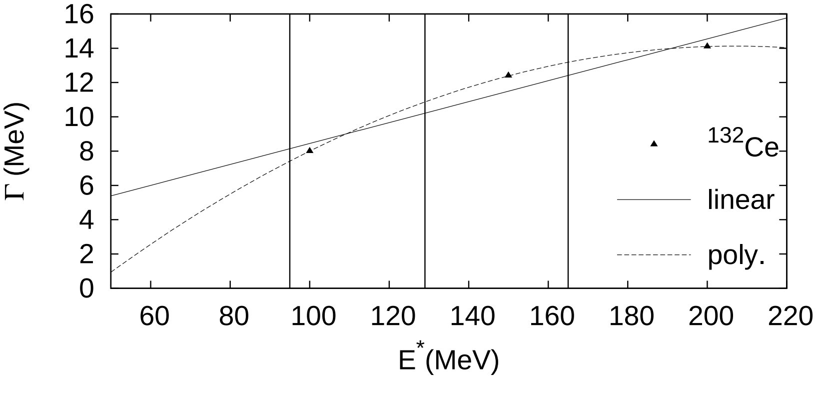

Figure 4.2: The parameters obtained from fit on measured data as described in [1] are interpolated both linearly and with a 2^{nd} order polynomial to obtain the width at the excitation energies of ^{132}Ce* produced by the ^{16}O+^{116}Sn reaction (vertical lines)

The inputs for Statistical Model calculation are listed in Tab. 4.4.

Reaction	E^*_{CN}(MeV)	S	E_{GDR}(MeV)	Γ(MeV)
^{16}O+^{116}Sn	94	1	14	8
^{16}O+^{116}Sn	129	1	14	10.2
^{16}O+^{116}Sn	165	1	14	12.4

Table 4.4: GDR parameters (strength S, width Γ and centroid E_{GDR}) for the ^{132}Ce* CN at the three measured excitation energies. The CN excitation energy of 129 MeV is deduced from the systematics and it is used only for a preliminary analysis.

4.3.1 Measurements at E_{beam}=8.1 and 15.6 MeV/nucleon

The Statistical Model calculation is compared with measured data in Fig. 4.3, and the difference associated with pre-equilibrium DD emission is plotted in the insets on a linear scale.

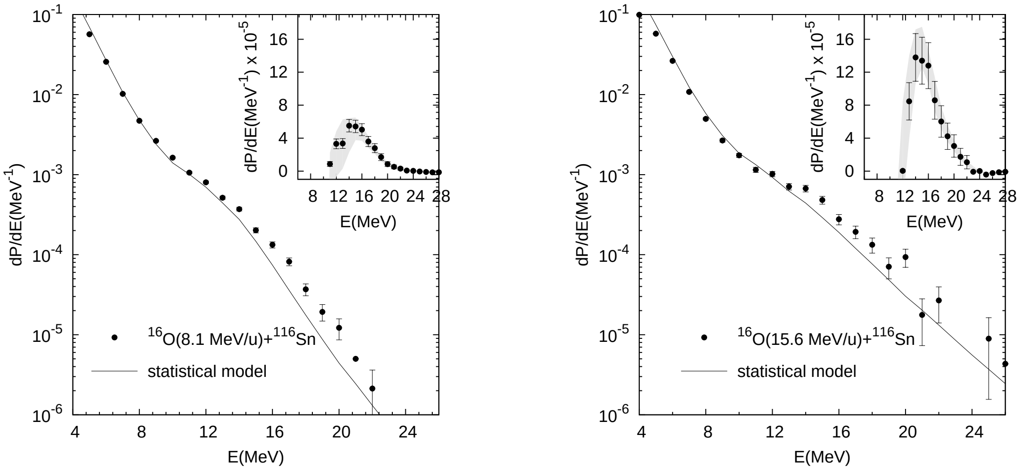

Figure 4.3: The measured γ-ray spectra of ^{16}O + ^{116}Sn at the two bombarding energies of 8.1 MeV/nucleon (left panel) and 15.6 MeV/nucleon (right panel). The continuous lines are the statistical model predictions at E*= 94 MeV and E*= 165 MeV (see text), respectively. The insets show the difference between the measured spectra and the statistical model predictions providing the γ-ray yield of the DD; the error bars indicate the uncertainty in the determination of the pre-equilibrium contribution [21].

The multiplicity of DD emission integrated in the 10-22 MeV energy range displays a smooth increase with beam energy; see Fig. 4.4. In this figure, it can be seen that the multiplicity calculated within BNV model with a Bremsstrahlung approach (see Sect. 1.3) reproduces the experimental results and also the smooth increasing trend, both with an asy-stiff and an asy-soft parameterization of the density dependence of the symmetry term of the EOS.

The data collected at the beam energy of 15.6 MeV/u allow us to make further con-

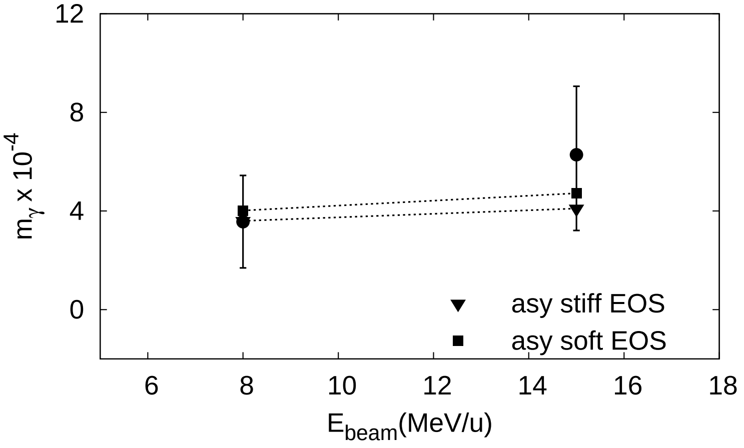

Figure 4.4: Measured and calculated DD γ multiplicity as a function of beam energy for the system ^{16}O + ^{116}Sn. The error bars in the measurement (dots) reflect mainly the uncertainty in the determination of the energy lost in the pre-equilibrium phase. The calculations performed with the BNV model correspond to two different parameterizations of the symmetry term of the EOS (the lines are to guide the eye).

siderations. The fact that this energy is very close to the one of the reaction measured by [19, 20] and already presented in Sect. 1.4, allows to observe the dependence of DD on N/Z asymmetry at fixed beam energy per nucleon. Unexpectedly and contrary to BNV predictions we do not observe an increase with increasing N/Z asymmetry but a rather flat dependence (see Fig. 4.5) that may suggest a more complicated interplay between beam energy and N/Z asymmetry in the onset and damping of DD mode. Indeed further investigation and new measurements are demanded.

For the measurement at 15.6 MeV/u it was also possible to extract an angular distribution limited to the angles where BaF$_2$ detectors were placed. This angular distribution is shown in Fig. 4.6 together with three curves calculated according to Eq. 1.7 with three different values of the parameter a_2.

One of the three values of a_2 is the one obtained by fitting the angular distribution calculated within BNV model with the method presented in [8] and recalled in Sect. 1.3. In Fig. 4.7 the integrated emission probability, calculated at energies of 8.1 and 15.6 MeV/u, is found to saturate around 200 fm/c implying that the emission probability is concentrated in an interval of ~ 150 fm/c after the collision. The time evolution of the cosine of the angle θ of the dipole with respect to the beam axis is plotted in Fig. 4.8. The fluctuations superimposed are caused by the coupling to isoscalar quadrupole and octupole surface modes in the entrance channel.

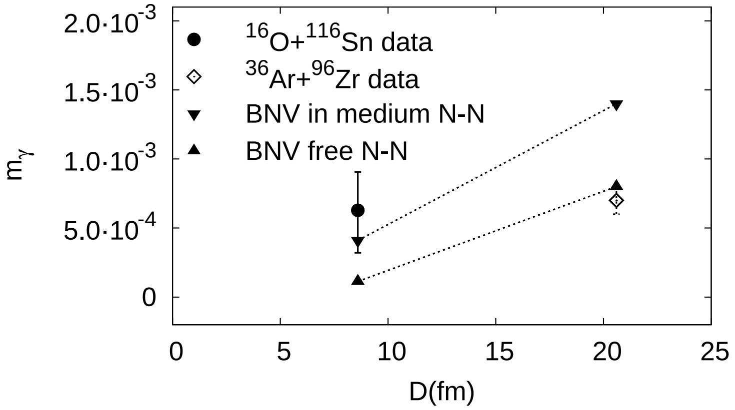

Figure 4.5: Measured and calculated DD multiplicities of ^{16}O + ^{116}Sn at 15.6 MeV/nucleon are compared with the ones reported in reference [19] for the reaction ^{36}Ar + ^{96}Zr at 16 MeV/nucleon. The lines are to guide the eye.

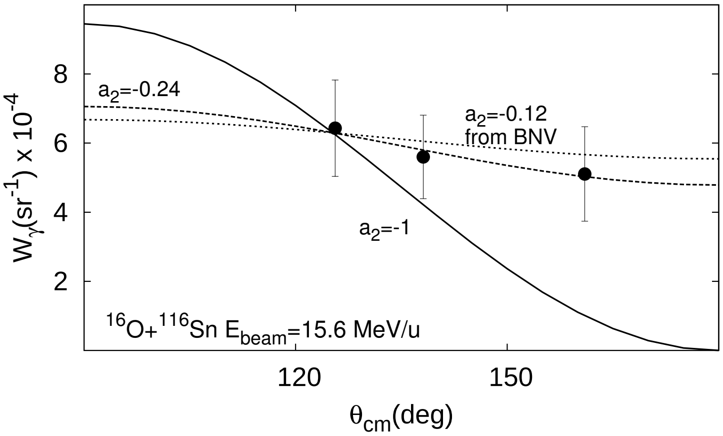

Figure 4.6: Measured angular distribution of γ-ray excess yield in the region E_γ = 10-20 MeV for E_{beam}= 15.6 MeV/nucleon compared with parameterizations using three different values of a_2.

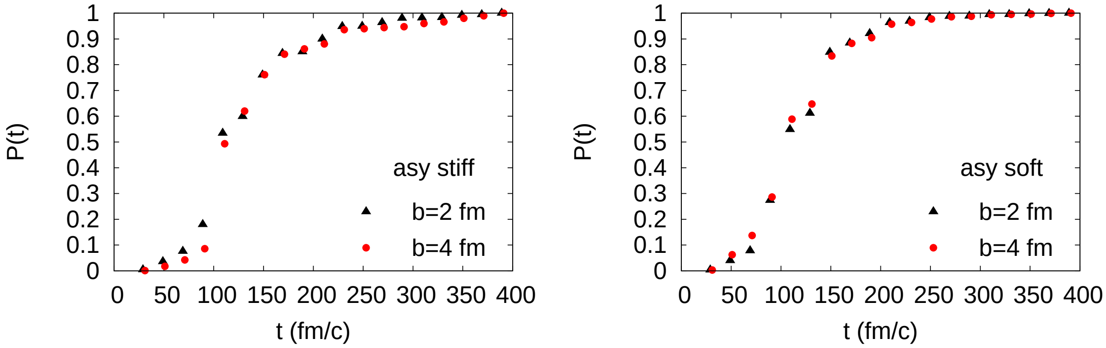

Figure 4.7: Integrated γ emission probability (left panel: E_{beam}=8.1 MeV/u, right panel: E_{beam}=15.6 MeV/u).

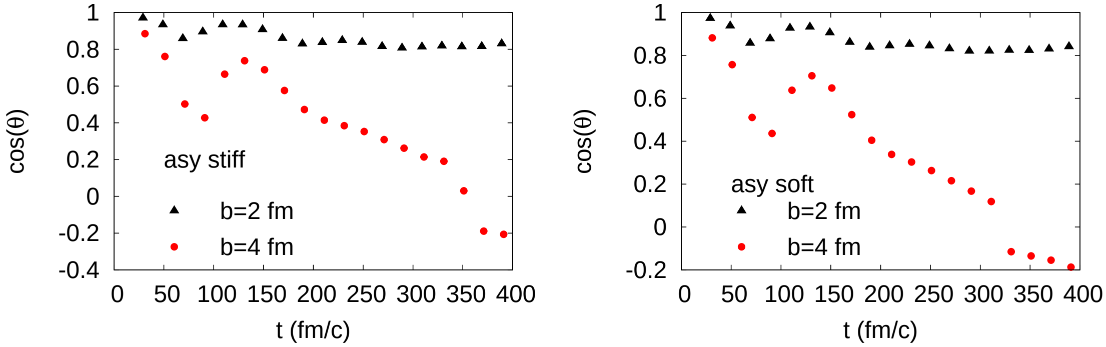

Figure 4.8: Time evolution of cos(θ), with θ defined as the angle between the beam axis and the dipole axis (left panel: E_{beam}=8.1 MeV/u, right panel: E_{beam}=15.6 MeV/u).

4.3.2 Measurement at E_{beam}=12 MeV/nucleon: preliminary results

In this section, we will present some preliminary results of the ongoing analysis of the γ decay measured in the reaction ^{16}O+^{116}Sn at 12 MeV/nucleon. The extra-yield associated with DD emission will be compared with the ones achieved at 8.1 and 15.6 MeV/nucleon, allowing to verify if a "rise and fall" trend exists also for ^{16}O+^{116}Sn as observed and predicted for other systems (see Sect. 1.4).

Data reduction

The events of interest for this analysis have been selected with a gate on fusion-evaporation residues as is displayed in the right panel of Fig. 4.9 and on the prompt γ peak (see Fig. 4.10, left panel). This double gate allows to select the fusion-evaporation events and reduces the random background as is shown in the right panel of Fig. 4.10.

The gated spectrum in Fig. 4.10 (right panel) is compared in Fig. 4.11 with the one calculated with Statistical Model (see App. B.1) and folded with the response function of HECTOR array.

The analysis of light charged particle emission is still ongoing; in order to have a preliminary estimate of the pre-equilibrium energy loss we have interpolated the values measured for the same reaction at beam energies 8.1 and 15.6 MeV/nucleon (see Tab. 4.2). With this procedure we have estimated a 17±3% energy loss, corresponding to 25.6±4.5 MeV. The GDR width adopted is the one obtained by linear interpolation of the width obtained by Statistical Model analysis of ^{132}Ce γ decay (see Fig. 4.2).

The most relevant inputs of the Statistical Model calculation are listed in Tab. 4.5; the input file is quoted in App. B.1.

Reaction	E_{beam} (MeV)	E^* (MeV)	E_{loss} (MeV)	E^*_{CN} (MeV)	S	E_{GDR} (MeV)	Γ (MeV)
^{16}O+^{116}Sn	192	155	25.6±4.5	129.4±4.5	1	14	12.4

Table 4.5: The GDR and reaction parameters used to calculate the statistical decay of ^{132}Ce populated with the reaction ^{16}O+^{116}Sn are listed: beam energy E_{beam}, excitation energy E^* from kinematics and Q-value, pre-equilibrium energy loss E_{loss}, CN excitation energy E^*_{CN} and GDR parameters (strength S, centroid E_{GDR} and width Γ).

The difference between measured and Statistical Model spectrum (normalized at 7 MeV) is plotted in the right panel of Fig. 4.11. It has a Lorentzian shape with the maximum at 13 MeV.

The increase associated with DD emission has been calculated with Eq. 4.2 and is plotted in Fig. 4.12 together with the values measured at the beam energies 8.1 and 15.6 MeV/nucleon:

$$increase(\%) = \frac{\int_{10MeV}^{22MeV} Y(E)dE - \int_{10MeV}^{22MeV} S(E)dE}{\int_{10MeV}^{22MeV} S(E)dE} \tag{4.2}$$

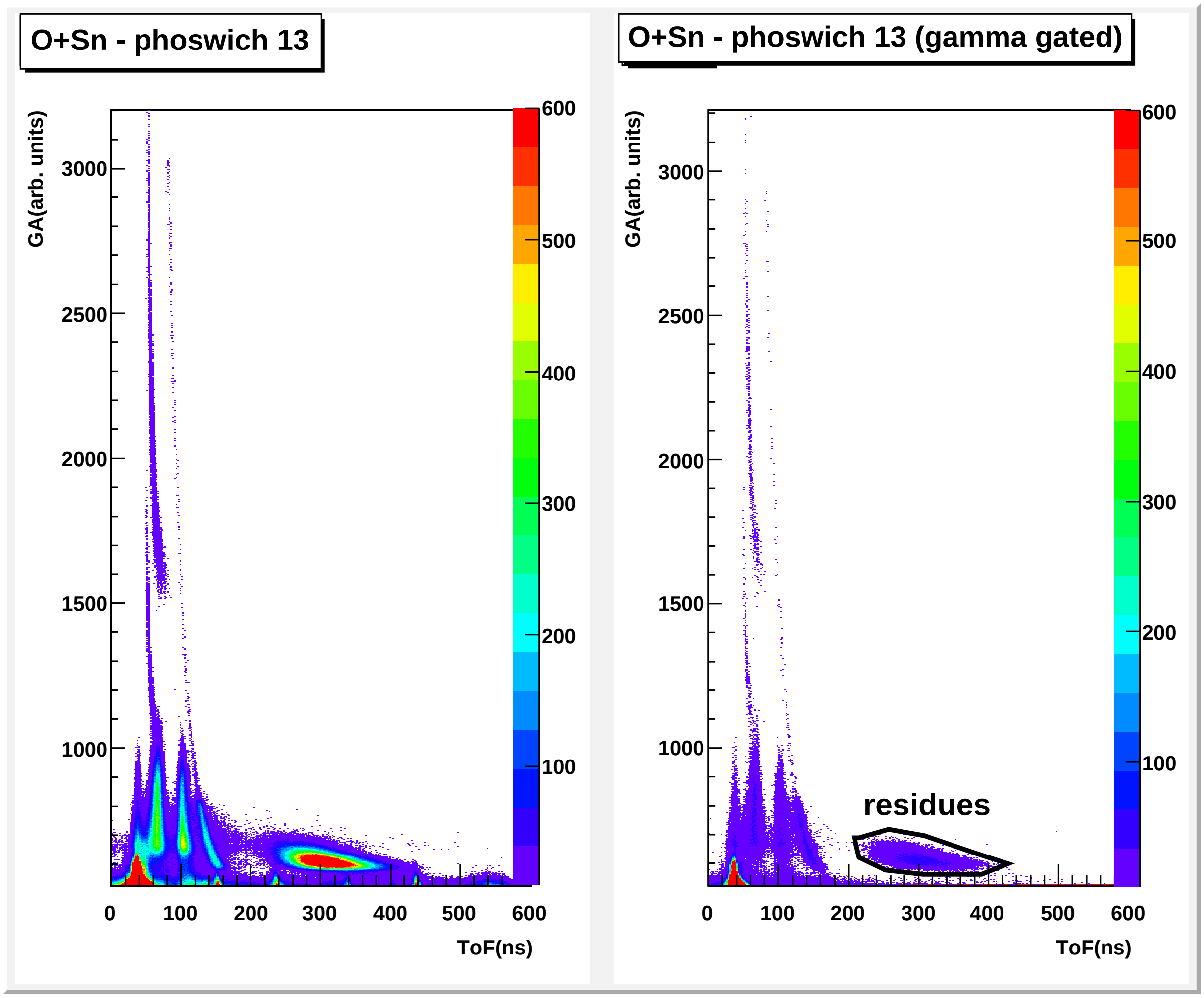

Figure 4.9: GA vs time of flight spectrum of one phoswich detector, with GA corresponding to the light output from the first scintillator layer. On the left the spectrum without conditions, on the right with a gate on the prompt γ peak. The evaporation residues are clearly separated from other events (encircled with graphical cut).

where Y(E) is the measured γ yield and S(E) is the one calculated within the Statistical Model.

Fig. 4.12 displays the beam-energy dependence of the increase in γ yield for the system under study with D=8.6 fm and for the ones with D $\sim$ 20 fm studied in [18, 19, 20] through the reactions ^{32}S+^{100}Mo and ^{36}Ar+^{96}Zr. Both systems have been measured at three different beam energies as listed in Tab. 1.1. The measured increases follow the same "rise and fall" trend with a maximum at the intermediate energy that is more pronounced for the system with the higher geometrical dipole moment D.

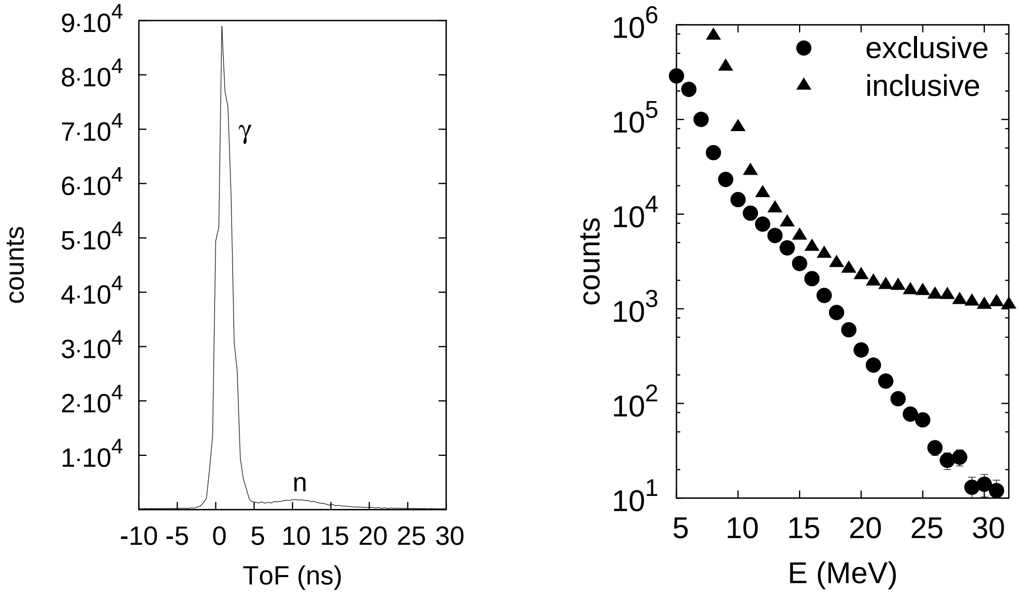

Figure 4.10: Left panel: time-of-flight spectrum of one HECTOR detector. The gate on the prompt γ peak is 4 ns wide, allowing to reduce significantly random coincidences and neutrons. Right panel: inclusive γ spectrum (triangles) compared with the one obtained with a gate on evaporation residues measured by the PHOSWICH detectors and on the prompt γ peak in the ToF spectrum of each HECTOR detector (dots).

BNV simulations

BNV calculations have been performed and analyzed with the same Bremsstrahlung approach used for the reactions at 8.1 and 15.6 MeV/u. In this case, 50 events have been simulated at each impact parameter b=0, 2, 4, 6 fm in order to reduce the numerical noise. A faster fusion dynamics (see Fig. 4.13, left panel) and a higher frequency of dynamical dipole oscillation (see Fig. 4.13, right panel) are found for the asy-soft parameterization of the density dependence of the symmetry term of the EOS. This is due to the fact that in the region probed by the first stages of the dynamical dipole oscillation (the neck developed between projectile and target) the density is lower than the saturation density and therefore the isospin-symmetry restoring force is stronger with the asy-soft parameterization with respect to the asy-stiff one (see Fig. 1.8). The centroid of the Bremsstrahlung spectrum obtained with the asy-soft parameterization is in fact $\sim$ 1 MeV higher than the one obtained with an asy-stiff parameterization.

The integral of the Bremsstrahlung spectrum yields, for each impact parameter, the DD γ multiplicity. Each impact parameter b can be associated with the corresponding angular momentum transferred to the CN in a fusion reaction within the semiclassical approximation:

$$\ell\hbar = \mu_{pro} v_{pro} b \tag{4.3}$$

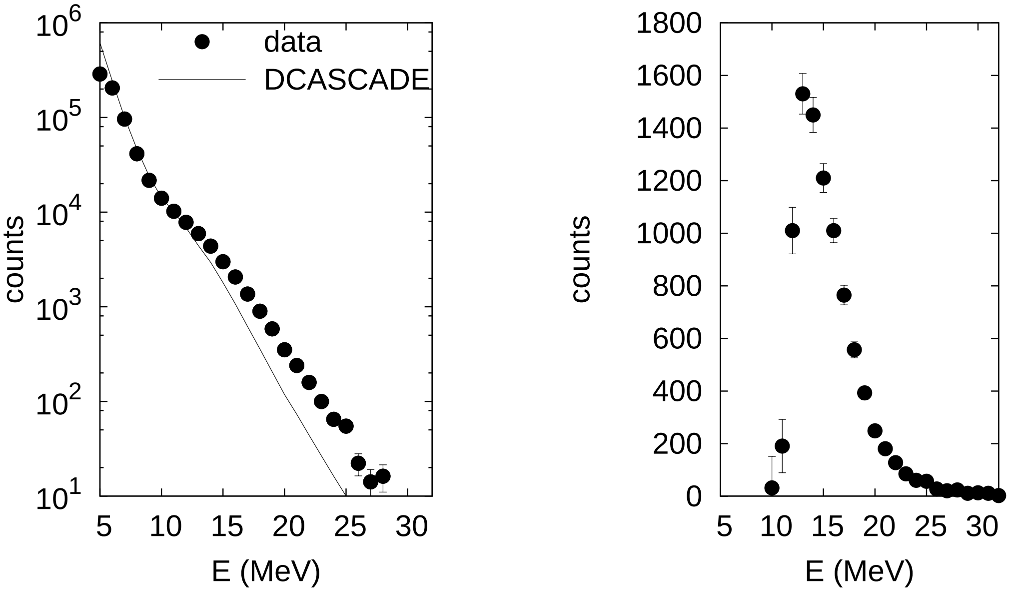

Figure 4.11: In the left panel, measured γ spectrum (dots) is compared with Statistical Model calculation (line). The difference between the two spectra of the left panel is plotted in the right panel.

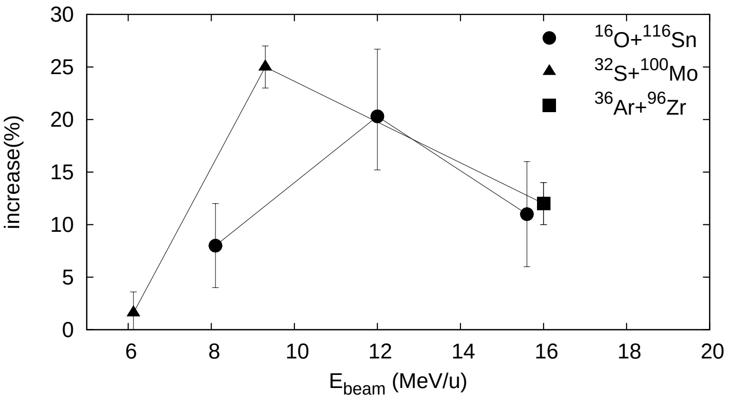

Figure 4.12: Increase of γ spectrum with respect to Statistical Model calculation (integrated between 10 and 12 MeV) obtained with Eq. 4.2.

where μ_{pro} and v_{pro} stand for projectile reduced mass and velocity, respectively. With this relation we have associated with each range of impact parameters (centered at b=0, 2, 4 and 6 fm) a range of angular momenta and the corresponding fusion cross section calculated with PACE4 code [66]. In this way we can perform a weighted average on the γ

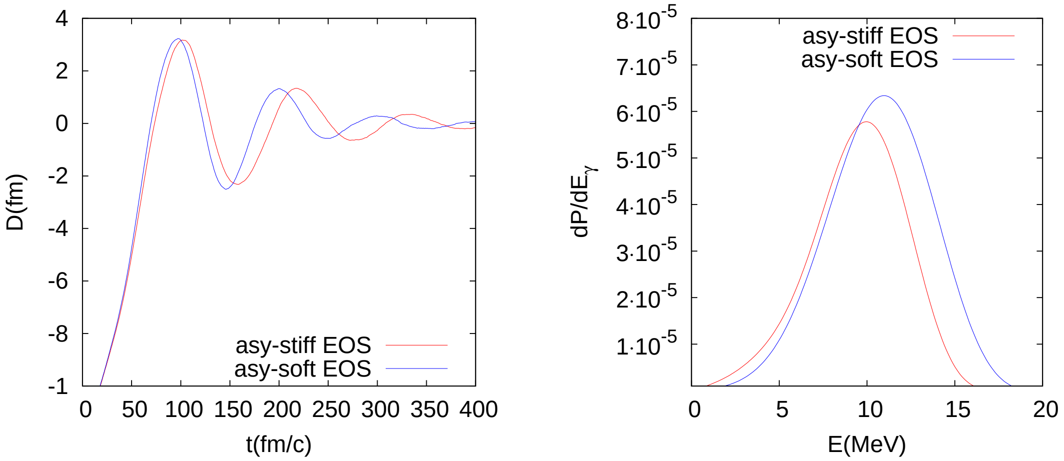

Figure 4.13: Results of BNV simulations of ^{16}O+^{116}Sn reaction at E_{beam}=12 MeV/u and impact parameter b=2 fm. Simulations are performed using an asy-stiff (red line) and an asy-soft (blue line) parameterization of the EOS. Dipole moment oscillation and the corresponding Bremsstrahlung spectrum are plotted in the left and right panels, respectively.

multiplicity corresponding to each range of impact parameters and obtain an overall DD γ multiplicity that can be directly compared to the measured one. The results obtained with this procedure are presented in Fig. 4.14 together with the ones already plotted in Fig. 4.4. From this preliminary analysis, DD γ multiplicity seems to display a flat dependence on beam energy per nucleon different from the one obtained for the experimental γ increase (see Fig. 4.12).

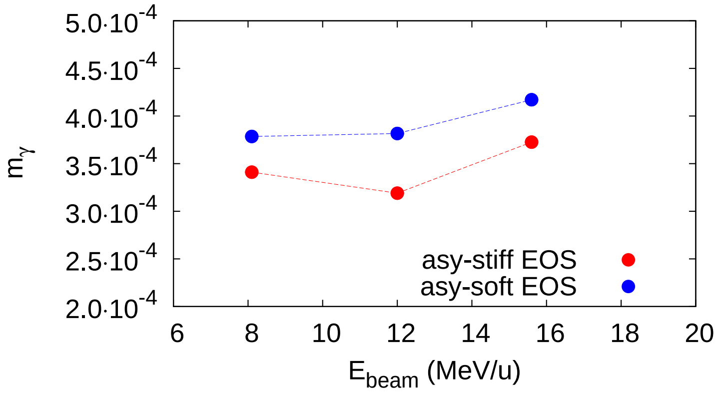

Figure 4.14: γ multiplicity integrated over the Bremsstrahlung spectrum as a function of beam energy. Each point is obtained by averaging on impact parameters b=0, 2, 4, 6 fm with a weight obtained from PACE4 fusion cross section.

Chapter 5

^{81}Rb and ^{80}Zr experiments: preliminary calculations

The analysis method that we use is based on the assumption that the statistical decays of ^{81}Rb* and ^{80}Zr* have the same features. The conditions that, if fulfilled, guarantee the validity of this assumption are that the average CN temperature, mass and shape are very similar. This implies that the GDR observables and the parameters used to describe the statistical decay will be the same.
The condition on mass is satisfied by choosing two CN with A=81 and 80, respectively, that can be assumed as equal in the description of statistical decay from hot nuclei. In this Chapter, we will present preliminary calculations showing that the conditions on temperature and shape are satisfied to a very good extent by the systems we have chosen, i.e. ^{81}Rb as a reference and ^{80}Zr as the system sensitive to the effect under study. The same kind of test will be done on the experimental data (see Chapt. 6).

5.1 Kinematics of the reaction

The internal energy of the CN can be calculated according to Eq. 5.1:

$$\begin{aligned} E_{int} &= E^* - < E_{rot} > \\ &= \frac{A_{pro}}{A_{pro} + A_{tar}} E_{beam} + Q - < E_{rot} > \end{aligned} \tag{5.1}$$

where A_x is the mass number of nucleus x (projectile or target), E_{beam} is the beam energy corrected for energy loss in the target, Q is the Q-value of the reaction and $< E_{rot} >$ is the average rotational energy after the formation of the CN. For these reasons the beam energies have been chosen in order to match E* (calculated with Eq. 5.1) after correcting E_{lab} for energy loss in the target, as shown in Tab. 5.1.

The beam delivered by the TANDEM-ALPI accelerator complex was pulsed with a frequency of 200 ns and a pulse width of ∼ 1 ns. The frequency has been chosen in order to allow fusion-evaporation residues to arrive in phoswich detectors before the forward

reaction	E$_{lab}$(MeV)	E$_{loss}$(MeV)	t($\mu g/cm^2$)	E*(MeV)	v$_{rec}$(cm/ns)	$\sigma(mb)$
^{37}Cl+^{44}Ca	153	3	500	83	1.3	1190
^{40}Ca+^{40}Ca	200	4	500	83	1.5	1080

Table 5.1: E$_{lab}$ is the energy of the incoming beam, E$_{loss}$ the energy loss in the target of thickness t, calculated with LISE++ code [67], E* the excitation energy calculated with Eq. 5.1, v$_{rec}$ the velocity of the recoiling CN, σ the fusion cross section calculated according to Bass Model with PACE4 code [66].

emitted α particles and protons belonging to the next bunch.
Fig. 5.1 displays the expected ToF spectrum of phoswich detectors calculated with Monte-Carlo Statistical Model (see App. C for explanations on Monte-Carlo Statistical Model and Sect. 3.4 for details on the response function of phoswich apparatus inside GARFIELD scattering chamber). The peak on the left corresponds to the overlap of α particles and protons emitted in forward direction while the bump on the right to fusion-evaporation residues.
Tab. 5.2 reports in detail the ToF that each reaction product takes to arrive in HECTOR and PHOSWICH detectors.

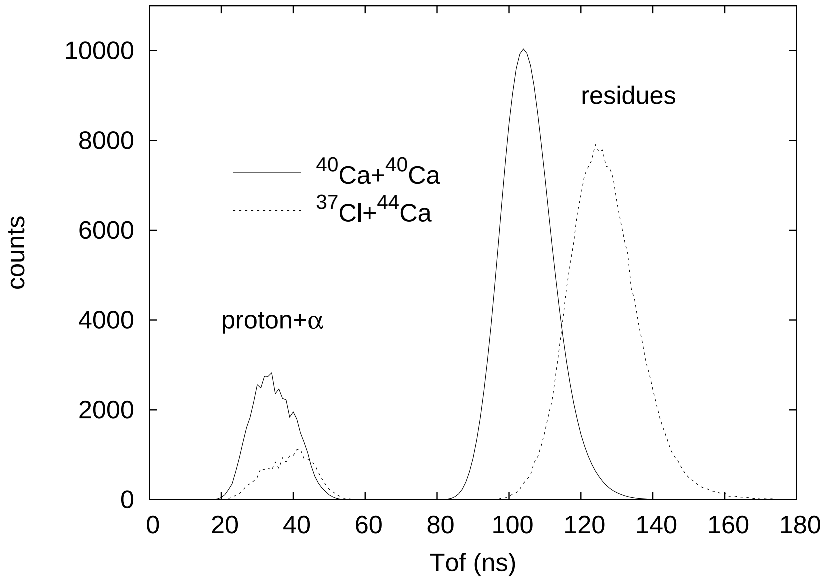

Figure 5.1: ToF spectrum measured by PHOSWICH detectors for light charged particles and residues produced by ^{37}Cl+^{44}Ca and ^{40}Ca+^{40}Ca reactions.

Detector	Residues	α	p	n	γ
^{37}Cl+^{44}Ca					
HECTOR	/	/	/	∼5	∼1
PHOSWICH	∼126	∼42	∼33	/	/
^{40}Ca+^{40}Ca					
HECTOR	/	/	/	∼5	∼1
PHOSWICH	∼104	∼9	∼32	/	/

Table 5.2: Average ToF (in ns) for each reaction product in PHOSWICH and HECTOR detectors. For neutrons in HECTOR, the Time of Flight is the one of the fastest neutrons. It is 4 ns longer than γ ToF in HECTOR, allowing to perform a good γ-neutron discrimination.

5.2 CN population and decay

5.2.1 CN spin population

In order to calculate $< E_{rot} >$ and, therefore, the mean internal energy of the CN, one has to perform an average on the rotational energy as a function of spin J (so called yrast line displayed in Figs. 5.2 and 5.3 for our systems) using the spin population distribution as a weight (see Fig. 5.4). In our calculation we have adopted the standard parameterization of the yrast line used within CASCADE Statistical Model calculation.
In the experiment, only events with a signal in PHOSWICH detectors are written on disk (see Chapt. 3). In order to take into account the effect of this kinematic selection on the phase-space population of the residues (and, consequently, angular momentum and internal energy available for the decay), fusion-evaporation kinematics has been implemented upon standard CASCADE Monte-Carlo output and phoswich-array geometry integrated into the code (see Appendix C for details). As one can qualitatively deduce from the kinematics of fusion-evaporation process, the residues entering the PHOSWICH detectors are the ones deviated from the beam trajectory. Deviation is due to recoil following particle emission, in particular α particles that are emitted preferentially from high-J states. Therefore, higher J residues are more likely to be detected by the PHOSWICH array.

With these ingredients we can calculate the internal energy after subtracting the energy of the rotational motion. The difference between the two systems is ∼5 MeV, that is within the sensitivity of the apparatus. In particular, the difference in spin population causes the rotational energy to be ∼5 MeV higher in ^{80}Zr and so reduces its internal energy. The average nuclear temperature has been calculated for the initial compound nucleus within CASCADE calculation. The J-dependent nuclear temperature

$$T(J) = \sqrt{\frac{E^* - E_{rot}(J)}{a(A, E^*, J)}} \tag{5.2}$$

has been averaged with the initial CN spin population as a weight in order to obtain

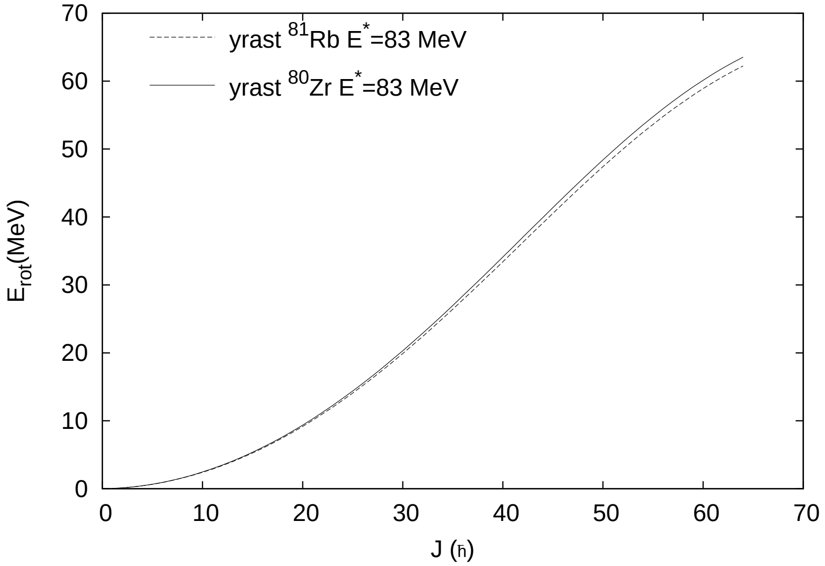

Figure 5.2: Yrast-line used within CASCADE Statistical Model calculations.

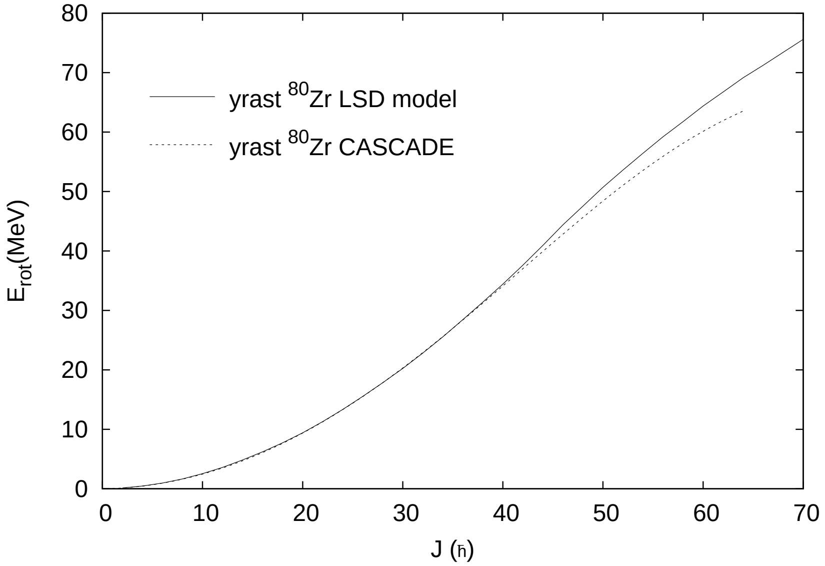

Figure 5.3: Yrast-line used within CASCADE Statistical Model calculations compared with the ones calculated according to Lublin-Strasbourg Liquid Drop Model [68, 69]

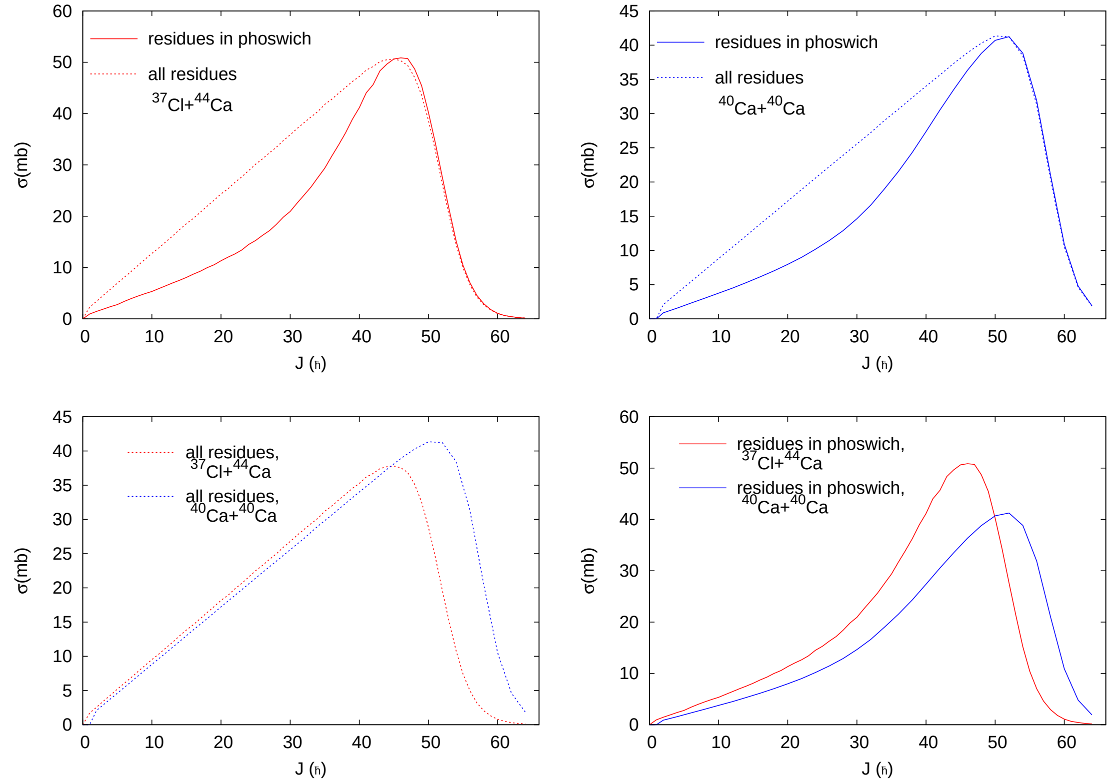

Figure 5.4: Spin population calculated with CASCADE Statistical Model. In the upper panels, the angular momentum selection induced by PHOSWICH detectors due to kinematics is displayed by comparing the total spin population (dashed lines) to the spin population of the residues entering the PHOSWICH detectors (full lines). The lower panels display the difference in spin population (both total and PHOSWICH-gated) between the two reactions.

T (Tab. 5.3). The level-density parameter a(A,E*,J) has been calculated according to Reisdorf parameterization [68, 69, 70]. As one can see in Tab. 5.3, the difference in average rotational energy induces a small temperature difference of 0.2 MeV. The associated change in GDR parameters (namely the width that is the only temperature-dependent parameter) is well beyond the sensitivity of this kind of measurements.

5.2.2 Light-particle evaporation

The spectrum of light particles evaporated by CN has a shape given by the overlap of distributions of this kind:

$$\frac{dP}{dE} = \frac{N}{4\pi T^2}(E - V_c)exp(-(E - V_c)/T) \qquad (5.3)$$

CN	$< J >$ ($\hbar$)	$< J^p >$ ($\hbar$)	$< E_{rot} >$ (MeV)	$< E^p_{rot} >$ (MeV)	T (MeV)	T^p (MeV)
^{81}Rb	34	38	27.46	32.04	2.3	2.2
^{80}Zr	38	42	33.10	37.86	2.2	2.1

Table 5.3: The average angular momentum $< J >$ and $< J^p >$, rotational energy $< E_{rot} >$ and $< E^p_{rot} >$ and nuclear temperature T. Average is performed with the whole and PHOSWICH-gated spin population (labeled with p superscript) calculated with a Monte-Carlo version of CASCADE code.

where V$_c$ is the Coulomb barrier, N is a normalization factor and T is the temperature of the emitting source (i.e. of the CN in the different steps of the decay). Therefore, the slope of the light charged particle spectra probes the average temperature of the decaying CN. For this reason, a comparison of the light charged particle spectra emitted by the two CN under study may confirm the validity of our calculations predicting a very similar temperature for the two systems (see Tab. 5.3).
Indeed different particles may probe slightly different temperatures, depending on the branching ratio between the different kinds of emissions along the decay chain which runs from the initial CN temperature down to almost zero temperature. This remark has to be taken particularly into account since we are comparing a system in the stability valley (^{81}Rb) with one close to the proton drip line (^{80}Zr) (Fig. 5.5), where the proton binding energy is very low and proton emission has the higher branching ratio in the first steps of the decay.

Therefore, we have verified via Statistical Model calculations if the LCP spectra can be directly compared. Comparison is shown in Fig. 5.6. The spectra of Fig. 5.6 show a good overlap of the slopes; the difference in the maximum of α-particles spectra may be due to a difference of $\sim$ 1 MeV in the Coulomb barriers for the two systems.

As remarked in Subsect. 5.2.1, the effect of PHOSWICH kinematic selection has to be taken into account and is shown in Fig. 5.7. A correlation between a higher-energy α (emitted in the first decay steps) and a residue in the PHOSWICH detectors can be observed as suggested in Subsect. 5.2.1. Consequently, one has to verify if under this geometrical constraint the LCP spectra of the two reactions are the same.

Multiplicity of light-particle emission has been calculated with a Monte-Carlo version of CASCADE code and is reported in Tab. 5.4. The high multiplicity of protons emitted by the proton-dripline nucleus ^{80}Zr can be noted.

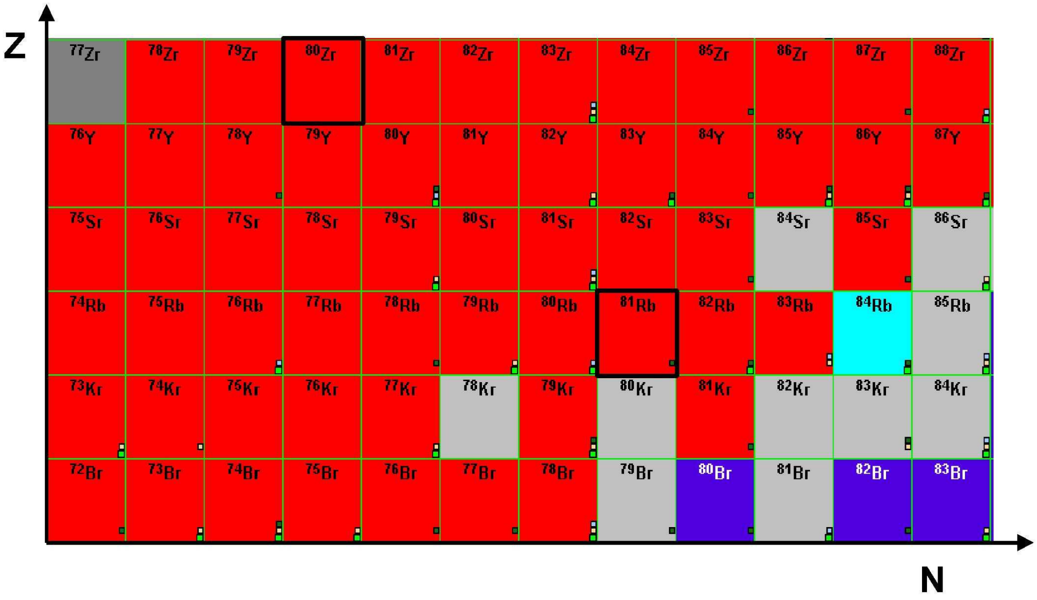

Figure 5.5: Region of the nuclear chart where ^{81}Rb and ^{80}Zr are situated.

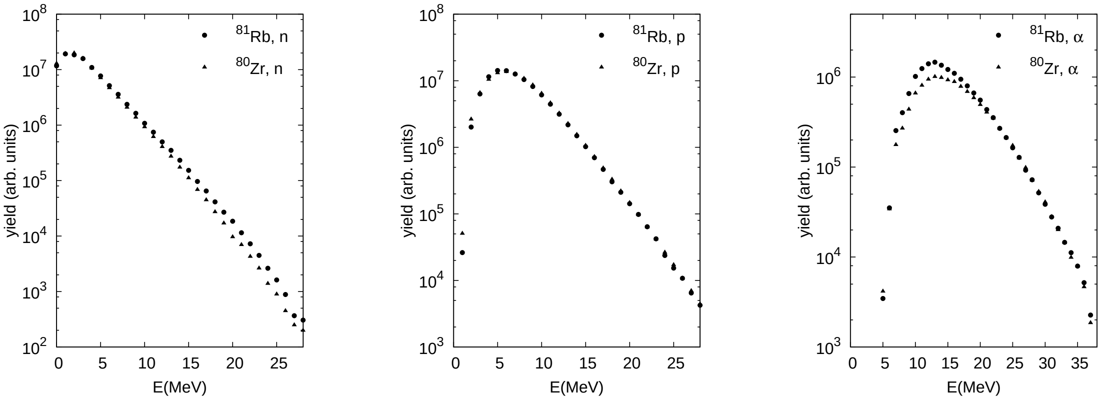

Figure 5.6: Light-particle multiplicity spectra calculated with a Monte-Carlo version of CASCADE Statistical Model code. The integral of the spectra is normalized to an arbitrary value in order to better compare the spectral shapes.

CN	α	proton	neutron
^{81}Rb	1.18	1.15	2.37
^{80}Zr	1.44	3.47	0.29

Table 5.4: Multiplicity of light particles emitted by the CN under study as calculated with Monte-Carlo CASCADE code.

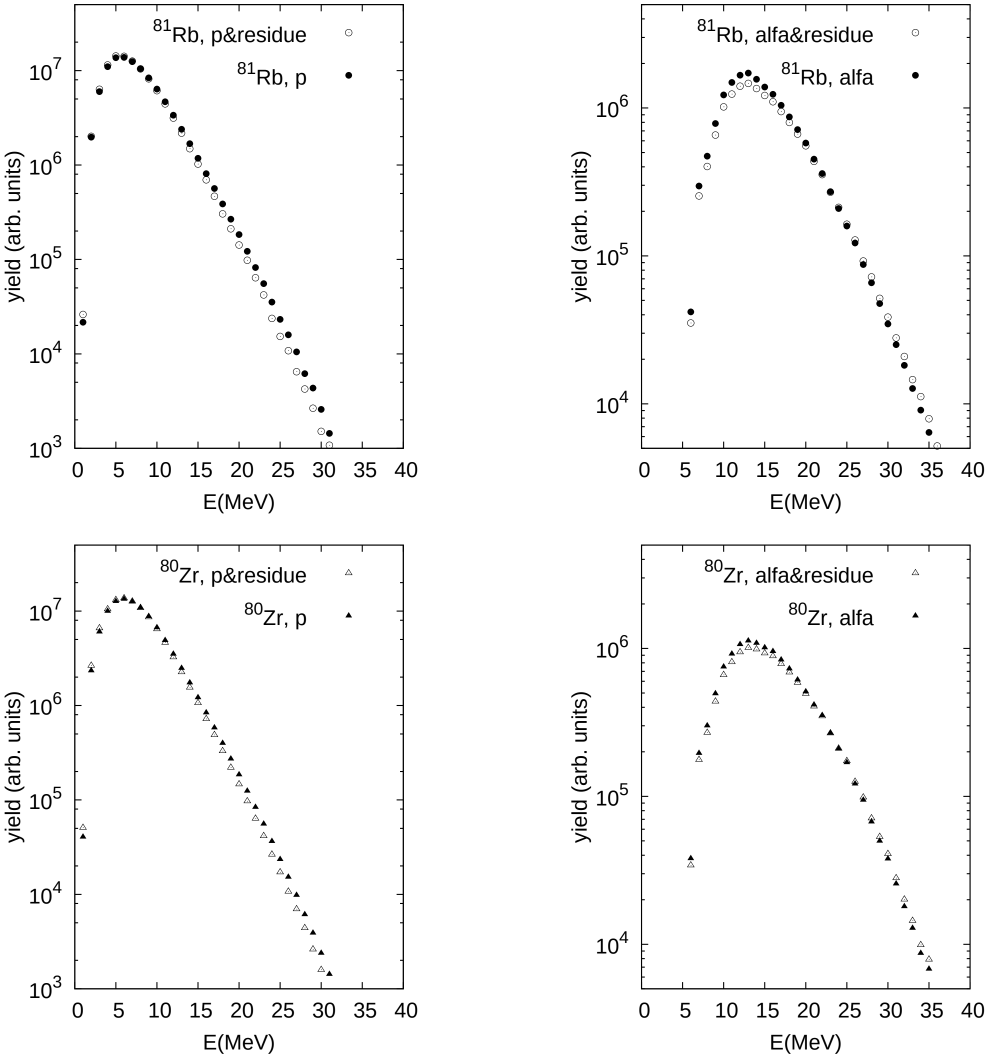

Figure 5.7: Light-particle multiplicity spectra calculated with a Monte-Carlo version of CASCADE Statistical Model code, with (hollow symbols) and without PHOSWICH kinematic selection on the events (full symbols). The integrals of the spectra are normalized to an arbitrary value in order to better compare the spectral shapes.

5.2.3 GDR systematics

CN and GDR properties of the two systems under study have been investigated preliminarily. The systems closer to the ones under study that can be found in Schiller systematics [71] are reported in Tab. 5.5.

CN	E* (MeV)	⟨J⟩ ($\hbar$)	S	E (MeV)	Γ (MeV)	E_w (MeV)	FWHM (MeV)
^{63}Cu	77.4	23	0.9±0.1	16.4±0.3	10.6±0.6		
^{76}Kr	54	19	1.3	15.5±0.63	7.0±0.63		
^{90}Zr 1	75		0.36±0.13	14.6±0.5	5.24±0.88		
^{90}Zr 2	75		0.68±0.14	18.2±0.6	9.07±0.77	17.0	9.67±0.39
^{92}Mo 1	93.5		0.22±0.34	14.0±1.7	4.78±2.5		
^{92}Mo 2	93.5		0.93±0.36	17.9±1.4	12.78±2.37	17.2	12.08±0.97

Table 5.5: GDR parameters from Schiller *et al.* systematics for nuclei close to A∼80 and E*=83 MeV. If a splitting of the GDR strength has been observed, also the centroid energy weighted on the strength of the two components (labeled with subscript w) and the FWHM of the cross-section parameterization is presented.

As one can see, ^{80}Zr and ^{81}Rb in our experimental conditions are not available in Tab. 5.5, therefore we can only infer the range of values where we expect to find GDR parameters of ^{80}Zr and ^{81}Rb.
It has been demonstrated within Nilsson-Strutinsky approach that for non-magic nuclei at T $\geq$ 1.5 MeV shell structure has dissolved and the nucleus can be described as a liquid drop. The potential energy maps in Fig. 5.8 show the angular-momentum induced deformation of ^{80}Zr and ^{81}Rb nucleus calculated with the Lublin-Strasbourg Liquid Drop Model [69], which extends the original Liquid Drop Model with an explicit introduction of the surface-curvature terms.

At finite temperature the average deformation may differ significantly from the one corresponding to the minimum of the potential energy curves due to thermal shape fluctuations (see Subsect. 2.4.1). We have calculated the average deformation parameter $\langle\beta(\mathrm{J,T,A})\rangle$ using the formula given in [57]:

$$\langle\beta(J,T,A)\rangle = \frac{8}{3\sqrt{\pi}}\sqrt{\frac{T}{C_0}w_1(\xi)^{4/(T+3)}} \tag{5.4}$$

where ξ=J/A$^{5/6}$, w$_1$=1+$\frac{c_1}{1+exp[(c_2-\xi)/c_3]}$ (c$_i$=(4.3, 1.64, 0.31)) and C$_0$=1/2 $\delta^2 F/\delta\beta^2|_{\beta=0}$, and with F being the free energy from Liquid Drop Model. Inverting the linear relation between β and Γ presented in Fig. 2.9, we obtain the following relation:

$$\Gamma = \Gamma_0 + \frac{E_0}{0.8}(\beta - 0.12) = \Gamma_0 + \Delta\Gamma \tag{5.5}$$

If Γ_0 is known, Eq. 5.5 allows to evaluate the width Γ of the GDR built on the nucleus deformed by temperature and rotation. This datum is available for ^{81}Rb (see Tab. 5.6)

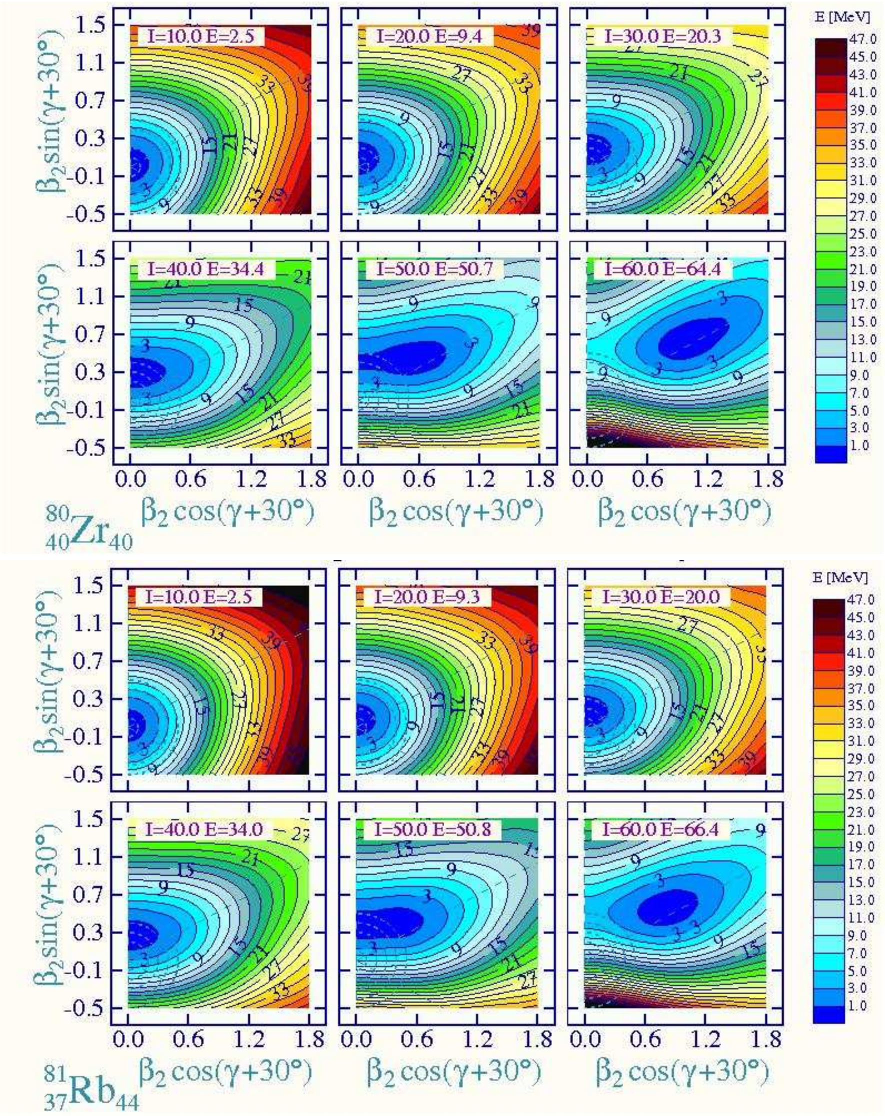

Figure 5.8: Maps of macroscopic energy of ^{80}Zr and ^{81}Rb as a function of β, γ coordinates for six values of angular momentum. Calculations were performed with the Lublin-Strasbourg Liquid Drop Model [68, 69].

but not for ^{80}Zr, for which we have to follow another, more qualitative, approach.

The intrinsic width Γ_0 is expected to have a minimum value for closed-shell nuclei. Therefore, we expect that for ^{80}Zr, with N=Z=40 corresponding to a subshell closure (given by the filling of *fp* orbitals [72]), Γ_0 is lower than in the nuclei with similar mass as ^{81}Rb, thus compensating the higher $\Delta\Gamma$.

Furthermore, we have observed that in the isotopic chains where no neutron (sub)shell

CN	β	Γ_0(MeV)	$\Delta\Gamma$(MeV)	Γ(MeV)
^{81}Rb	0.44	4.5	6.47	10.9
^{80}Zr	0.49	/	7.37	/

Table 5.6: β and $\Delta\Gamma$ are calculated according to Eqs. 5.4 and 5.5. Γ_0 of ^{81}Rb has been obtained in photoabsorption experiments [48] but is not available for the proton-rich nucleus ^{80}Zr.

closures are involved, the intrinsic width decreases approaching the proton drip line, as shown in Tab. 5.7.

Both remarks allow us to conclude that Γ_0 in ^{80}Zr is less than in ^{81}Rb, and therefore the width Γ to be used in the Statistical Model calculations (see Chapt. 7) should be very similar.

A	76	78	80	82
Se	5.4	5.7	6.9	5.9

A	116	118	120	124
Sn	4.2	4.8	4.9	4.8

Table 5.7: Systematics of GDR intrinsic width Γ_0 (in MeV) for Se and Sn isotopes.

Also for γ emission, kinematic selection following detection of a residual nucleus by the PHOSWICH detectors has an effect that is shown in Fig. 5.9 and will be taken into account as described in App. B.

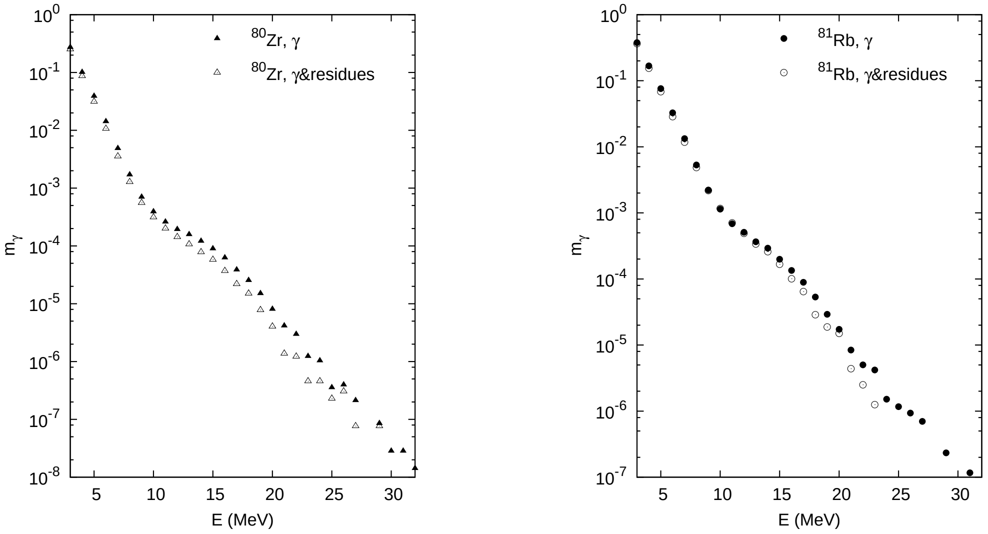

Figure 5.9: γ-multiplicity spectra calculated with a Monte-Carlo version of CASCADE Statistical Model code, with (hollow symbols) and without (filled symbols) phoswich kinematic selection on the events.

Chapter 6

^{81}Rb and ^{80}Zr experiments: data reduction

In this chapter, we will give details on calibration and event identification for each detector, pointing out the gating conditions used to select the events of interest for the subsequent analysis. In conclusion, we will also discuss several details of the data-reduction procedure that we regard as closely linked to the features of this setup and to the running conditions of the experiment. A clear understanding of these aspects was crucial in order to properly reduce and interpret the data.

The analysis code is based on ROOT Data Analysis Framework [73]. After calibration of time and energy signals and alignment of peaks in Time-of-Flight (ToF) spectrum (see also Sect. 6.5), a subset of the original dataset obtained with a gross selection has been rewritten preserving the event-by-event structure using the methods of the Class TTree of ROOT. The selection of physical events has been done starting from this reduced dataset, keeping in mind that the GDR decay in fusion-evaporation reactions has the following signatures in our detection apparatus:

- detection of one fusion-evaporation residue in PHOSWICH detectors
- detection of one high-energy γ-ray in HECTOR detector
- detection of one (or more) light charged particle in GARFIELD or PHOSWICH detectors

6.1 PHOSWICH analysis

The first step in the analysis of PHOSWICH detectors has been the calibration of the ToF. Actually, only the analog TDC (Time-to-Digital Converter), used to process the RF signals, needs to be calibrated. The calibration of this channel, as well as the calibration of the ones used for HECTOR and Plastic time signals, has been performed with a pulse generator. A typical time spectrum of the pulse generator is shown in Fig. 6.1 We have, therefore, calculated the ToF using Eq. 3.1. An alignment procedure has been performed,

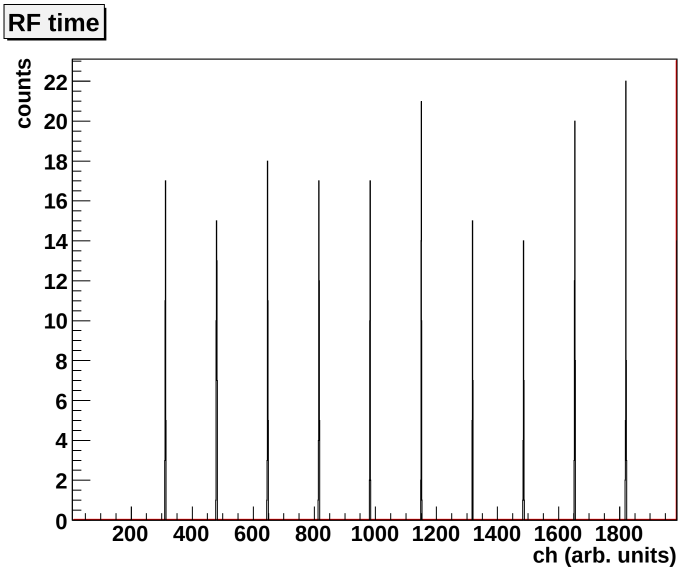

Figure 6.1: Time spectrum of pulser used to calibrate all the analog TDCs (in this case, the one used for RF signal). The peaks are equally spaced at time intervals of 20 ns.

as described in Sect. 6.5.
GA, GB and GC variables (light output from the three scintillator stages, see Sect. 3.4) have been used without calibration (that is unnecessary and demands dedicated in-beam measurements). Therefore, we will not be able to show energy spectra from PHOSWICH detectors.
Residues identification has been done using the correlation between GA and ToF as shown in Fig. 6.2. A better separation of the evaporation residues from other reaction products is achieved in the two-dimensional spectra after gating on the prompt gamma peak in HECTOR detectors (see Fig. 6.13) as displayed in the right panels of Fig. 6.2. In Fig. 6.3, ToF spectra corresponding to evaporation residues, protons and α's are compared with the ones calculated with CASCADE Monte-Carlo code and filtered by PHOSWICH response function (see Fig. 3.11).

We point out that GA is not proportional to the kinetic energy of the detected particle for different ranges of A, Z and kinetic energy. In fact, while elastically scattered beam particles and fusion-evaporation residues are stopped in the first stage, light charged particles punch through the first scintillator stage (and part of the protons also through the second stage). The range in the first scintillator material (BC404) of a recoiling heavy ion like ^{80}Zr with a kinetic energy of 98 MeV is $\sim$22 μm, while the thickness of this layer is 200 μm. Conversely, α particles with energy higher than $\sim$ 14 MeV and protons with energy higher than $\sim$ 3.7 MeV punch through the first layer. Therefore, light-particle identification can be also obtained studying the correlation between light outputs from first and second (or second and third) scintillator stages, as shown in Fig. 6.4 (6.5)

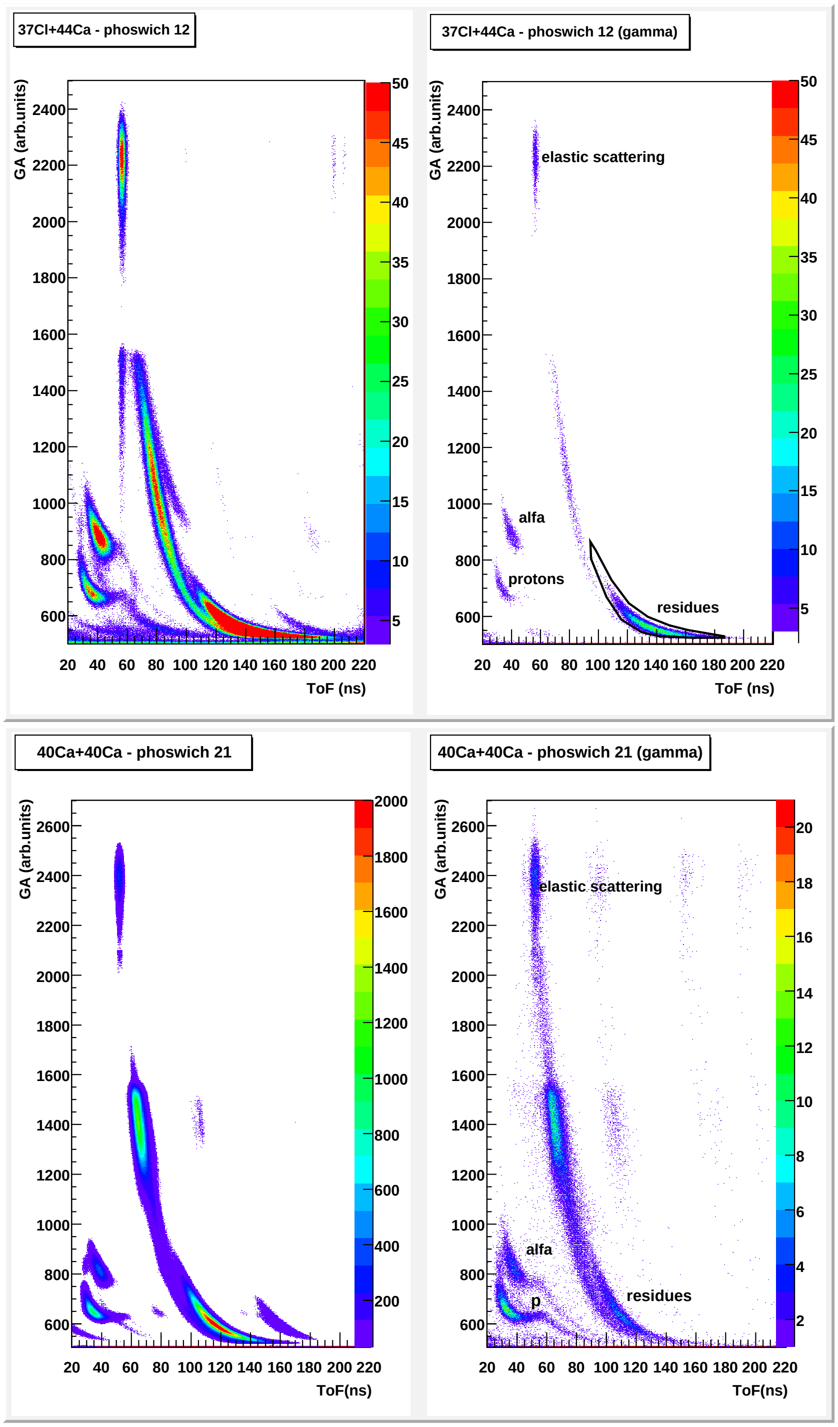

Figure 6.2: GA vs Time of Flight for Cl+Ca (upper panel) and Ca+Ca (lower panel). The two-dimensional spectra in the right panels are gated on values of HECTOR ToF corresponding to prompt gamma peak (see Fig. 6.13), thus reducing random coincidences. Graphical cuts enclose the fusion-evaporation residues.

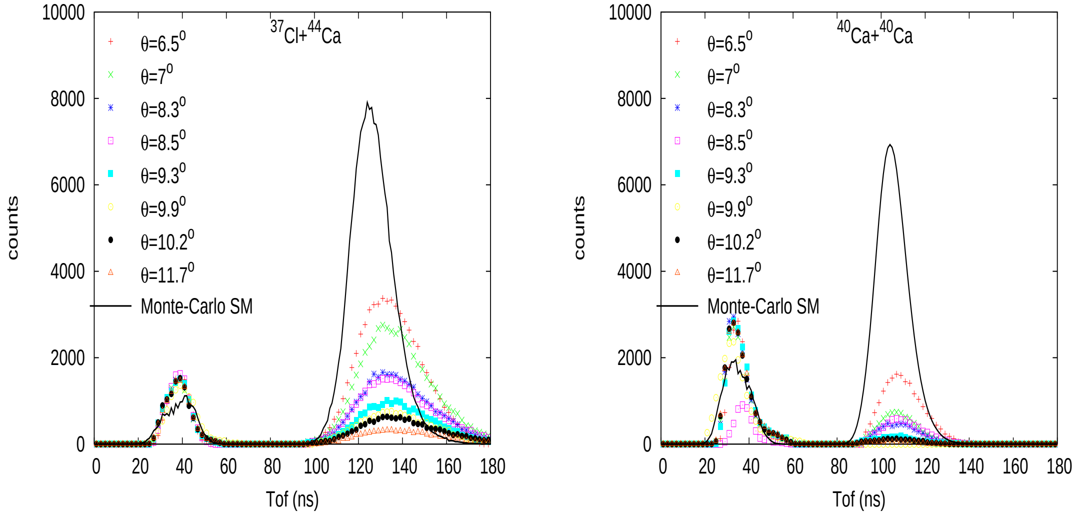

Figure 6.3: ToF spectra of residues and light charged particles in phoswich detectors for Cl+Ca (left) and Ca+Ca (right) reactions. The spectra of PHOSWICH detectors centered at the same θ angle are summed and compared with a calculation performed with a Monte-Carlo version of CASCADE Statistical Model code (see App. C). Global response function of all PHOSWICH detectors is included in the analysis of Monte-Carlo output.

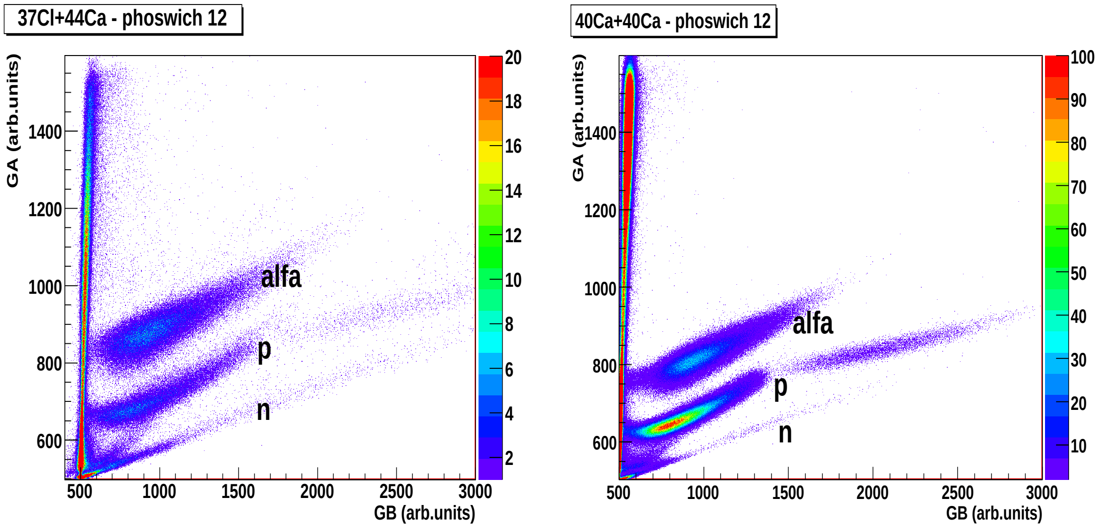

Figure 6.4: GA vs GB matrix for Cl+Ca (left) and Ca+Ca (right). The line almost parallel to y-axis corresponds to events stopped in the first layer, i.e. evaporation residues and scattered beam particles. The lines corresponding to light particles are well identified and labeled (the label “n” includes also γ rays). The change of slope, more evident for protons in Ca+Ca, corresponds to particles punching through the second layer.

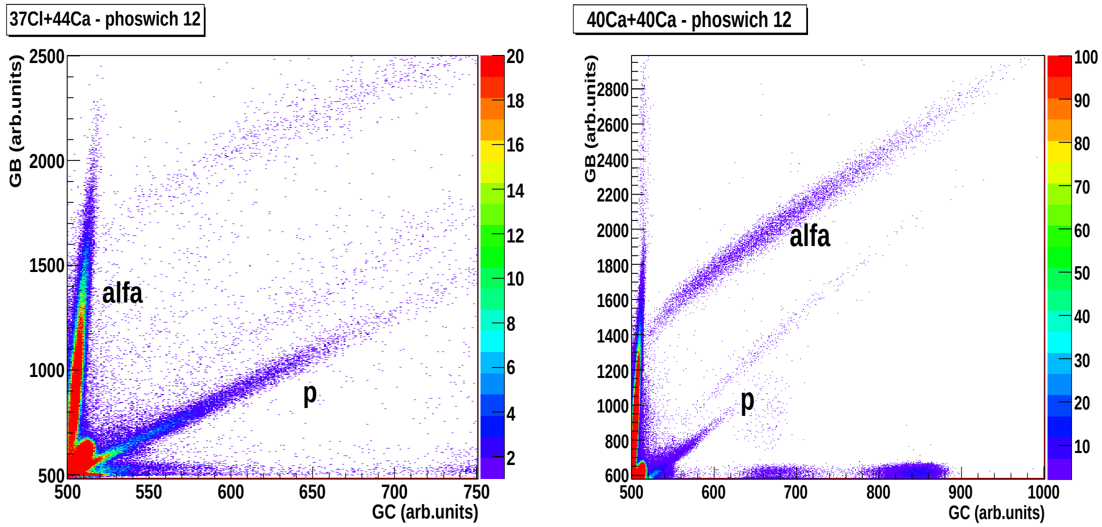

Figure 6.5: GB vs GC matrix for Cl+Ca (left) and Ca+Ca (right). The line almost parallel to y-axis corresponds to events stopped in the first and second layers. The lines corresponding to light particles punching through the second layer are labeled and correspond to faster protons and α's.

6.2 GARFIELD analysis

The energy spectrum of the light charged particles has been analyzed in order to probe the nuclear temperature as explained in Subsect. 5.2.2. Light charged particles are detected both in the GARFIELD and PHOSWICH array but only the first one yields information on their energy.

The first step of the calibration of energy spectra from CsI detectors (GARFIELD E) is the isotopic identification. This was performed with an automatic procedure [74] to track and identify the ridges corresponding to different isotopes in the two-dimensional spectrum fast vs slow psa (slow psa=3.5 × (slow - 4 × fast), see Sect. 3.3). As shown in Fig. 6.6, only Z=1,2 isotopes are detected at this low excitation energy (83 MeV). The quality of the identification is classified with a code ranging from 0 to 5, corresponding to the distance between a measured point and the identification line. In this analysis, we take into account only signals with a code ≤ 3 after having verified that this choice is a good compromise between discarding the events not well identified and preserving the spectral shape.

The result of the identification procedure is to associate with each cell of the fast vs slow psa matrix an A,Z value that is needed in order to apply the formula that converts light output (LO) in energy. In fact the differential energy loss of each light charged particle in CsI is different as accounted for by Birks formula [75]

$$LO = \gamma E + \beta(exp(-\alpha E) - 1) \tag{6.1}$$

where α, β and γ are isotope-dependent parameters. Before inverting and applying a formula similar to Eq. 6.1, the light output of our experiment has to be normalized to the value used to build the theoretical formula. This calls for calibration measurements with elastic scattering reactions, where the A, Z and energy of the detected particle are well known. The same calibration measurements are adopted for several experiments, so a further normalization has to be done to account for changes (e.g. in the gain settings). This normalization is done for each experiment with a calibrated pulser.

Once calibrated, the energy spectra have to be transformed from the laboratory to the center of mass (CM) frame. This transformation has been done, event by event, with the following relation:

$$E_{cm} = E_{lab} + \frac{1}{2}mv_s^2 - 2cos(\theta)\sqrt{\frac{1}{2}mv_s^2 E_{lab}} \tag{6.2}$$

where the velocity of the emitting source v_s is taken as the velocity of the recoiling compound nucleus, see Tab. 5.1.

Emission from a thermalized system is expected to be isotropic in the center-of-mass (CM) reference frame. The comparison between CM energy spectra measured at different polar angles θ=60°, 47°, 35° is shown in Fig. 6.7. The overlap of the slopes of the spectra detected at different angles is a signature of the absence of pre-equilibrium emission, while the difference in the maximum positions is due to the electronic thresholds.

In Fig. 6.8 we compare the CM energy spectra of α particles and protons. The spectra overlap and have the same slope, which we take as a signature of the fact that the effective temperatures of ^{80}Zr and ^{81}Rb CN are very similar. The comparison is shown for three different CsI's centered at different angles with respect to the beam axis.

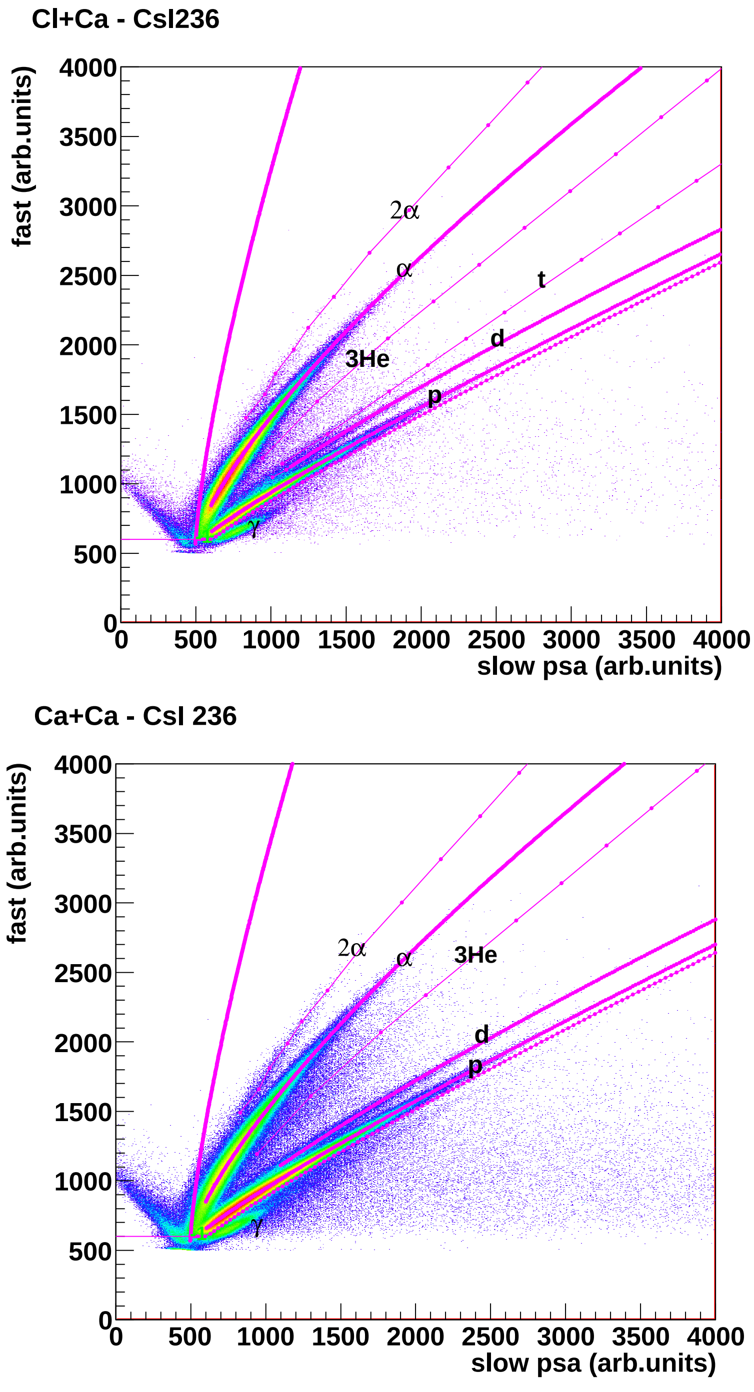

Figure 6.6: Fast vs slow psa correlation, with slow psa=3.5 × (slow - 4 × fast), for Cl+Ca (top panel) and Ca+Ca (bottom panel). Ridges corresponding to different isotopes are labeled and tracked with identification lines. The line labeled as 2α corresponds to the pile up of two α particles coming from $^{8}\mathrm{Be}_{gs}$ decay while the outer lines delimit the region of the matrix where light charged particles lie from the region where neutrons, γ's and badly identified events are found.

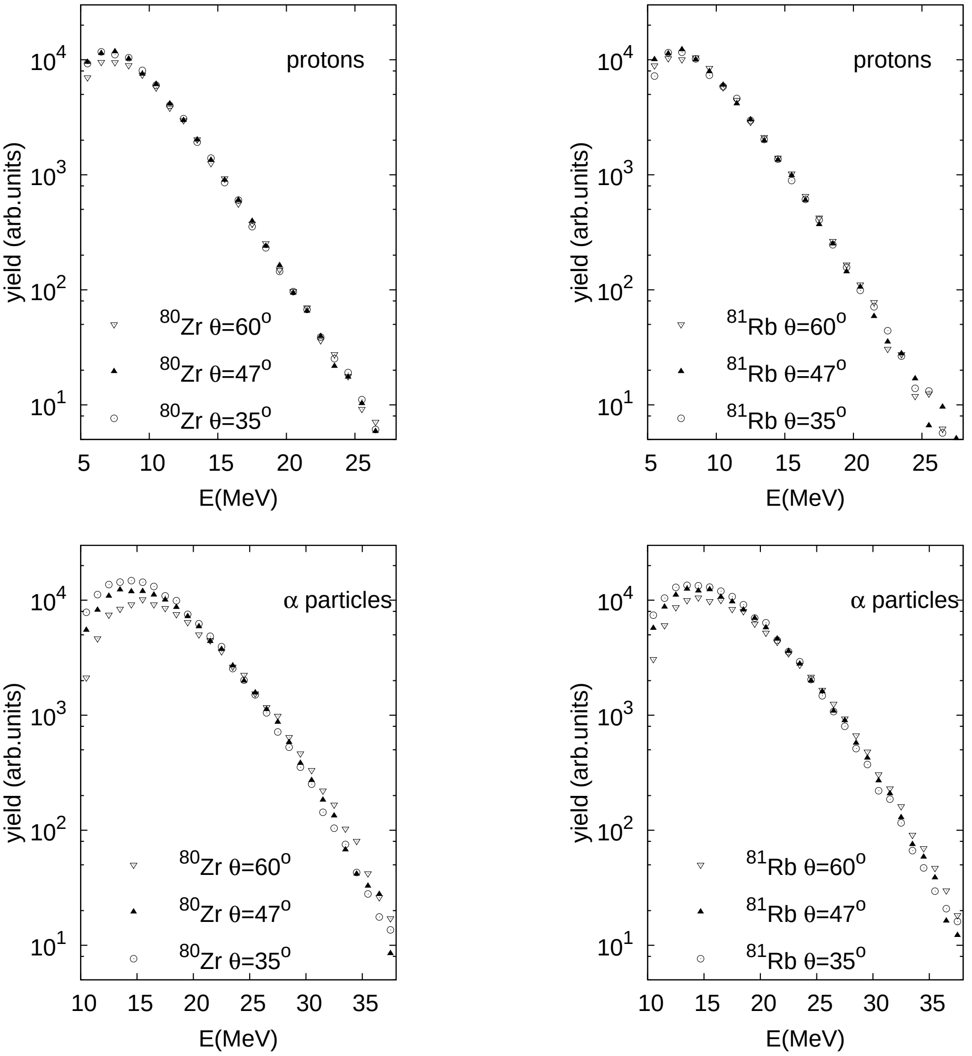

Figure 6.7: Energy spectra of protons (top) and α particles (bottom) emitted from ^{80}Zr (left) and ^{81}Rb (right) CN. Comparison is made between the spectra detected at different angles normalized for the sake of comparison.

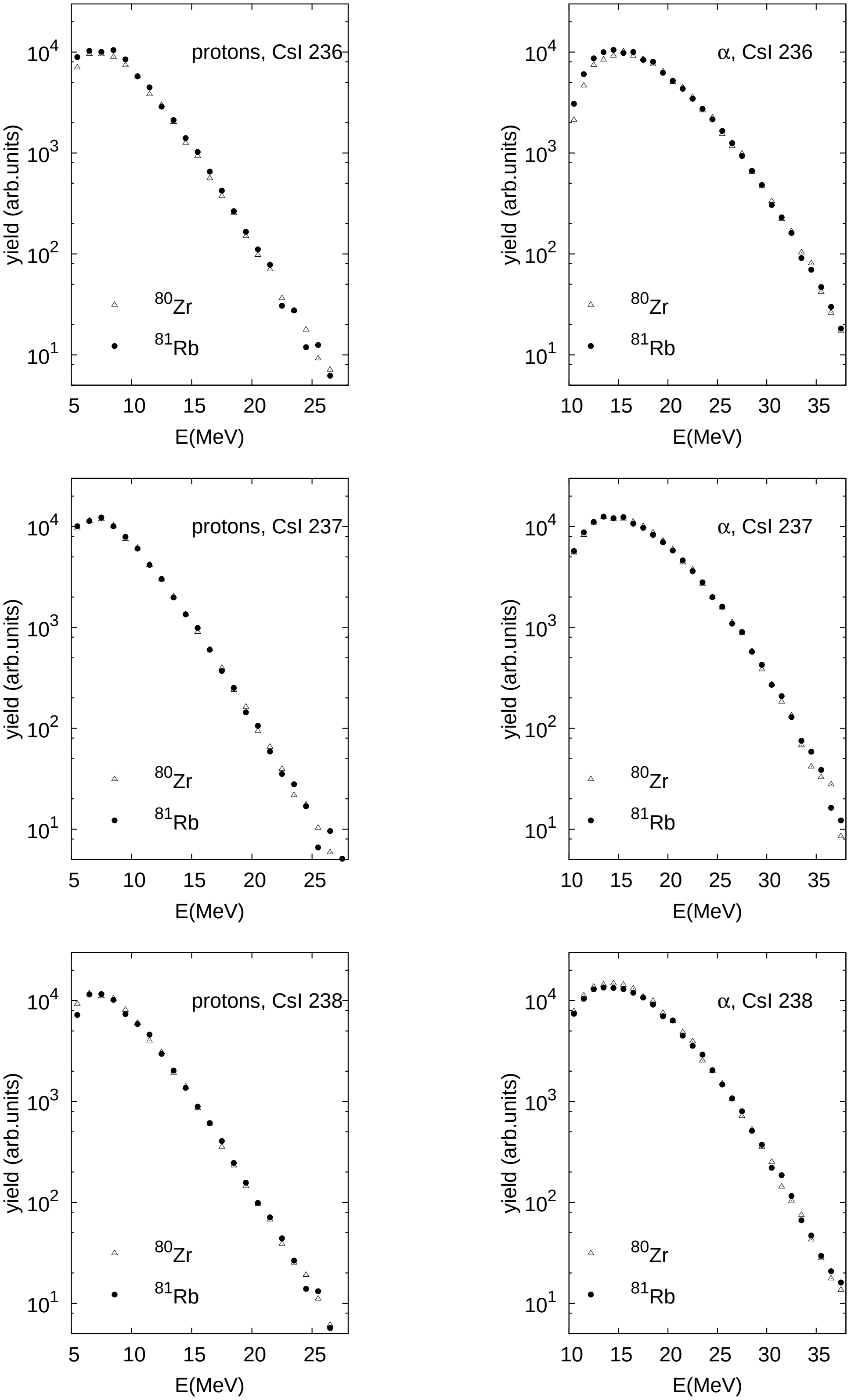

Figure 6.8: Center-of-mass energy spectra of protons (left) and α particles (right) emitted from ^{81}Rb (dots) and ^{80}Zr (hollow triangles) CN, normalized for the sake of comparison. From top to bottom, spectra of detectors centered at decreasing polar angles θ=60.0°, 47.0°, 34.85° measured with respect to the beam axis.

6.3 HECTOR

The energy calibration of the HECTOR detector has been done with several measurements at different energies in order to have a reliable calibration in a wide energy range (1-30 MeV). Before, during and after the experiment we have measured the γ emission from sources of ^{137}Cs and ^{60}Co and the internal radioactivity of BaF$_2$. The latter is due to small impurities of Ra (an alkaline earth as Ba) which α decay yielding 4 characteristic peaks, the higher-energy one at 3-4 MeV (Fig. 6.9). The shape, position and intensity of these peaks is a characteristic of each detector; therefore, the energy assignment has been done just before the experiment using the calibration obtained with the ^{137}Cs (E$_\gamma$= 662 keV) and ^{60}Co sources (E$_\gamma$= 1173 keV and 1332 keV).
At the end of the physics measurement, a calibration measurement has been performed with a beam of ^{11}B at E$_{lab}$=45 MeV delivered by the Tandem accelerator. The reaction was ^{11}B(D,γn)^{12}C. An absorber foil has been placed before the D target in order to reduce the energy of the impinging ^{11}B down to the value of E$_{lab}$=19 MeV allowing to populate a resonant state of ^{12}C. This state decays with a γ emission of 15.1 MeV. In this range of energy, the dominant mechanism of γ-ray interaction is pair production; therefore, two peaks corresponding to first and second escape of a γ ray of energy of 511 keV due to positron annihilation are present but not resolved in the spectrum. The peak is fitted with the sum of 3 Gaussian peaks (plus background), the centroid of the first escape peak being the fitting parameter (Fig. 6.10). This peak, together with the 4 peaks of internal radioactivity, has been used for the final calibration that has been done with the linear regression technique. The fitting procedure is based on standard fitting methods implemented in ROOT framework [73] and is explained in detail in the manual [76].

The calibrated γ energy spectrum has to be corrected for Doppler effect. Indeed the source velocity is non-relativistic, therefore we have applied the following formula:

$$E_{DC} = E\frac{1-\beta cos(\theta)}{\sqrt{1-\beta^2}} \tag{6.3}$$

where β=v_{rec}c and v_{rec} are taken as in Tab. 5.1. As for CsI, also for BaF$_2$ we are able to perform pulse-shape analysis in order to discriminate the signals of light charged particles from the ones of neutrons and γ-rays. In the data sorting procedure we have excluded the events falling in the triangle drawn in Fig. 6.11 corresponding to protons and α's. Neutrons interact in BaF$_2$ mainly through (n,γ) reactions. Therefore, their signals are difficult to disentangle in the fast vs slow matrix from the ones associated with γ detection. For them a clean discrimination can be achieved only via ToF, relying on the difference in ToF of γ rays and neutrons ($\geq$4 ns, as can be seen in Fig. 6.12, where the prompt γ peak is centered at ToF=1 ns) and the good time resolution of BaF$_2$ scintillators. In order to reduce random coincidences and neutron contamination, the events considered in the analysis are the ones falling in the graphical cut drawn in Fig. 6.13.

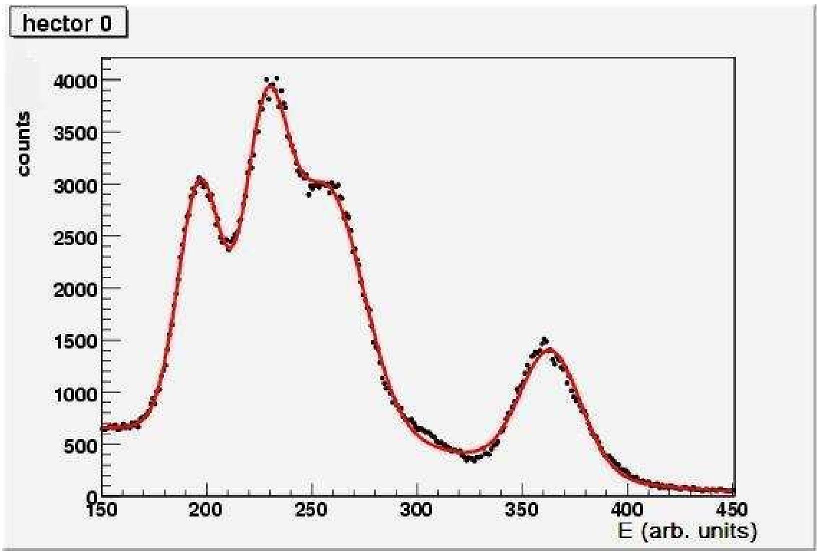

Figure 6.9: Energy spectrum of internal radioactivity of one HECTOR scintillator. The red line is the fit performed with the sum of three Gaussian functions, plus a single resolved Gaussian and a background.

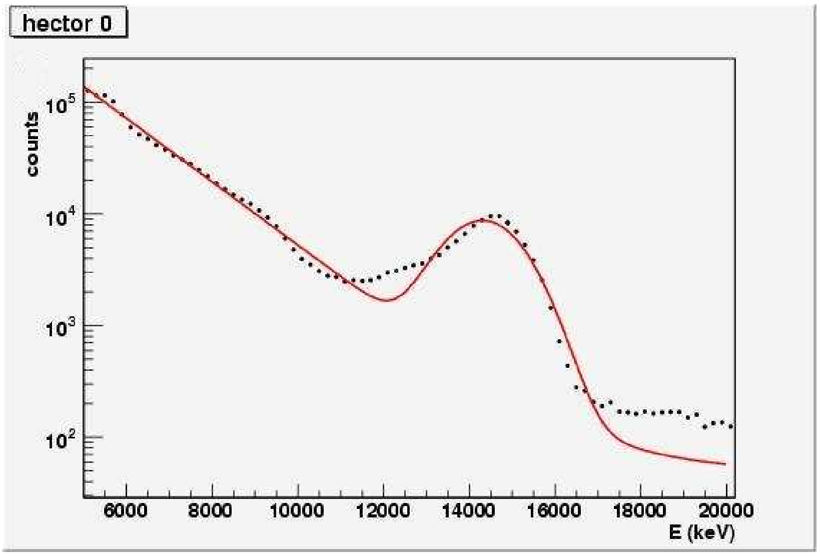

Figure 6.10: Energy spectrum of γ's emitted in ^{11}B(D,γn)^{12}C reaction detected by one HECTOR scintillator. The red line is the fit performed with the sum of three Gaussian functions plus a background.

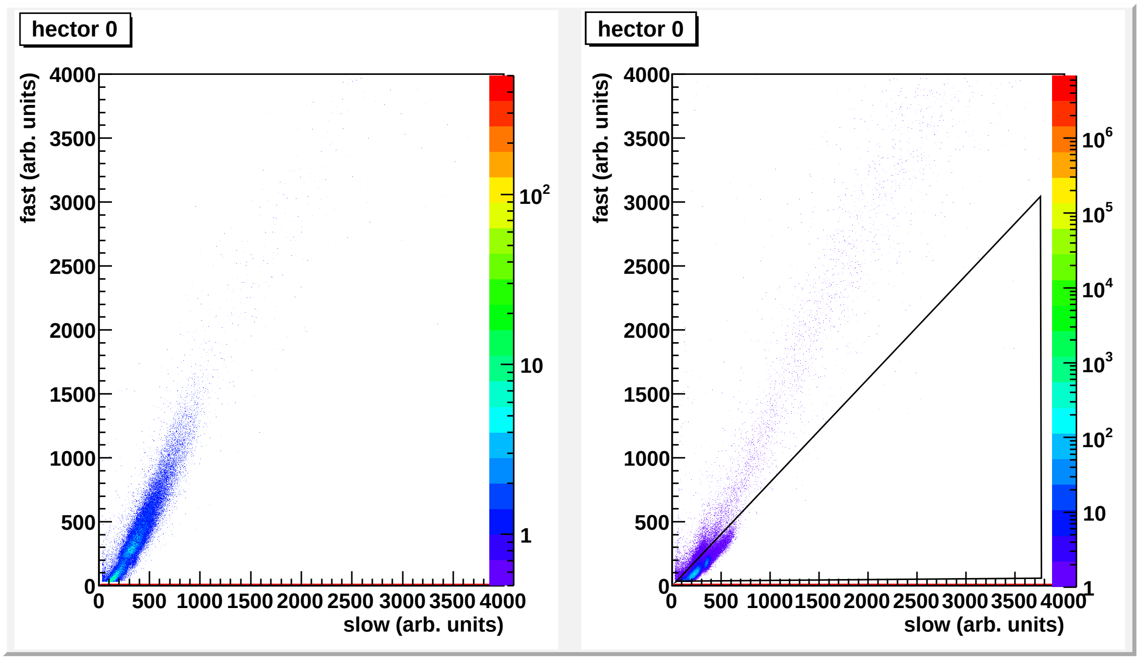

Figure 6.11: Fast vs slow correlation. The spectrum on the left is taken in beam and is dominated by the ridge corresponding to γ detection, extending to high energies. The one on the right is the sum of the previous one and a run of background, dominated by internal radioactivity, and is shown here in order to visualize more clearly the separation between charged and neutral particles. The signals falling inside the triangle drawn on the correlation matrix correspond to light charged particles and are rejected in the analysis of γ emission.

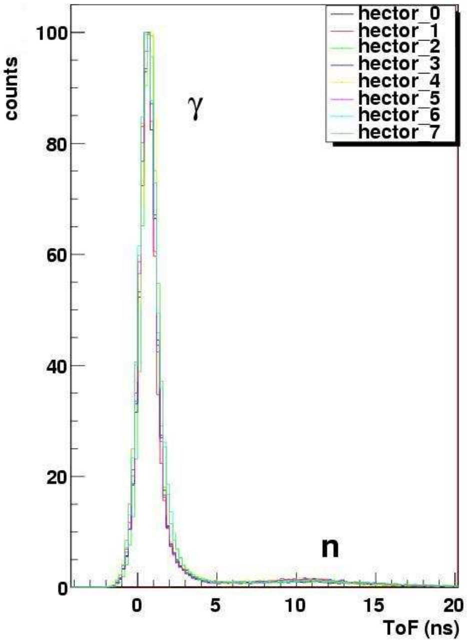

Figure 6.12: ToF spectrum of Cl+Ca reaction. The prompt γ peak has been centered at 1 ns, corresponding to the ToF of γ's in HECTOR (see Tab. 5.2), while the broad distribution on its right corresponds to neutrons evaporated in CN decay.

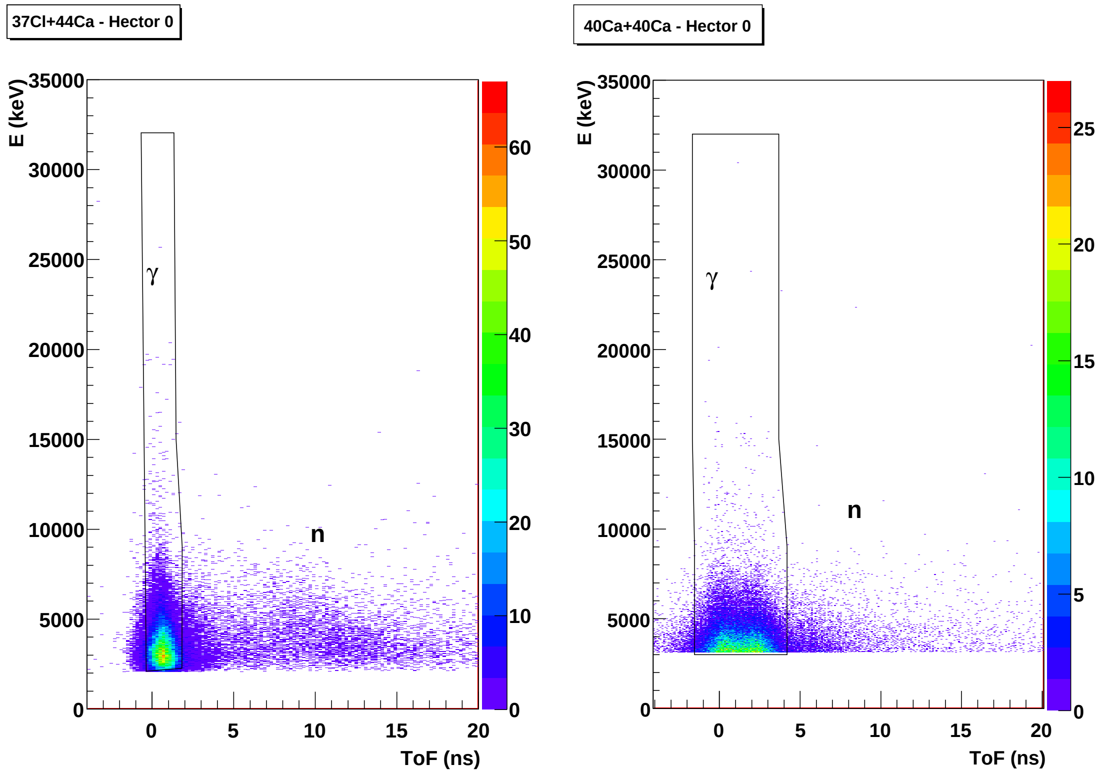

Figure 6.13: Energy vs ToF in one of the HECTOR detectors for Cl+Ca (left) and Ca+Ca (right) reactions. The splitting of the γ peak due to RF drift (see Sect. 6.5 for more explanations) can be seen in the right panel and induced us to enlarge the graphical selection. It can also be noted that, due to the fact that ^{80}Zr is a neutron-deficient nucleus, neutron emission is much suppressed and therefore the contamination of neutrons in the graphical cut is negligible.

Summarizing, the following conditions have been applied in the sorting of the collected data in order to select the γ spectra plotted in Fig. 6.14:

- conditions for the existence of good time signal from RF, HECTOR and PHOSWICH detectors (for each TDC)
- energy and ToF of γ's falling in the graphical cut in Fig. 6.13 (for each HECTOR detector); this corresponds to a gate on energy > 3 MeV and a window of ~ 2 ns of width on the prompt gamma peak, that we enlarge at higher energy where there is no risk of neutron contamination.
- fast and slow energy signals falling outside of the graphical cut of Fig. 6.11 (for each HECTOR detector)
- fold one of γ's fulfilling the previous condition (for the whole event)
- fold one of fusion-evaporation residues identified in the GA vs ToF correlation using the graphical cut in Fig. 6.2 (for the whole event).

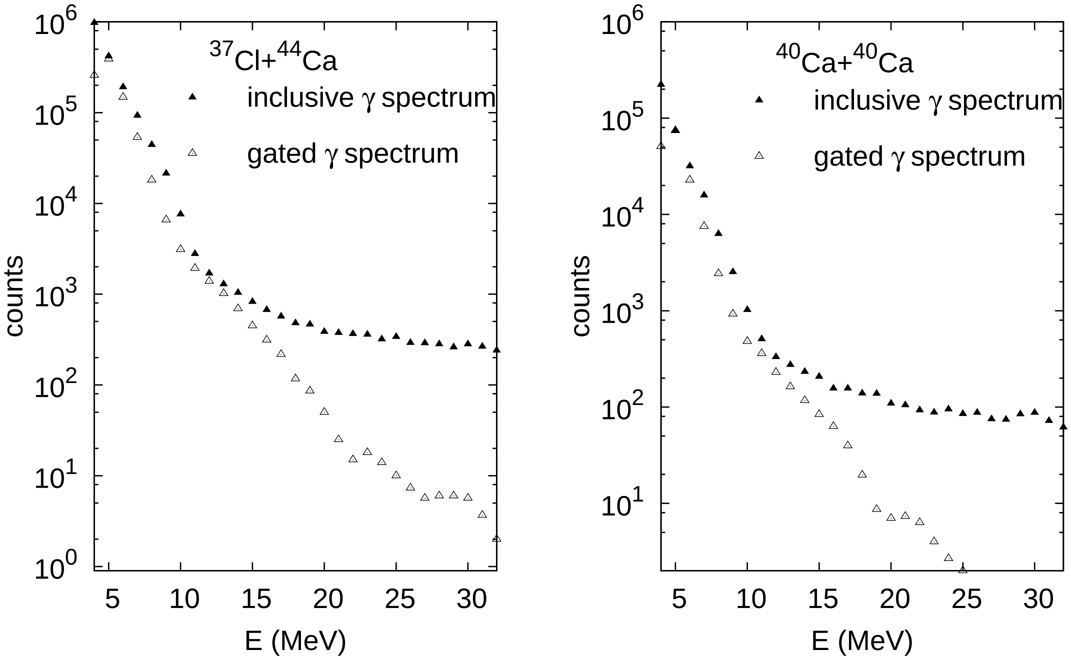

Figure 6.14: Inclusive γ-ray spectra (filled triangles) compared with the ones obtained with the gating conditions listed in this chapter. The inclusive spectra (open triangles) have been arbitrarily normalized to the gated ones for comparison. Cl+Ca spectra are shown on the left, whereas Ca+Ca spectra are shown on the right.

6.4 γ multiplicity

The multiplicity of measured γ rays can be calculated dividing the number of γ-residue coincidences by the number of residues detected in single mode in PHOSWICH detectors (trigger 2 in the list in Sect. 3.6), multiplied by the factor of reduction of this trigger. In order to calculate the multiplicity of γ emitted by the CN, the response function and efficiency of the HECTOR array has to be known with great accuracy. Unfortunately, we are able to simulate the response function (see Fig. 3.3 and text) but we cannot rely on the evaluation of the efficiency. Therefore, in order to obtain the absolute efficiency we have normalized the spectrum measured in the decay of ^{81}Rb on the γ-multiplicity spectrum calculated within the CASCADE code. The normalization has been done on the number of counts at 7 MeV, but is not dependent on the point of normalization since the measured spectrum is expected to be fully reproduced by standard Statistical Model (see Chapt. 7).

The same normalization factor, rescaled on the beam current monitored by means of the plastic scintillator (placed at θ=2°), is valid also for ^{80}Zr.

6.5 Details of data reduction

6.5.1 RF drift

As explained in Fig. 3.22, the reference to build all ToF spectra is the RF signal. This is the signal applied in order to split the beam in bunches of ~ 1 ns width equally spaced at intervals of 200 ns (or multiples according to the need). Therefore, a change in the synchronism between this signal (a square wave) and the bunch of beam delivered to the user (and, consequently, the arrival of the reaction products in the detector) may seriously compromise the quality of the ToF spectra. In this experiment we have observed three kinds of deviation from ideal RF behavior that have to be accounted for:

1. jumps of several tens of ns
2. continuous drift of ~ 2 ns during the measurement with ^{40}Ca beam, as shown in Fig. 6.15
3. development of a tail in the time spectrum of RF during the measurement with ^{37}Cl beam, inducing a tail on the right side of the ToF prompt γ peak of the extension of ~ 3 ns (see the left panel of Fig. 6.16)

While the first problem can be easily solved with a careful alignment of the time peak, the second and the third are more difficult since they cannot be corrected and appear as a worsening of the time resolution.

We have performed several tests to pin down RF as the source of these drifts. The clearest ones are the ones performed on a subset of the dataset corresponding to the events triggered only by the plastic scintillator; since this trigger signal comes from one and only one detector, detecting basically elastically scattered beam particles. Such a selection allows to have the peaks corresponding to the same reaction products (e.g. elastically scattered beam particles and γ's) at fixed position in the time spectrum.

In Fig. 6.15, the values of the ToF obtained from the plastic scintillator (Tof$_{plastic}$= time$_{plastic}$-time$_{RF}$, upper panel), referred to hereafter as Plastic ToF, and RF time (lower panel) are plotted against subsequent time slots of the data taking, each bin corresponding to 10^4 events. A correlation between the drift (of ~ 2 ns) in the position of Plastic ToF and RF time can be seen (indeed in opposite directions since RF time is subtracted to build Tof$_{plastic}$). If we sort plastic time spectrum selecting the events triggered only by the plastic itself, we obtain a nice peak whose position reflects only the delays in the electronic chain. Therefore, the drift in plastic ToF necessarily comes from RF.

The same considerations are also valid for the other detectors. The splitting of the peak is evident in the ToF spectra of the HECTOR detectors (Fig. 6.13, right panel) while in the PHOSWICH detectors it is beyond the intrinsic resolution of the detector and of the physics process.

The development of the tail on the left side of the RF peak occurred after an interruption in the delivery of the ^{37}Cl beam and can be seen in the left panel of Fig. 6.16. Again this change of shape is mirrored by all the ToF spectra but can be seen only in HECTOR and plastic spectra.

Since the fastest neutrons reach HECTOR scintillators ~ 4 ns after the γ rays, in both cases 2 and 3 the contamination from neutrons is fortunately negligible and the broadening of the RF peak does not affect significantly the quality of our event selection. This statement has been verified comparing γ spectra gated on the first and second peaks in HECTOR ToF (for ^{40}Ca+^{40}Ca reaction, see the right panel of Fig.6.16) and on the left and right side of the ToF peak (for ^{37}Cl+^{44}Ca reaction). In both cases the difference is within the statistical uncertainty.

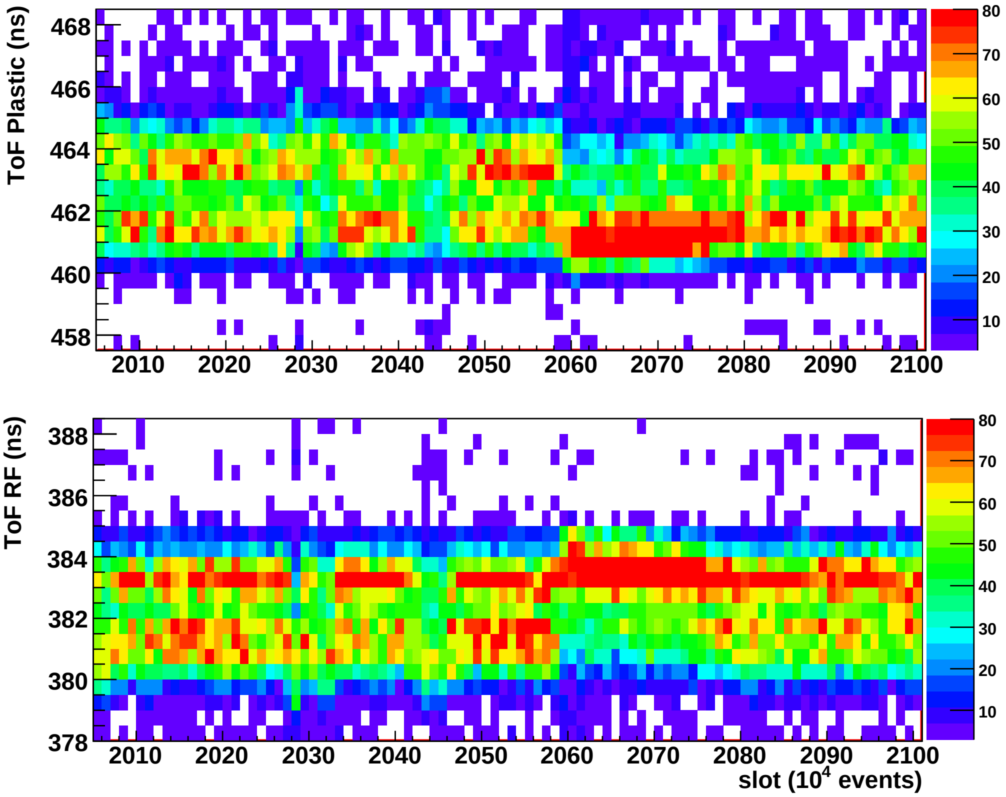

Figure 6.15: ToF vs time slot of the dataset corresponding to 10^4 events triggered exclusively by plastic. Upper panel: Plastic ToF on y-axis; Lower panel: RF time on y-axis.

Indeed this kind of problem may seriously affect the results of a measurement. Therefore, in the last measurement performed with GARFIELD-HECTOR apparatus, we have explored the possibility to use an alternative time reference, i.e. the BaF$_2$ scintillators from HELENA array. Results of this test are presented in Sect. 3.2.

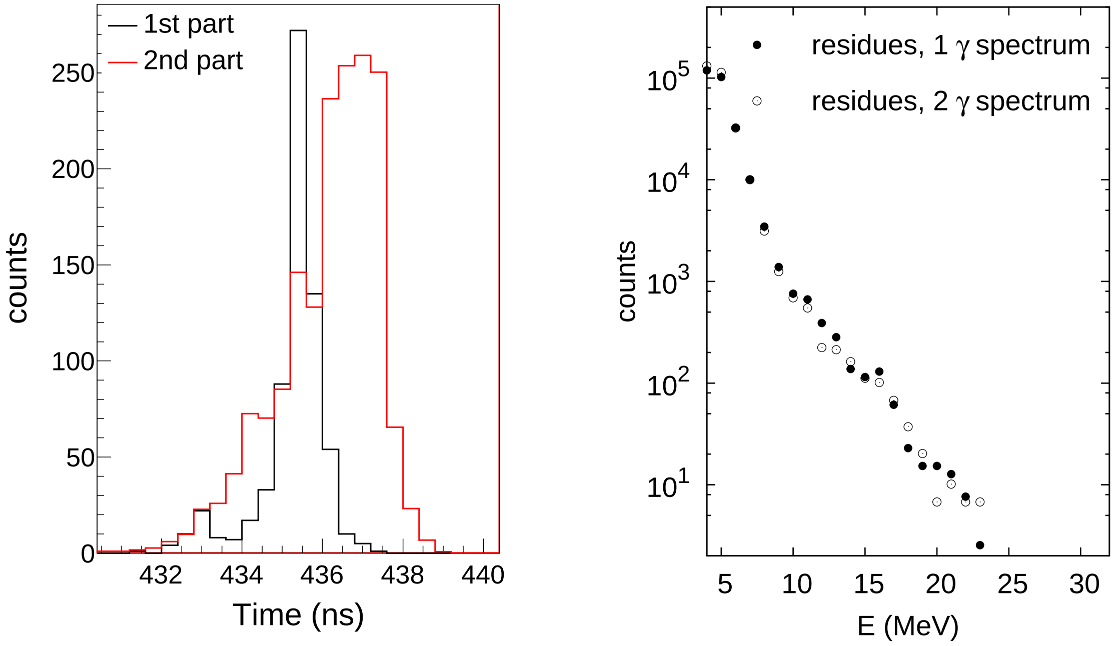

Figure 6.16: Left panel: RF time spectrum in the first and second parts of the measurement with ^{37}Cl beam. Right panel: γ spectrum gated on fusion-evaporation residues and the first or second prompt γ peak produced by the drift of RF during the measurement with ^{40}Ca beam (labeled as “residues, 1” and “residues, 2”, respectively).

6.5.2 ToF matching

As explained in Sect. 3.6, ToF spectrum for events validated by triggers involving GARFIELD signals are shifted backward of 200 ns since they take as a reference the subsequent RF signal (see Fig. 6.17). The effect is common to the ToF spectra from all detectors but particularly evident in PHOSWICH, as shown in Fig. 6.18.

In order to properly synchronize the ToF spectra and to set the coincidences between the different detectors, one has to find, for each event, the “first detectors to arrive”, i.e. the signal that has produced the validation for the trigger. This has to be done keeping in mind that only the signals above the threshold (or between lower and upper threshold in the case of PHOSWICH) can deliver a trigger signal to the acquisition. The threshold positions have been evaluated for each detector. All “first detector(s) to arrive” are linked to the same physical process and their signals have to be synchronized as far as ToF is concerned. Therefore, if needed a shift of 200 ns is added to the ToF in order to superimpose them on the same bunch. All the “second detectors to arrive” are rejected, since they are not synchronous with the physical process that has validated the acquisition of the event.

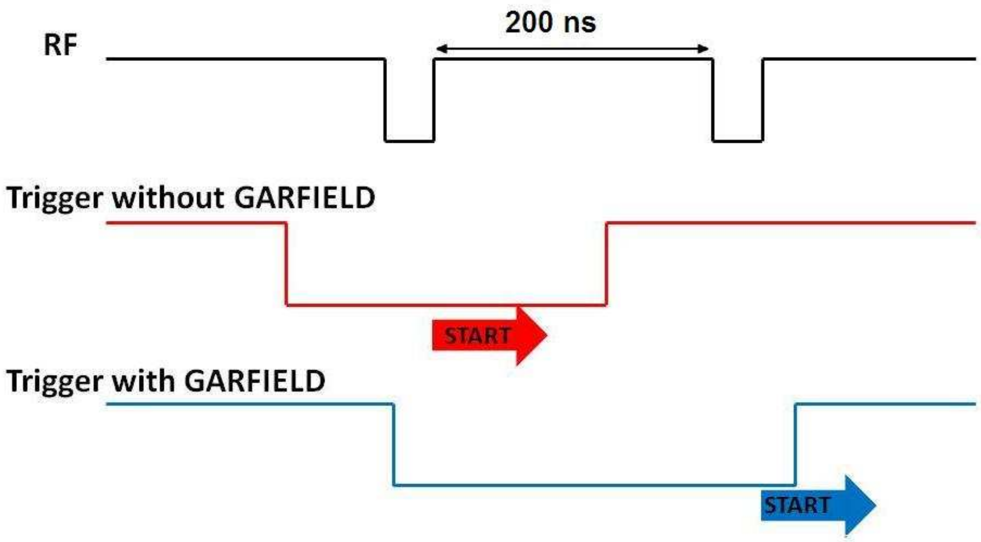

Figure 6.17: The start is given by the coincidence between RF and the trigger signal; a jittering in the trigger signal due to differences in signal processing and delays in the electronic chain of each detector induces a shift of 200 ns in the acquisition start for trigger signals involving GARFIELD detectors.

This procedure is applied when re-writing the dataset in a ROOT TTree structure. It simplifies the analysis but also avoids working with wrong coincidences. For example, before applying this procedure, events with $50 < \text{ToF} < 250$ in Fig. 6.18 can be either "first to arrive" with a non-GARFIELD trigger, or "second to arrive" (therefore spurious) with a GARFIELD trigger. A graphical cut on evaporation residues applied before the alignment procedure would have indeed included some spurious coincidences.

6.5.3 Scattered beam particles

As one can already see in Fig. 6.2, there are unidentified signals with GA intermediate between elastically scattered beam particles and evaporation residues, lying on the same hyperbole as the scattered beam. At these relatively low beam energies (4 and 5 MeV/nucleon) fusion is essentially the only reaction channel open (besides elastic scattering), therefore these signals can be only interpreted as produced by not well focused beam scattered on the target holder or similar.
The fact that the γ spectrum detected in coincidence with these signals (selected with the graphical cuts shown in the left panel of Fig. 6.19) is essentially a low energy spectrum (see the right panel of Fig. 6.19, where it is compared with the spectrum obtained in coincidence with evaporation residues) confirms this hypothesis.
Graphical cuts on evaporation residues (our physical selection) have been drawn paying special care to avoid contaminations in the cut. We have then compared the γ spectrum

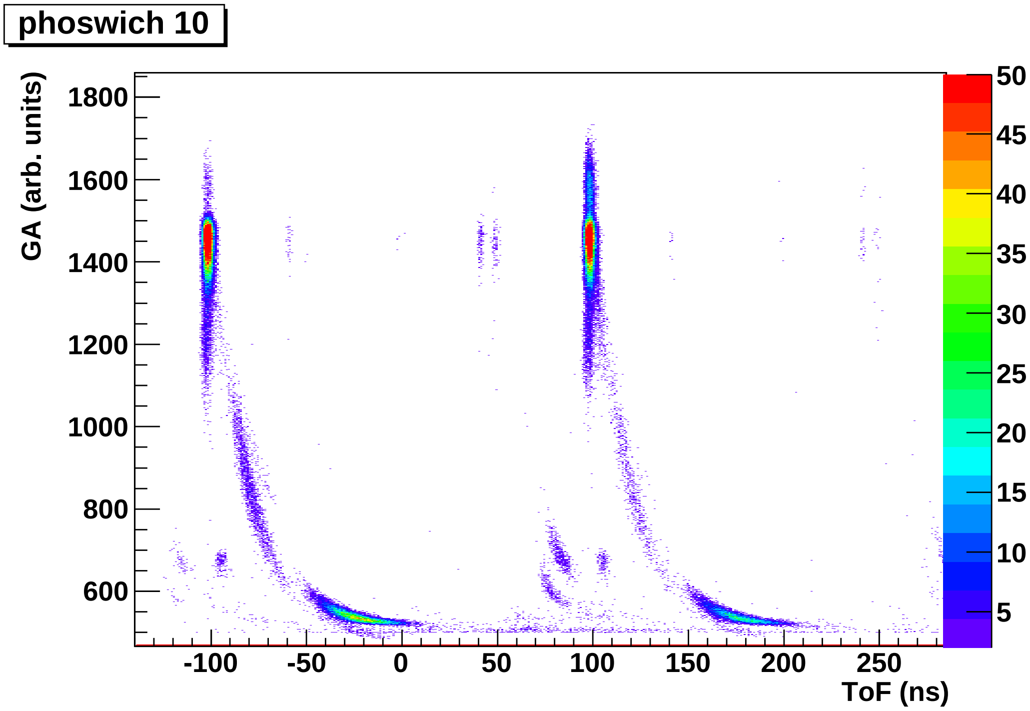

Figure 6.18: GA vs ToF two-dimensional spectrum of a PHOSWICH detector before time-of-flight matching. The shift of the reference RF signal induces a shift of 200 in the ToF. “First to arrive” signals validated by trigger OR.GARFIELD and OR.GARFIELD.AND.OR.PHOSWICH have -150 < ToF < 50, the ones validated by all the other triggers 50 < ToF < 250. In the time interval 50 < ToF < 250 there are also the “second to arrive” signals belonging to an event validated by the trigger OR.GARFIELD and OR.GARFIELD.AND.OR.PHOSWICH.

obtained in coincidence with one evaporation residue and nothing else in PHOSWICH detectors with the ones obtained dropping the last condition. Indeed the first condition is more exclusive since it discards all the events where, for example, a scattered-beam particle is detected by one PHOSWICH detector and an evaporation residue by another. However, the differences in shape between the spectra obtained with the two conditions are within the statistical uncertainty, therefore we have adopted the second condition yielding higher statistics.

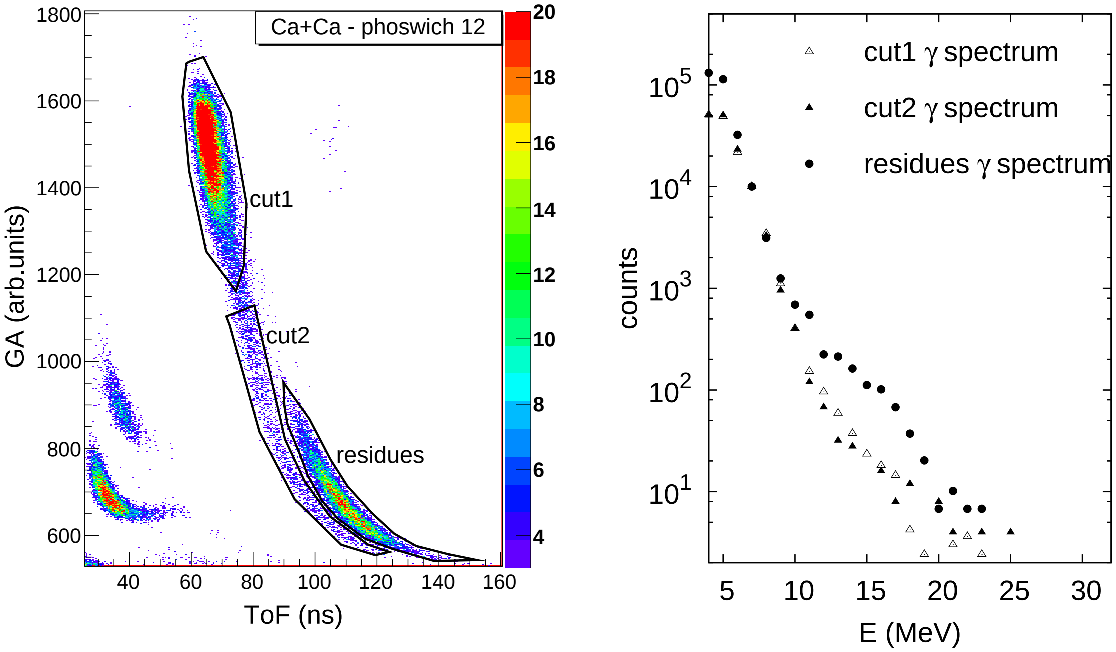

Figure 6.19: Left panel: The two regions of signals identified as scattered beam particles are enclosed by graphical cuts and labeled as *cut1* and *cut2*. Right panel: γ spectrum in coincidence with events falling in the three graphical cuts drawn in the left panel. The coincidence with *cut1* and *cut2* suppresses the high energy γ yield, confirming the interpretation of these signals as associated with reaction processes different from fusion-evaporation.

Chapter 7

^{80}Zr experiment: Statistical Model analysis

7.1 Statistical Model with isospin

The Statistical Model analysis has been performed using a Statistical Model code, where isospin is completely accounted for. In order to do that the original version of the CASCADE code [4] has been modified first by M.N. Harakeh [9] and later on by the Washington University group [10, 32] implementing the following features:

- population cross section matrices and level densities are labeled with the quantum number for isospin (in addition to excitation energy, angular momentum and parity)
- population cross section is isospin mixed before decay
- transmission coefficients are multiplied by isospin Clebsch-Gordan coefficients

Two classes of isospin are accounted for, $I_<$=I_z and $I_>$=I_z+1. The initial compound nucleus is usually populated in the state $I_<$=I_z. States with I > I_z correspond to configurations with a lower binding energy and, therefore, a higher excitation energy. The energy of the state $I_>$=I_z+1 in a nucleus of mass A is calculated as the energy of the state which is isobaric analog to the nucleus with the same A but Z_{analog}=Z-1 and N_{analog}=N+1 (or Z_{analog}=Z+1 and N_{analog}=N-1 if N<Z). The energy of the isobaric analog state is calculated with the formula in [77],

$$\Delta_{I_>,I_<}(A) = M(A_{analog}) - M(A) + \Delta E_c - (m_n - m_p) \tag{7.1}$$

where $m_{n,p}$ are the neutron and proton masses, respectively, ΔE_c is the Coulomb Displacement Energy (CDE) for a doublet of isobars with mass A and average charge $\bar{Z}$=min(Z,Z_{analog})+1/2, calculated with the formula in [77]:

$$\begin{aligned}\Delta E_c = \{&1539\frac{\bar{Z}}{A^{1/3}} - 3230\frac{\bar{Z}}{A} + 3600\frac{\bar{Z}}{A^{4/3}} - 783\frac{\bar{Z}^{1/3}}{A} + 530\frac{\bar{Z}^{1/3}}{A^2} \\ &-17\frac{\bar{Z}}{A^{2/3}}(\bar{Z} - \frac{A}{3 + 0.022484A^{2/3}}) + 60\}keV\end{aligned} \tag{7.2}$$

The CDE in Eq. 7.2 corresponds to the difference in Coulomb energy between the nuclei of the doublet, integrated over a Fermi density distribution. Formula 7.1 is given in [77] for analog nuclei with N⩾Z and has been extended in the code to nuclei with N<Z changing the sign of the last term as follows:

$$\Delta_{I_>,I_<}(A) = M(A_{analog}) - M(A) + \Delta E_c + (m_n - m_p) \tag{7.3}$$

For each excitation energy E*, angular momentum J and isospin I the level density is calculated with the usual formula:

$$\rho(E^*, J, I) = \frac{2J+1}{12\Theta^{3/2}(U+T)^2}\sqrt{a}e^{2\sqrt{aU}} \tag{7.4}$$

where Θ is the moment of inertia, T is the nuclear temperature, a the level-density parameter [70] and U=E*-Δ-J(J+1)/Θ=aT^2-T the internal energy for I=I$_<$, U=E*-Δ-J(J+1)/Θ-$\Delta_{I_>,I_<}$ for I=I$_>$. In this way $\rho(E^*, J, I_>) < \rho(E^*, J, I_<)$.
Using these level densities and the $\Gamma^{\downarrow}_{>}$ given in input to the code the mixing probability is calculated according to the parameterization of Harney, Richter and Weidenmüller described in Subsect. 2.3.1. As an example, the calculated and measured energies of the IAS are presented in Tab. 7.1 for several nuclei. Also the intermediate values used in the calculations are listed.

nucleus	M-M$_{analog}$	Δ E$_c$	m$_n$-m$_p$	$\Delta^{theo}_{I_>,I_<}$	$\Delta^{exp}_{I_>,I_<}$
^{60}Zn	-4.2	9.9	0.782	5.0	4.9 (Mazzocchi et al.)
^{80}Zr	-6.5	11.9	0.782	5.4	/
^{90}Zr	2.3	11.6	0.782	13.1	13.1 (von Neumann-Cosel et al.)
^{208}Bi	-3.7	18.8	0.782	15.2	15.1 (Bordewijk et al.)

Table 7.1: Mass difference between the isobar doublet, CDE, proton-neutron mass difference used to calculate the energy of the IAS $\Delta^{theo}_{I_>,I_<}$ with Eq. 7.1. The theoretical value is compared with the measured one, where available. All the values are in MeV.

7.1.1 Sensitivity to mixing after particle decay

In this analysis we have adopted the same $\Gamma^{\downarrow}$ for all the nuclei populated along the decay cascade. This hypothesis is supported by theoretical arguments (see Subsect. 2.3.1) but also by the fact that in this kind of analysis we are not really sensitive to the degree of mixing after the first step, due to the fact that the self-conjugate CN has I$_<$ $\neq$0 after one proton or one neutron emission. Of course along the decay cascade other self-conjugated nuclei are populated (in primis the one populated after one α emission from ^{80}Zr, which has a branching of only 8%), but their γ yield at high energy is much lower compared to the one of the initial CN. The effect of mixing for each nucleus populated along the decay is visualized in Fig. 7.1 as the difference in γ yield between a CASCADE calculation with and without isospin mixing.

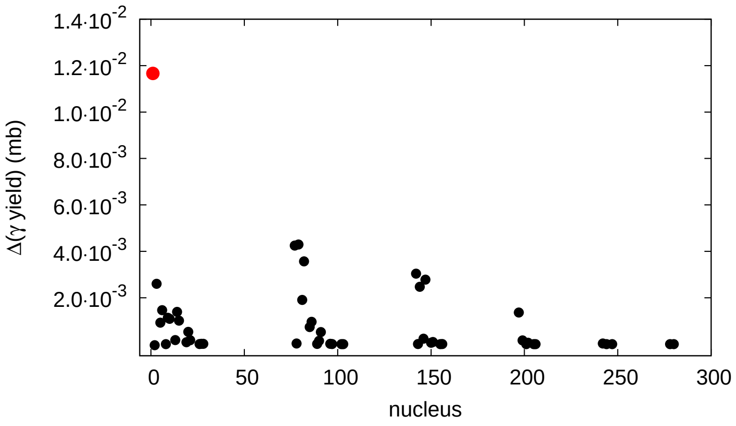

Figure 7.1: The difference in γ yield (in mb) between a CASCADE calculation performed with $\Gamma^{\downarrow}_{>}$=10 keV and with $\Gamma^{\downarrow}_{>}$=0 is plotted as a function of the number identifying each nucleus populated along the decay. The yield is the one obtained integrating between 10 and 32 MeV the γ-decay spectrum for each nucleus populated along the decay. The difference corresponding to the initial CN is plotted in red and is the dominant contribution. Along the decay cascade, the regions close to an N=Z nucleus are giving a relatively bigger contribution due to the effect of isospin mixing on γ decay and on branching ratio.

7.2 Analysis

The goal of this analysis is to extract the best fitting value of the Coulomb Spreading width $\Gamma^{\downarrow}_{>}$ (defined in Sect. 2.3) in order to evaluate the degree of mixing in ^{80}Zr at T $\sim$ 2 MeV. The recursive procedure to evaluate the degree of isospin mixing follows the steps listed below:

- Fit of GDR parameters (strength, width and centroid) on ^{81}Rb spectrum, with $\Gamma^{\downarrow}_{>}$=0
- Fit of Coulomb Spreading width $\Gamma^{\downarrow}_{>}$ on ^{80}Zr spectrum with best GDR parameters obtained at the previous step
- Reproduce the ^{81}Rb spectrum with the best fitting GDR parameters and $\Gamma^{\downarrow}_{>}$ obtained in the previous step in order to check the convergence of the procedure.

If the third step is not successful, the procedure is redone from the beginning fitting the GDR parameters on ^{81}Rb spectrum, with $\Gamma^{\downarrow}_{>}$ obtained in the second step. At each step, the best fitting parameters are the ones obtained with the χ^2 minimization technique. We have redefined the χ^2 as in Eq. 7.5 in order to enhance its sensitivity to the lower-yield region of the energy spectrum, the spectral shape of which furnishes information on the GDR built on the hot CN.

$$\chi^2 = \sum_{i=8MeV}^{i=14MeV} \frac{(Y_i - M_i)^2}{M_i^2} \tag{7.5}$$

where Y_i is the measured multiplicity per bin and M_i the multiplicity per bin from CASCADE Statistical Model Calculation.
We have verified that this approach is equivalent to performing the standard χ^2 minimization on the "divided spectrum", i.e. divided by an exponential spectrum obtained from the statistical decay of the same CN without GDR.
The statistical error is taken as one standard deviation of the Gaussian distribution (see Fig. 7.2) of the best fitting parameters extracted performing the χ^2 minimization on an ensemble of 10^5 spectra. These spectra have been obtained adding to the number of counts per bin (Y_i in Eq. 7.5) a fluctuation randomly extracted from a Gaussian distribution centered at zero and with a standard deviation equal to the statistical error on the number of counts per bin.

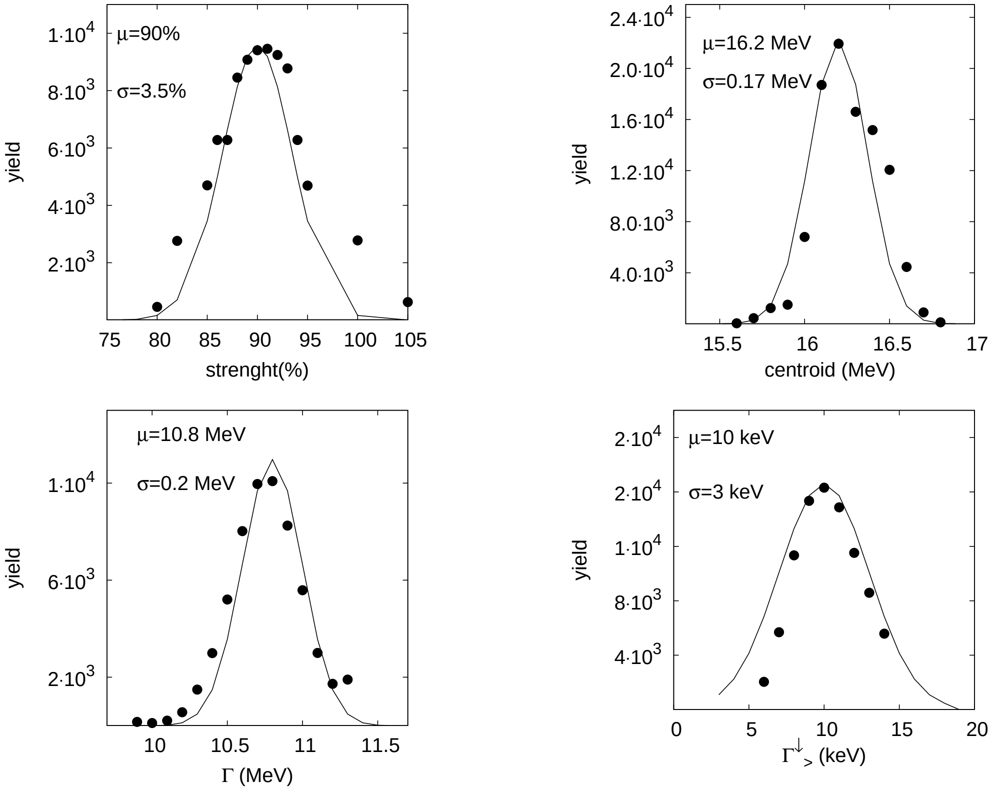

Figure 7.2: Distribution of parameters (from top left: GDR strength, centroid, width Γ and Coulomb spreading width $\Gamma^{\downarrow}_{>}$) obtained from χ^2 minimization as described in the text, together with the Gaussian fit (line). Centroid and standard deviation of the Gaussian are also shown and labeled as μ and σ.

7.2.1 Statistical analysis of ^{81}Rb

The parameters describing the GDR γ decay of hot ^{81}Rb as obtained from χ^2 minimization are listed in Tab. 7.2. The spectrum calculated with this set of parameters is plotted in Fig. 7.3.

CN	centroid(MeV)	Γ(MeV)	strength(%)	$\Gamma^{\downarrow}_{>}$(keV)
^{81}Rb	16.2±0.17	10.8±0.2	90±3.5	0

Table 7.2: GDR parameter giving the best fit of the measured γ-decay spectrum.

One can see that the best-fitting value of the width Γ is in good agreement with the one calculated according to the analytic formula of [57] and given in Tab. 5.6.

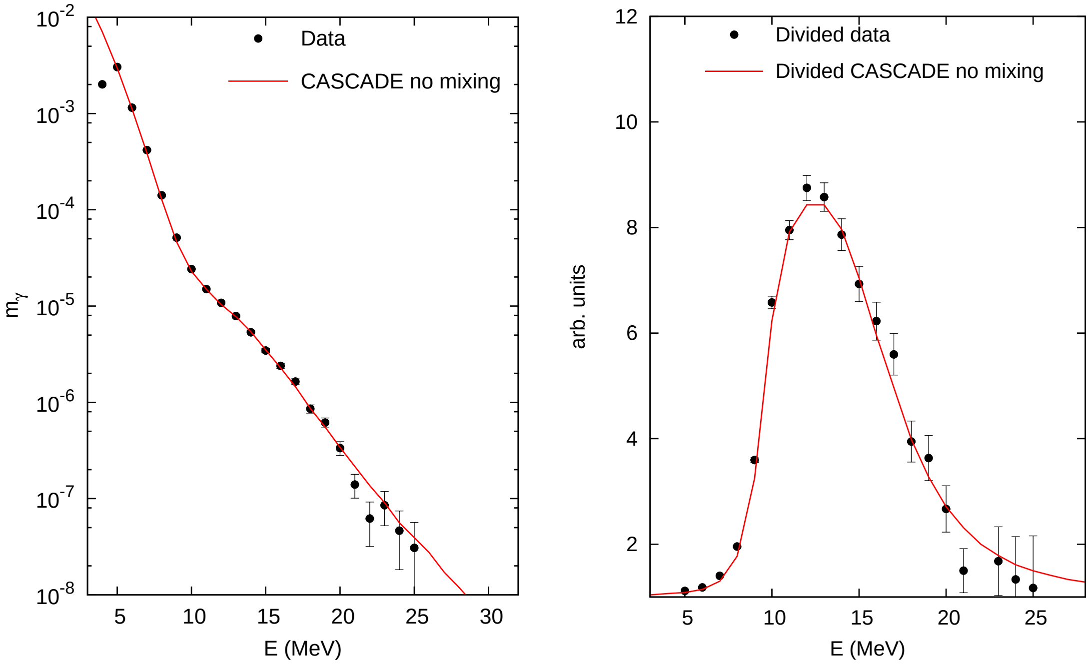

Figure 7.3: Left panel: measured γ-ray spectrum of ^{81}Rb compared with a Statistical Model calculation with GDR parameters obtained from χ^2 minimization. Right panel: the same, divided by an exponential spectrum obtained from the statistical decay of the same CN without GDR.

7.2.2 Statistical analysis of ^{80}Zr

The GDR parameters obtained from χ^2 minimization performed on the γ spectrum emitted by ^{81}Rb are listed in Tab. 7.3, together with the value of $\Gamma^{\downarrow}_{>}$ obtained from χ^2

minimization performed on the γ spectrum emitted by ^{80}Zr. The spectrum calculated with this set of parameters is plotted in Fig. 7.4 together with the spectra obtained with two extreme values of $\Gamma^{\downarrow}_{>}$. The Coulomb spreading width $\Gamma^{\downarrow}_{>}$ is physically equivalent to the spreading width of the IAS $\Gamma^{\downarrow}_{IAS}$. This datum has not been measured for ^{80}Zr but several measurements are available in this mass region. We find a good agreement between our best-fitting value of $\Gamma^{\downarrow}_{>}$=10±3 keV and the value $\Gamma^{\downarrow}_{IAS}$=9.9±0.6 keV measured by Kailas *et al.* [78] for ^{80}Se, which has the same mass as ^{80}Zr but I_0=6 and a smaller ground-state quadrupole deformation (β=0.23 [79]).

CN	centroid(MeV)	Γ(MeV)	strength(%)	$\Gamma^{\downarrow}_{>}$(keV)
^{80}Zr	16.2±0.17	10.8±0.2	90±3.5	10

Table 7.3: GDR parameters giving the best fit of the measured γ decay of ^{81}Rb and $\Gamma^{\downarrow}_{>}$ giving the best fit of the measured γ decay of ^{80}Zr.

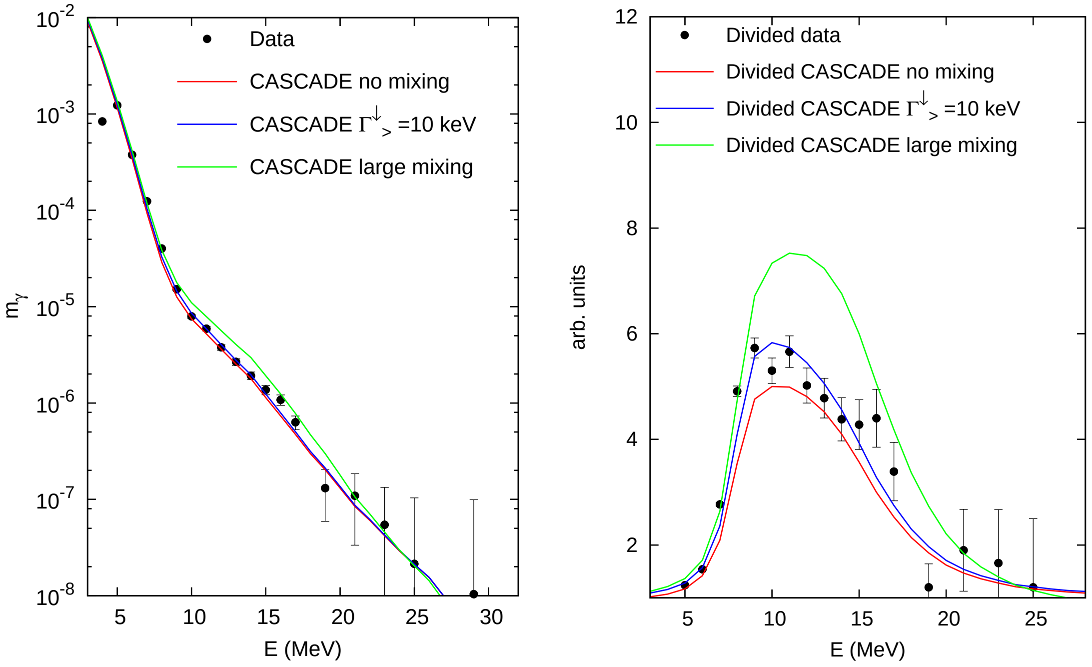

Figure 7.4: Left panel: measured γ-ray spectrum of ^{80}Zr compared with Statistical Model calculations without isospin mixing (red), with isospin mixing given by $\Gamma^{\downarrow}_{>}$ obtained from χ^2 minimization (blue) and with a large degree of isospin mixing (green). Right panel: the same, divided by an exponential spectrum to highlight the effect of isospin mixing.

7.2.3 Convergence of the fit

In order to check if further iterations are needed to reach the convergence of the fit, the spectrum displayed in Fig. 7.3 has been recalculated with the value of $\Gamma_>^\downarrow$ obtained for ^{80}Zr. As one can see in Fig. 7.5, this spectrum is not substantially different from the one of Fig. 7.3 and convergence is obtained at the first iteration. This is due to the fact that the γ decay of ^{81}Rb is not forbidden by the selection rules for E1 transitions and therefore it is not sensitive to isospin mixing.

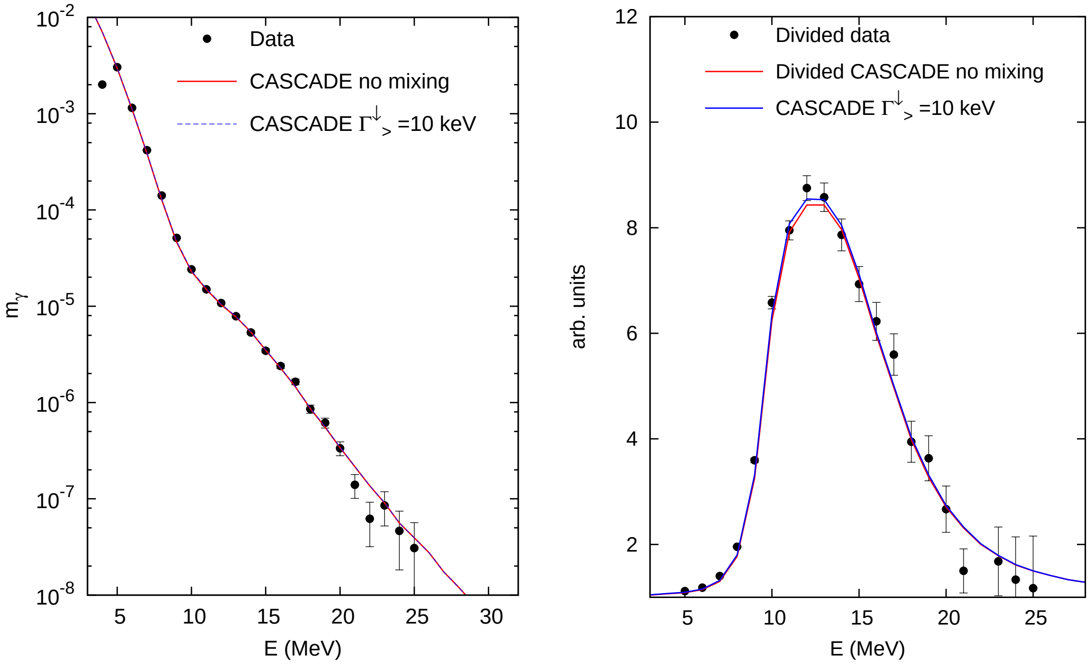

Figure 7.5: Left panel: measured γ-ray spectrum of ^{81}Rb compared with Statistical Model calculations without isospin mixing (red) and with isospin mixing given by $\Gamma_>^\downarrow$ obtained from ^{80}Zr analysis (blue). Right panel: the same, divided by an exponential spectrum.

7.2.4 Indirect proof in support of the need of isospin mixing

We have checked the possibility of reproducing the γ-decay spectrum of ^{80}Zr without allowing the mixing between states of different isospin, i.e. with $\Gamma_>^\downarrow$=0. This is possible only using a smaller GDR width, as shown Fig. 7.6 and listed in Tab. 7.4. Therefore, we have verified that the two spectra can be reproduced with the same GDR parameters (as expected) only allowing the mixing between states with $I_<$ and $I_>$.

CN	centroid(MeV)	Γ(MeV)	strength(%)	$\Gamma^{\downarrow}_{>}$(keV)
^{80}Zr	16.2±0.17	9.7±0.2	90±3.5	0

Table 7.4: GDR parameters giving the best fit of the measured γ decay of ^{80}Zr without introducing isospin mixing.

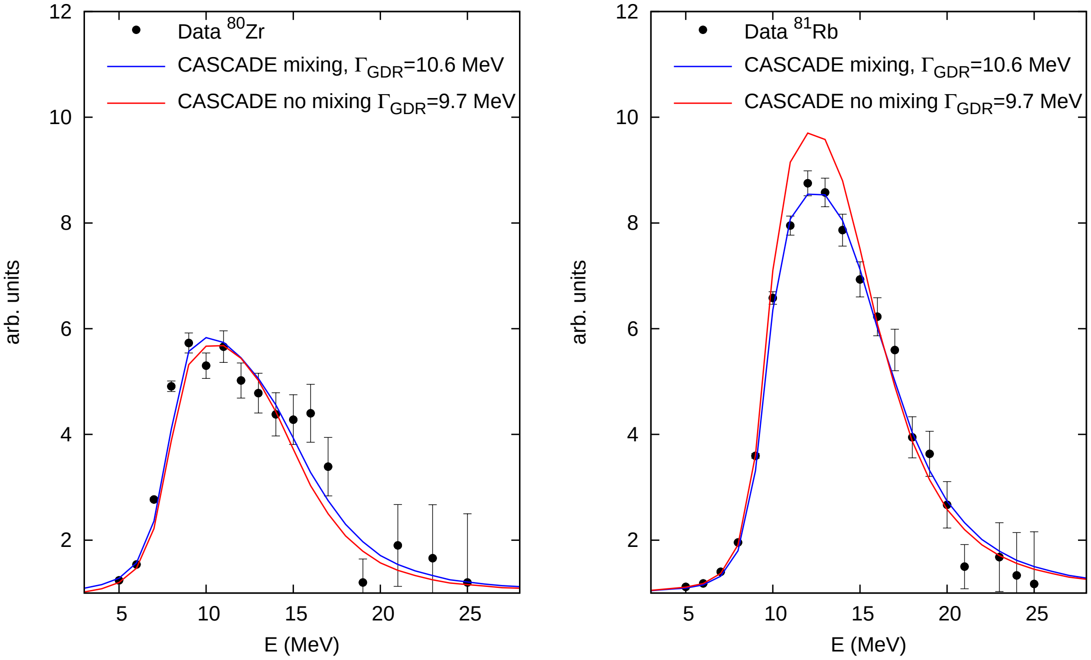

Figure 7.6: Left panel: measured γ-ray spectrum compared with Statistical Model calculations reproducing the γ decay of ^{80}Zr with $\Gamma^{\downarrow}$=0. Right panel: measured spectrum of ^{81}Rb compared with Statistical Model calculations obtained with the same set of GDR parameters used in the left panel. In both panels the spectra are divided by an exponential to highlight the effect of a change in GDR width.

7.3 Degree of isospin mixing

Within the Statistical Model and the formalism described in Subsect. 2.3.1, $\Gamma^{\downarrow}_{>}$ is kept fixed at all CN angular momenta J and decay steps. $\Gamma^{\downarrow}_{<}$(J) is obtained from $\Gamma^{\downarrow}_{>}$ via detailed balance and the isospin mixing parameters $\alpha^2_{>}$(J) ($\alpha^2_{<}$(J)) are calculated from the CN decay width and from $\Gamma^{\downarrow}_{>}$ ($\Gamma^{\downarrow}_{<}$). Therefore, a set of mixing parameters $\alpha^2_{>}$(J) and $\alpha^2_{<}$(J) is associated with the best fitting value of $\Gamma^{\downarrow}_{>}$, as is shown in Fig. 7.7. Each value of the CN angular momentum J corresponds to a different rotational energy (see Fig. 5.2) and to a different temperature T according to Eq. 5.2. In ^{40}Ca+^{40}Ca fusion-evaporation reaction at E_{beam}=200 MeV, a wide range of angular momenta up to J $\sim$

60 $\hbar$ is populated and temperatures up to 3 MeV are probed by the CN. Consequently, CASCADE calculations yield a significant variation of $\alpha^2_>$ and $\alpha^2_<$ with J as can be seen in Fig. 7.7. The steep increase of $\alpha^2_>$(J) and $\alpha^2_<$(J) with increasing J reflects the stronger effect of isospin-breaking interaction on colder and longer-lived CN.

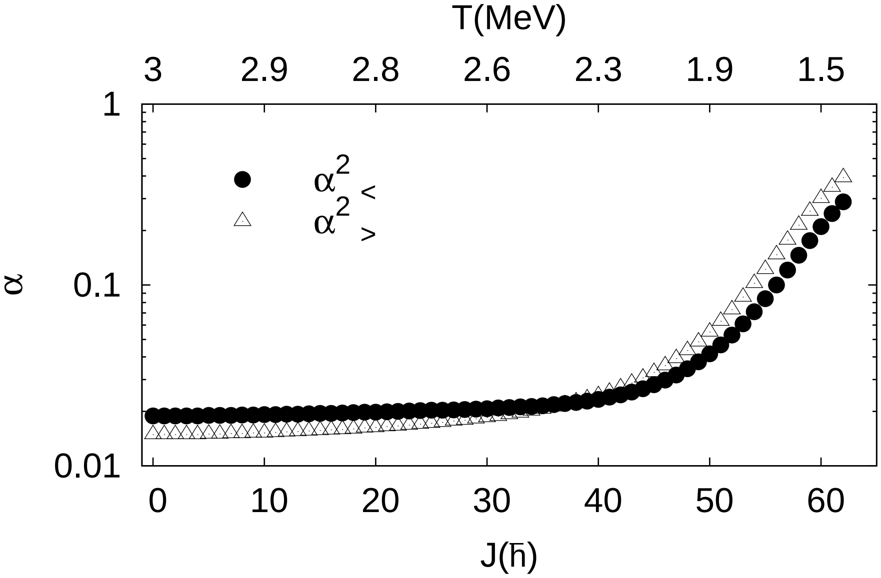

Figure 7.7: Mixing parameters $\alpha^2_<$(J) (filled dots) and $\alpha^2_>$(J) (hollow triangles) as a function of J (bottom axis) and T (top axis).

In literature, the degree of isospin mixing obtained from Statistical Model analysis of hot CN decay is given as the weighted average of $\alpha^2_<$(J). The weight is the γ yield for each J, obtained within a CASCADE calculation as the spin population of the initial CN multiplied by the γ branching ratio, i.e. the probability of γ emission divided by the summed probability of neutron, proton, α and γ emission.

In the previous analyses [45, 46] the γ branching ratio displayed a smooth dependence on J (see the case of ^{44}Ti at T$\sim$ 2.5 MeV in Fig. 7.8, right panel); therefore, the weight function is very similar to the spin population. This fact, combined with the milder dependence of $\alpha^2_<$ and $\alpha^2_>$ on J, yielded an average value of $\alpha^2_{<,>}$ substantially corresponding to $\alpha^2_{<,>}(<J>)$.

This is not the case for ^{80}Zr. In fact at high J the γ branching ratio strongly increases (see Fig. 7.8, left panel) due to the low level density of the final states reached by the particle decay.

The decrease of the level density of final states can be understood looking at the intrinsic energy of the CN as a function of J plotted in Fig. 7.9 together with the particle-separation energies of ^{80}Zr. As J increases, the internal energy approaches the particle separation energy and in the case of states $|>\rangle$=$|I_0+1, I_z\rangle$ goes below the neutron binding energy. Reisdorf level-density parameterization [43] adopted in our CASCADE calculation allows

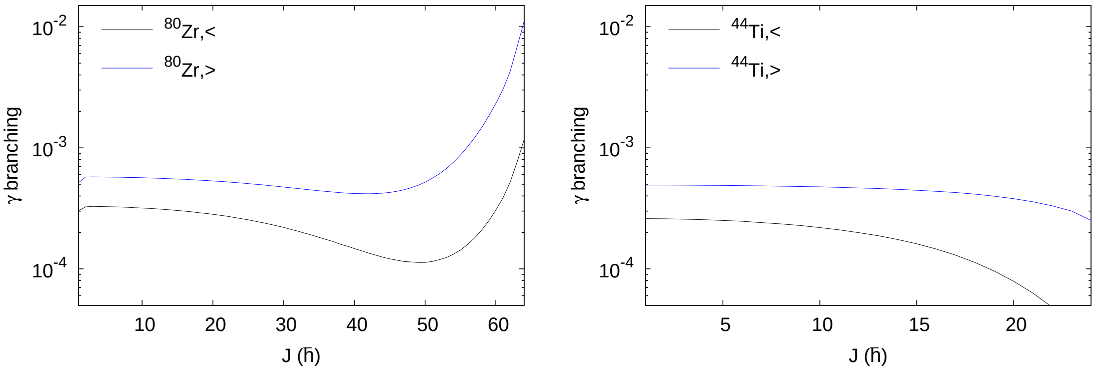

Figure 7.8: γ branching ratio calculated within CASCADE Statistical Model for the first decay step of ^{80}Zr (left panel) and ^{44}Ti (right panel).

to use the same energy-dependent parameterization in the whole range of temperatures and yields the expected decrease of the level density as the temperatures goes to zero [70].

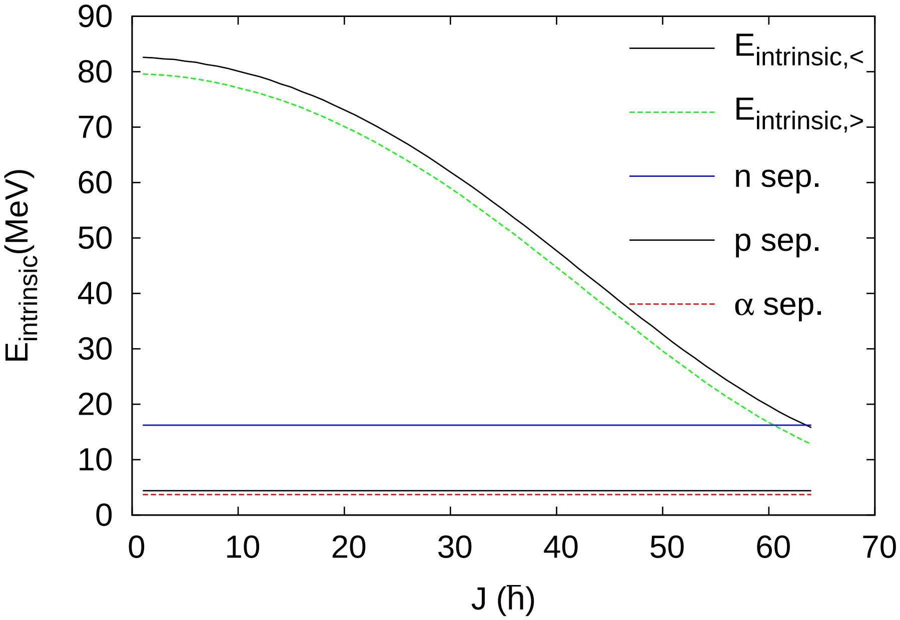

Figure 7.9: Internal energy obtained by subtracting from the initial excitation energy of the CN, E*=83 MeV, the rotational energy of the yrast line of ^{80}Zr (Fig. 5.2). Separation energies for neutron, proton and α's are plotted for comparison.

In order to be consistent with the approach used up to now, we have performed the average using as a weight the γ yield at each J. This procedure yields an average $\alpha^2_<$=0.05±0.01 for ^{80}Zr* CN at T∼2 MeV. A more detailed discussion on the interpretation of the results obtained from Statistical Model analysis will be done in Sect. 7.4.

7.3.1 Comparison with systematics at finite temperature

We compare in Fig. 7.10 our result with the existing systematics on isospin mixing. This comparison will be limited to the results obtained from measurements of GDR decay in self-conjugate nuclei which have been analyzed with the same approach of Sect. 2.3.1. For better clarity we divide the results in two groups, the first one including the results obtained by the Washington University group [10, 32], the second one by the Warsaw group [13, 45, 46]. The second group includes also the result obtained in this work. The lighter systems (A=26, 28) populated at higher temperature (T=3-4 MeV) belong to the first group while the heavier ones (A=32-80) populated at lower temperature (T=2-3 MeV) to the second one. We remark that each of the two groups contains systems with different Z and T. The results of the two groups are shown in Fig. 7.10 as function of Z (left) and T (right).

Within the first group it is not possible to recognize a clear trend in Z and T dependence.

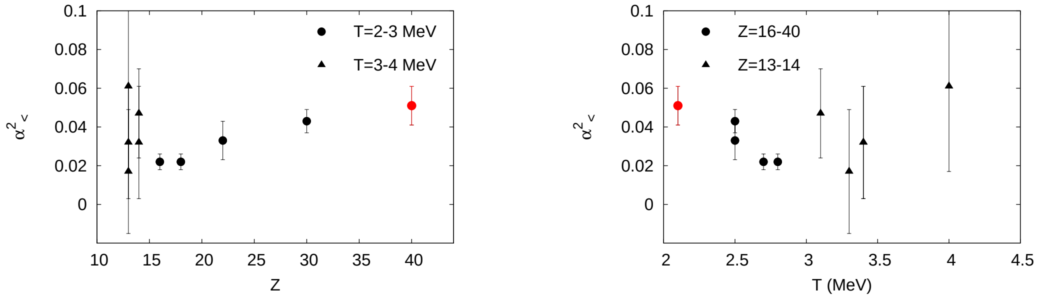

Figure 7.10: Systematics of $\alpha^2_<$ measured via GDR decay of the hot CN with Z=13-14 and T=3-4 MeV (triangles) and with Z=16-40 and T=2-3 MeV (dots). The result obtained from the analysis described in this Thesis belongs to the second group and is plotted with a red dot. The left panel displays the dependence of $\alpha^2_<$ on atomic number Z, the right panel the dependence on nuclear temperature T.

Conversely, within the second group a decrease of the degree of mixing with increasing T and an increase with increasing Z can be observed. In order to make more stringent statements it is necessary to disentangle the two effects by performing new measurements where only Z or T are varied.

7.4 Comparison with calculations at zero temperatures

We have investigated the temperature dependence of the isospin-mixing parameter $\alpha^2_>$ (corresponding to $\alpha^2_{I_0+1}$ in the ground-state notation) with the approach developed in [12] and already described in Subsect. 2.2.2.
We have applied Eq. 2.12 to ^{80}Zr neglecting the smooth temperature dependence of $\Gamma^{\downarrow}_{IAS}$ and of Γ_{IVM} and using the temperature-dependent CN decay width $\Gamma^{\uparrow}_{CN}$ given by CASCADE code (see Fig. 7.11). Since the extrapolation done in Ref. [12] does not take into account the angular momentum that is developed in fusion-evaporation reactions, we have decided for the sake of comparison to select the subset of CN with the smallest possible angular momentum, i.e. J=1 $\hbar$. Therefore, $\Gamma^{\uparrow}_{CN}$, nuclear temperature T and isospin mixing $\alpha^2_>$ used in this chapter are the ones assigned to CN with J=1 $\hbar$ within CASCADE calculations. In the case under study, T(J=1 $\hbar$)=2.9 MeV and $\alpha^2_>$(J=1 $\hbar$)=0.013, respectively.

$\Gamma^{\downarrow}_{IAS}$ and Γ_{IVM} have never been measured for the proton-rich ^{80}Zr and theoretical calculations are challenging due to the fact that its ground state has a high quadrupole deformation (β=0.4 [80]). Therefore, we have adopted as $\Gamma^{\downarrow}_{IAS}$ the value of the Coulomb spreading width $\Gamma^{\downarrow}_{>}$=10 keV obtained from our Statistical Model analysis. In fact, the two spreading widths are physically equivalent as already mentioned in Subsect. 7.2.2. The off-shell $\Gamma_{IVM}(E_{IAS})$ is predicted to be smaller than the physical one $\Gamma_{IVM}(E_{IVM})$, being proportional to the density of doorway states to which it can couple [40, 81]. This quan-

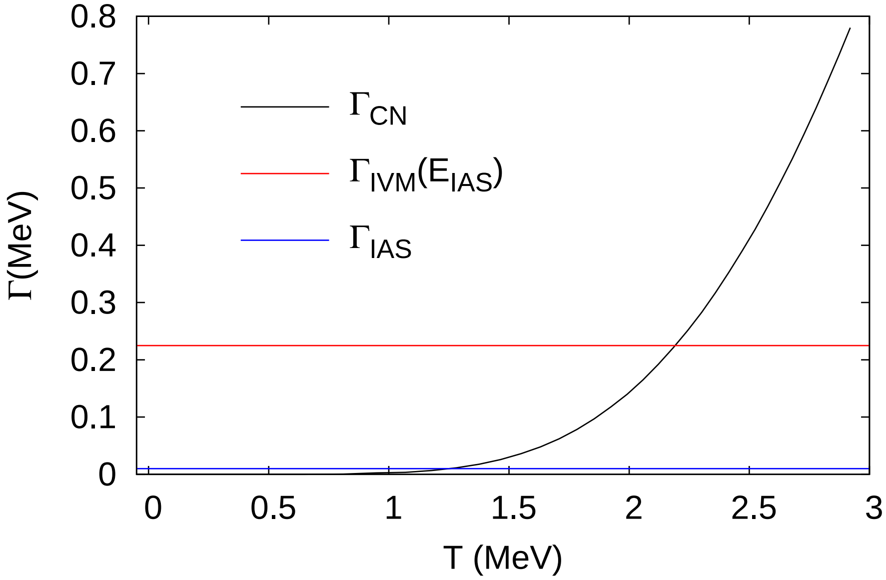

Figure 7.11: CN width Γ_{CN} of the state $| >\rangle$ calculated with CASCADE code. Calculations with CN excitation energies ranging from E*=1 MeV to E*=85 MeV have been performed in order to obtain the width as a function of temperature.

tity cannot be measured experimentally and theoretical calculations yield rather different results [81, 40, 38]. Therefore, we have decided to fix the value of $\Gamma_{IVM}(E_{IAS})$ in such a way as to reproduce the value of isospin mixing in the ground state of ^{80}Zr obtained with the most recent available calculation (see Tab. 2.1 and Ref. [37]). This implies a value of $\Gamma_{IVM}(E_{IAS})$=225 keV.

Neglecting the geometrical factor F(I_0), Eq. 2.12 becomes the following:

$$(\alpha^{I_0+1})^2 = \frac{\Gamma^{\downarrow}_{IAS}(E_{IAS})}{\Gamma^{\uparrow}_{CN}(T) + \Gamma_{IVM}(E_{IAS})} \tag{7.6}$$

and yields the trend displayed in Fig. 7.12.

One can see that, once $\Gamma_{IVM}(E_{IAS})$ is fixed in order to reproduce the value of α^2=0.045

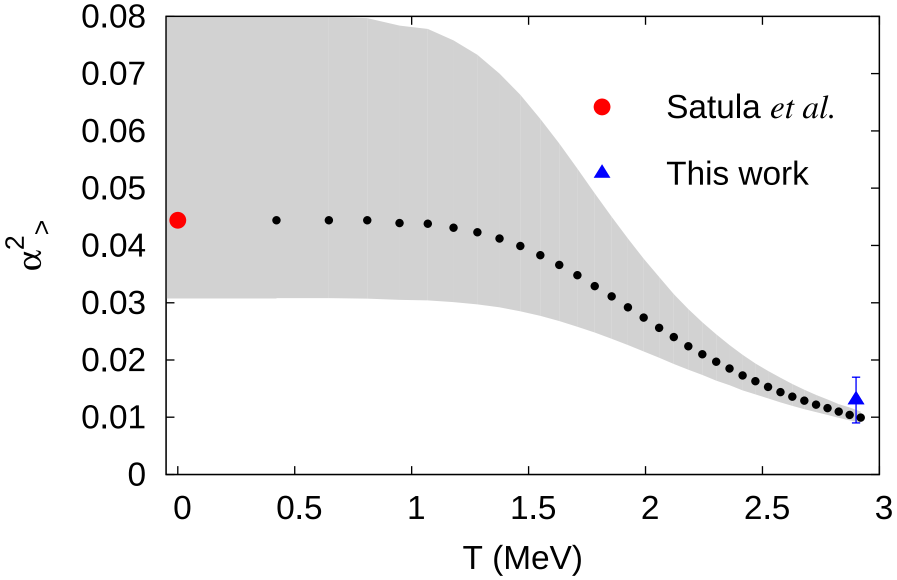

Figure 7.12: Temperature dependence of the isospin-mixing parameter $\alpha^2_>$ (equivalent to $(\alpha^{I_0+1})^2$) according to Eq. 7.6 with the choice of input parameters described in the text. The filled area is obtained by varying the parameter $\Gamma_{IVM}(E_{IAS})$ by ±100 keV with respect to the value 225 keV. The value of $\alpha^2_>$ at T=0 calculated in Ref. [37] is plotted with a red dot and the one obtained in this work with a blue triangle.

calculated in Ref. [37], also the value obtained from the analysis described in this Thesis ($\alpha^2_>$(J=1 $\hbar$)=0.013 at T(J=1 $\hbar$)=2.9 MeV) is quite well reproduced. The mixing probability decreases monotonically with increasing temperature without displaying the smooth increase from T=0 up to 1 MeV as predicted for ^{208}Pb in Ref. [12] (see Fig. 2.2). With the assumptions described above, this trend is clearly driven by the increase of CN decay width in agreement with Wilkinson hypothesis [31].

Conclusions

7.5 Dynamical Dipole measurement in ^{16}O+^{116}Sn fusion reaction

The results of the measurement of Dynamical Dipole γ emission in ^{16}O+^{116}Sn fusion reaction at the beam energies of 8.1, 12 and 15.6 MeV/u have been presented in Chapt. 4.

The analysis of the measured data and of the BNV simulations is still in a preliminary phase as far as the reaction at 12 MeV/u is concerned. At any rate, a "rise and fall" trend of the DD multiplicity as a function of beam energy is clearly seen with the measured data but not with the results of BNV simulations. This point calls for further investigations and for a more accurate evaluation of the fusion-evaporation cross section as a function of the impact parameter of the reaction.

Angular distribution of γ rays measured in the backward hemisphere (covered by HECTOR detectors) will be extracted and compared with the one obtained within BNV model. The analysis of light-charged-particle spectra detected in GARFIELD array is ongoing while the analysis of forward neutron emission measured by HELENA scintillators is still to come. We expect that the combination of the results of light-particle analysis might allow to pin down with more accuracy than in the past the amount of pre-equilibrium energy loss.

From the theoretical point of view, an approach that will allow to evaluate the fusion cross section within the same BNV simulation is under investigation. A recent study [28] displays a sensitivity of the time evolution of the quadrupole moment to the competition between fusion, fast fission and break-up. We are planning to apply this method also to the reaction ^{16}O+^{116}Sn at 12 MeV/u and to compare the results with the ones obtained with macroscopic fusion-probability evaluation codes (like PACE4) as already done with success in Ref. [28]. Further investigations will be necessary in order to pin down the fusion-evaporation contribution within the fusion reaction channel, especially at the more peripheral impact parameters.

Indeed an improved sensitivity to the equation of state via BNV (or equivalent) simulation of fusion dynamics is expected for systems with a higher N/Z asymmetry, as displayed by the results of BNV calculations performed with ^{132}Sn as projectile and quoted in Chapt. 1. A great improvement in this direction is expected once high-intensity exotic beams will become available.

7.6 Isospin mixing in ^{80}Zr

The Statistical Model analysis described in Chapt. 7 has allowed to extract the parameters describing the GDR built on ^{81}Rb* and ^{80}Zr* at T$\sim$2 MeV. Furthermore, the degree of isospin purity in the excited CN ^{80}Zr* has been evaluated from the hindrance of GDR γ decay. To our knowledge, ^{80}Zr is the system with the highest mass for which isospin mixing has been measured up to now.

If we restrict the comparison to the results obtained with the same approach and for systems with Z=16-40 at T=2-3 MeV, we find an increase of the degree of isospin mixing with increasing Z and a decrease with increasing T, as expected. The fact that both T and Z are different for each measurement does not allow to completely separate the two effects and calls for new measurements where only one parameter at time is changed.

The possibility to explore Z dependence is currently limited by the technical difficulties involved in the production of nuclei close to the proton dripline. Conversely, temperature dependence can be better evaluated with the existing techniques, either by measuring the γ decay of the same CN populated at different temperatures or by tagging on different decay cascades within the same CN decay.

This analysis has also allowed to evaluate the Coulomb spreading width $\Gamma^{\downarrow}_{>}$ of the state with isospin I=I$_0$+1. Differently from the degree of isospin mixing which depends on the lifetime of the system, this is an intrinsic property of the nucleus ^{80}Zr that can be compared with the spreading width of the IAS. This quantity has been measured for nuclei of mass$\sim$80 and a very good agreement is found between our result and the one obtained by Kailas *et al.* [78].

We have also extrapolated, making use of several assumptions, the value of the isospin-mixing parameter calculated in the ^{80}Zr ground state [37] up to the temperatures probed by the CN populated in the reaction under study and found a rather good agreement between the extrapolated value and the one obtained in our analysis.

The possibility to extrapolate the results obtained at finite temperatures down to zero temperatures is of great importance. In fact the wide range of isospin-mixing probability in the ground state spanned by available calculations (see Tab. 2.1) calls for a more systematic comparison with measured data both at zero and finite temperature.

Appendix A

Preparation and analysis of a BNV simulation

The following is the input file used to run the simulation of ^{16}O+^{116}Sn collision at projectile energy E_{beam}=12 MeV/u and impact parameter b=2 fm.

```
IBMIN....=  2
IBMAX....=  2
IDB......=  1
N1.......= 8
N2.......= 66
IZ1......= 8
IZ2......= 50
GR.......=1.444
GK.......=0.346
NGNUC....= 200
NYFL.....=  4
ZREL.....= 14.
ESURA....=  12.
TMAX.....= 400.
DT.......=  0.5
TFLOW....= 540.
DPFL.....= 50.
TFRAM....= 0.
TDEN.....= 0.
DTDEN....= 20.
tdmi.....= 0.
tdma.....= 200.
dtdmi....= 20.
ICT......= 2
IPRN.....= 20
```

```
ITFRAM...= 1
ICONT....=   0
IDP......= 200
isig.....=   1
ifull....=   1
icoul....=   1
isy......=   1
isect....=   0
isol.....=   2
ifram....=   0
iden.....=   0
```

The input parameters which have to be adjusted case by case are the following:

- IBMIN, IBMAX: minimum and maximum impact parameter (which have to be the same in this kind of simulations)
- N1, N2, Z1, Z2: number of neutrons and protons of projectile (1) and target (2), respectively
- NGNUC: number of test particles per nucleon, usually between 150 and 250
- ZREL: distance between projectile and target when the simulation is started
- ESURA: beam energy per nucleon, in MeV
- TMAX: time lapse of the simulation, in fm/c
- DT: time step of the simulation, in fm/c
- isy: parameterization of the symmetry term of the EOS:
  - 1 asy-stiff
  - 2 asy-soft
- isect: parameterization of nn cross section:
  - 0 Li and Machleidt parameterization [25, 26] of the in-medium cross section at the time-dependent local density calculated within the BNV simulation
  - 1 Li and Machleidt parameterization [25, 26] of free *nn* cross section
  - 2 Li and Machleidt parameterization [25, 26] at density 0.16 fm^{-3}
  - 3 Li and Machleidt parameterization [25, 26] at density 0.14 fm^{-3}; the cross section is set to zero for collisions with energy lower than 50 MeV in order to reduce spurious low-energy collisions
- isol: kind of process simulated:

  - 1 dipole oscillation built on a nucleus (to mimic GDR and check if its centroid energy is well reproduced). In this case another code (*prepanda.for*) is used in order to prepare the nucleus (i.e. nucleons coordinates in the phase space) to be given as input to the BNV code.
  - 2 collision

- iden: 1 to write the output file used to produce the density-contour plot

The same collision is usually simulated from 10 up to 100 times and the average of the output is performed in order to reduce the numerical fluctuations.
Bremsstrahlung spectrum is calculated from the output file with the *dpn* extension containing, for each time step, the value of the dipole moment calculated from the proton and neutron coordinates which are solutions of the Boltzmann-Langevin equation.
The analysis of the BNV output is performed with the code *med_dip_10events.for*. This code reads the set of files $*$.*dpn* produced by the BNV simulations, performs the average, the second derivative and the Fourier transform of the time-dependent dipole moment in order to calculate the Bremsstrahlung spectrum. Also, the angular distribution of the dipolar γ emission is calculated according to the procedure described in Sect. 1.3.
In addition to the parameters already given as input to the BNV simulation, input and output directories (`inputdir, outdir`), part of the input file name (`file`) and number of events to be averaged on (`nev`) have to be specified in the input file *med_tra.dat*. The input file of the code *med_dip_10events.for* corresponding to the one of the BNV simulation quoted above is the following:

```
N1.......=8
N2.......=66
IZ1......=8
IZ2......=50
itrs.....=1
TMAX.....=400.
deltat...=255.
step.....=20.
burto....=2.
en_inf...=4.
ix.......=1
inputdir.=/data1/dipolone09/analisi/dipolone/osn_12_a1_bnv_carmelo/
outdir...=/data1/dipolone09/analisi/dipolone/media_anna/
file.....=o16sn116_a1_b6_12_spectra
nev......=50
```

Appendix B

CASCADE Statistical Model

On the top of the original version developed by Pühlhofer [4], several versions of the CASCADE Statistical Model code have been developed. In this Thesis work, a version called DCASCADE [82] has been used in the analysis of γ decay from ^{132}Ce, while for the analysis of isospin mixing in CN we have used a version that we name CASCADE ISOMIX [9, 10, 32]. In the latter, isospin effects have been included in the standard Statistical Model formalism by enumerating the channels with an additional quantum number for isospin and by including the appropriate isospin physics in CN population and decay. The physics of isospin mixing is implemented as described in Subsect. 2.3.1 and Chapt. 7. Several input descriptions are available [82, 83]. Therefore in this Appendix we will focus on the most critical aspects of input preparation.

B.1 Input used for DCASCADE

The following is the input used for the preliminary DCASCADE calculation described in Subsect. 4.3.2.

```
132Ce
A         8        16        50       116
B         162.8
C         0         0         2         0
D        30         0         0        18        12        12
E         0         0         0         0         0         0         0
F         0       2.0       0.0       0.0       0.0       0.0
G         1         0         1
H         0      -1.0         0
I         0         0         0         0         0
L       0.0         0         0         0         0
M         2         0         4
N       0.0       0.0       0.0
O      -1.0       0.0       0.0       0.0       0.0       0.0       0.0
P       1.0      14.0      10.5       0.0       0.0       0.0
```

```
Q       0.0       0.0       0.0       0.0       0.0       0.0
R       0.0       0.0
S    .00001       0.0       .30       .04        .5       .05
T      32.0      32.0       0.0       0.0
U         1         1         1         1         1         0         0
V fort.2
Z 132Ce
```

The input parameters that typically have to be modified according to the system under study are listed here for each line (labeled with letters) and column (labeled with numbers):

- A1, A2, A3, A4: Z and A of projectile and target
- B1: beam energy, in MeV
- D1: maximum number of decay steps
- D4, D5, D6: maximum number of neutrons, protons and α's emitted
- F1, F2: maximum angular momentum and diffusivity of CN spin-population cross section. If F1 is zero, the maximum angular momentum is calculated internally
- F3: total fusion cross section. If F3 is zero, the total fusion cross section is calculated on the basis of the maximum angular momentum
- P1, P2, P3: strengh, centroid and width of the GDR

The beam energy 162.8 MeV (lower than the one used in the experiment) is adopted in order to populate the CN at lower excitation energy E^*_{CN}=129 MeV as expected due to the pre-equilibrium light charged particle emission.
The GDR parameters have been chosen as described in Sect. 4.3.
We remark that the input is read in a formatted way, therefore attention has to be paid in preserving formats and spacings.

B.2 Adapting CASCADE ISOSPIN to our physics case

B.2.1 Mass table

The masses of the nuclei populated in the decay cascade constitute a critical input of the Statistical Model since they are used to calculate the Q-values for the emission of α's, protons and neutrons. Furthermore, in CASCADE ISOMIX nuclear masses determine the energy and, therefore, the level density of the states $I_<$ and $I_>$. A new mass table has been compiled and adopted for this analysis (*mass2003.dat*) using the masses in the database [84]. This was especially necessary in the case ^{80}Zr, since the nuclei populated in its decay chain (and their isobaric neighbors) are close to the proton dripline where significant deviations from the liquid-drop mass formula are expected.

B.2.2 Input spin population

As mentioned in Chapt. 5, the kinematic selection due to the geometry of PHOSWICH detectors induces a bias in the phase-space population that can be accounted for using a modified spin population as the one presented in Fig. 5.4. This modified spin population has been calculated with a Monte-Carlo version of CASCADE code (see App. C) and given as input to the CASCADE ISOMIX code [1].

In order to read spin population from input, the value of JCN parameter in position C3 of the input file *cascade.input* has to be 999 and the spin population has to be detailed for each J value in lines F and following (see Subsect. B.2.3). The reading format of these lines has been slightly modified and the adopted one is FORMAT(2A,I3,F6.1). The input of spin population cross section is concluded with an E character.

In order to use this option adequately, we have found out that the angular momentum cutoff LCO has to be specified in position M4 in order to assign the value of maximum spin for yrast-line calculation. We have also commented the following lines in the part labeled as “compound nucleus population” since the input spin population from CASCADE Monte-Carlo is already divided by two in case of odd-mass nuclei. These lines should be uncommented if spin population is calculated internally.

```
      DO 56 J=1,II-1
c        IF(MOD(IACN,2).EQ.0) THEN
         JJ=J_TEMP(J)
c        ELSE
c          JJ=J_TEMP(J)/2
c        ENDIF
```

All these modifications are implemented in the version CASCADEISOMIX_999.for.

B.2.3 Input used for CASCADE ISOSPIN

The following are the input files of CASCADEISOMIX_999.for used in the calculation of ^{80}Zr and ^{81}Rb statistical decay, with modified spin population and isospin mixing included.

```
A   cl37+ca44 150mev
B   17,37,20,44,150.
C   3,0,-1,999,1,1,0,0.012,0.012
D   12,0,0,12,10,10
E   0,0,0,0,0,0,0,0.,0.,1.
F   +<  0  0.00
    +<  2  0.87
    +<  4  1.34
    +<  6  1.76
    +<  8  2.18
```

---

[1] In the Monte-Carlo CASCADE isospin effects are not taken into account. At any rate, these effects do not affect the reaction kinematics in a significant way.

```
+< 10  2.55
+< 12  3.13
+< 14  3.62
+< 16  4.08
+< 18  4.50
+< 20  4.90
+< 22  5.41
+< 24  5.90
+< 26  6.42
+< 28  6.89
+< 30  7.41
+< 32  7.98
+< 34  8.51
+< 36  9.14
+< 38  9.65
+< 40 10.38
+< 42 11.02
+< 44 11.58
+< 46 12.30
+< 48 13.28
+< 50 13.99
+< 52 14.90
+< 54 15.73
+< 56 16.86
+< 58 18.15
+< 60 19.18
+< 62 20.66
+< 64 22.09
+< 66 23.51
+< 68 25.20
+< 70 26.90
+< 72 29.00
+< 74 31.04
+< 76 33.17
+< 78 35.63
+< 80 37.69
+< 82 40.33
+< 84 41.82
+< 86 44.29
+< 88 45.49
+< 90 46.38
+< 92 46.58
+< 94 46.46
+< 96 44.61
```

```
    +< 98 41.65
    +<100 36.85
    +<102 31.35
    +<104 25.33
    +<106 19.51
    +<108 13.91
    +<110  9.56
    +<112  6.43
    +<114  4.20
    +<116  2.69
    +<118  1.67
    +<120  1.00
    +<122  0.60
    +<124  0.40
    +<126  0.22
    +<128  0.14
    E
G   0.85,0
H   -1,0.,0.,0.,0.,0,1
I   0.,0,0
J   -1.,0.,0.,0.,0.,0.,0.
K   0.9,16.2,10.6,0.,0.,0.
L   0.000001,0.000001,0.01,0.01,0.01,0.01
M   120,120,0,55,1.
N   3,3,3,1
O   -1,-1,-1,0


A   ca40+ca40 196mev
B   20,40,20,40,196.
C   0,0,2,999,1,1,0,0.012,0.012
D   12,0,0,12,10,10
E   0,0,0,0,0,0,0,0.,0.,1     .
F   +< 0  0.00
    +<  1  0.00
    +<  2  1.81
    +<  3  0.00
    +<  4  3.24
    +<  5  0.00
    +<  6  4.75
    +<  7  0.00
    +<  8  6.21
    +<  9  0.00
    +< 10  7.74
```

```
+< 11  0.00
+< 12  9.25
+< 13  0.00
+< 14 10.91
+< 15  0.00
+< 16 12.63
+< 17  0.00
+< 18 14.42
+< 19  0.00
+< 20 16.38
+< 21  0.00
+< 22 18.49
+< 23  0.00
+< 24 20.91
+< 25  0.00
+< 26 23.53
+< 27  0.00
+< 28 26.52
+< 29  0.00
+< 30 30.09
+< 31  0.00
+< 32 34.16
+< 33  0.00
+< 34 39.07
+< 35  0.00
+< 36 44.24
+< 37  0.00
+< 38 49.95
+< 39  0.00
+< 40 56.26
+< 41  0.00
+< 42 62.72
+< 43  0.00
+< 44 68.87
+< 45  0.00
+< 46 74.71
+< 47  0.00
+< 48 79.74
+< 49  0.00
+< 50 83.66
+< 51  0.00
+< 52 84.76
+< 53  0.00
+< 54 79.80
```

```
    +< 55  0.00
    +< 56 65.54
    +< 57  0.00
    +< 58 43.23
    +< 59  0.00
    +< 60 22.45
    +< 61  0.00
    +< 62  9.86
    +< 63  0.00
    +< 64  3.93
    E
G   0.85,0
H   -1,0.,0.,0.,0.,0,1
I   0.,0,0
L   -1.,0.,0.,0.,0.,0.,0.
M   0.9,16.2,10.6,0.,0.,0.
N   0.000001,0.000001,0.01,0.01,0.01,0.01
O   120,120,0,61,1.
P   3,3,3,1
Q   -1,-1,-1,0
```

The input parameters that typically have to be modified according to the system under study are listed here for each line (labeled with letters) and column (labeled with numbers). More details can be found in [83].

- B1, B2, B3, B4: Z and A of projectile and target
- B5: beam energy, in MeV
- C3: options for spin population cross section
    - -1 internally calculated
    - 999 spin population from input (see line F and following)
- D1: maximum number of decay steps
- D3, D4, D5: maximum number of neutrons, protons and α's emitted
- F: parity, isospin class, angular momentum and cross section, for each J populated by the CN. This part is concluded with the letter E
- H: level density parameterization; H1<0 sets Reisdorf parameterization, H1>0 is used to calculate a=A/H1 in the level density formula (see Eq. 7.4)
- K1, K2, K3: strength, centroid and width of GDR
- M4: when C3 is set equal to 999, M4 value plus twice the diffusivity yields the maximum angular momentum for which the yrast line is calculated

Appendix C

Kinematics within Cascade Monte-Carlo

CASCADE Statistical Model code is available also in a Monte-Carlo version.
In order to run the real CASCADE Monte-Carlo simulation (cascadmc.for), the decay path and the transmission coefficients at each step have to be calculated preliminarily with the codes KASKAD.FOR and TSUMATPF1_AM3L.FOR. The input files of the CASCADE simulation of ^{40}Ca+^{40}Ca and ^{37}Cl+^{44}Ca reactions follow:

```
A   119                         IRNA (default from sys$gettim)
B   mass2003.dat
C   zr80.tls
D   zr80_.out
E   zr80.evp
F   zr80_.prt
G   3L M cascade  --  200 MeV 40Ca + 40Ca
H   20,40,20,40,196.0  IZP,IAP,IZT,IAT,ELAB
I   0,0,2,-1,0,0,0,0,0 JP,JT,IP12,JCN,ITZT,INDPAR,INDIS,AMIX,BMIX
J   99,210,276,8,8,8 KOPTK,IPS1,IPSMAX,NNX,NPX,NAX
K   0,0,0,0,0,0,0,0,0.,1 IZE4,IAE4,JE4,IPE4,EXC4,IZFF,DAF,FFB
L   0.,2.,0. CL0,DIFF,SIGMCN
M   0,2             FTHETA,KOPTLD
N   -1,7.5,15.,7.5,15.,0,0   DALDM,UTR,ULDM,UJTR,UJLDM,KOPTLQ,KOPTEB
O   18.5,1.153,4,0,0,0 Reisdorf Coefficient eshell,r0reis,ipair,dareis,dalpha,dexpo
P   1.25,8.7e-6,2.6e-8 R0LDM,DEF,DEFS-def e def are no more used-use the file defdefs.dat
Q   -1,0,0,0.,0.,0,1.e-5             XYE1,XYM1,XYE2,CJG1,CJG2,XYENH,GMIN
R   0.8,16.0,9.0,0.,0.0,0.0,0.0,0.0,0.0  F1,E1,G1, F2,E2,G2, F3,E3,G3
S   0,0,0,0,0,0    ieop,igop,ifop,fde,fdf
T   0.000001,0.000001,0.3,0.04,0.5,0.05  WGR,CGR,CVCBE,CVCB,VK,CVK
U   32,32,50,64.,1.          EXR0,EXH,CJC,LCO,ESTEP
V   60,60,80,1,3,3          KOUTW,KOUTL,KEVAP,KGAMMA,prio,iang
W   1000000000,30,31,2,0,0,0,0,0,0,0    N,JSTP,K0,IG,kp,br,thck,q2d,q2f,q2w,elfact
```

```
X   2 3 52 0 4 5 53 0 5 6 54 0 7 8 55 0 8 9 56 0
    9 10 57 0 11 12 58 0 12 13 59 0 13 14 60 0 14 15 61 0
    16 17 62 0 17 18 63 0 18 19 64 0 19 20 65 0 20 21 66 0
    22 23 67 0 23 24 68 0 24 25 69 0 25 26 70 0 26 27 71 0
    27 28 72 0 29 30 73 0 30 31 74 0 31 32 75 0 32 33 76 0
    33 34 77 0 34 35 78 0 35 36 79 0 211 37 80 0 37 38 81 0
    38 39 82 0 39 40 83 0 40 41 84 0 41 42 85 0 42 43 86 0
    43 212 87 0 44 45 88 0 45 46 89 0 46 47 90 0 47 48 91 0
    48 49 92 0 49 50 93 0 50 51 94 0 213 214 224 0 214 215 225 0
    215 216 226 0 216 217 227 0 217 218 228 0 218 219 229 0 219 220 230 0
    220 221 231 0 53 54 95 0 55 56 96 0 56 57 97 0 58 59 98 0
    59 60 99 0 60 61 100 0 62 63 101 0 63 64 102 0 64 65 103 0
    65 66 104 0 67 68 105 0 68 69 106 0 69 70 107 0 70 71 108 0
    71 72 109 0 73 74 110 0 74 75 111 0 75 76 112 0 76 77 113 0
    77 78 114 0 78 79 115 0 80 81 116 0 81 82 117 0 82 83 118 0
    83 84 119 0 84 85 120 0 85 86 121 0 86 87 122 0 222 88 123 0
    88 89 124 0 89 90 125 0 90 91 126 0 91 92 127 0 92 93 128 0
    93 94 129 0 94 223 130 0 224 225 233 0 225 226 234 0 226 227 235 0
    227 228 236 0 228 229 237 0 229 230 238 0 230 231 239 0 96 97 131 0
    98 99 132 0 99 100 133 0 101 102 134 0 102 103 135 0 103 104 136 0
    105 106 137 0 106 107 138 0 107 108 139 0 108 109 140 0 110 111 141 0
    111 112 142 0 112 113 143 0 113 114 144 0 114 115 145 0 116 117 146 0
    117 118 147 0 118 119 148 0 119 120 149 0 120 121 150 0 121 122 151 0
    123 124 152 0 124 125 153 0 125 126 154 0 126 127 155 0 127 128 156 0
    128 129 157 0 129 130 158 0 232 233 241 0 233 234 242 0 234 235 243 0
    235 236 244 0 236 237 245 0 237 238 246 0 238 239 247 0 239 240 248 0
    132 133 159 0 134 135 160 0 135 136 161 0 137 138 162 0 138 139 163 0
    139 140 164 0 141 142 165 0 142 143 166 0 143 144 167 0 144 145 168 0
    146 147 169 0 147 148 170 0 148 149 171 0 149 150 172 0 150 151 173 0
    152 153 174 0 153 154 175 0 154 155 176 0 155 156 177 0 156 157 178 0
    157 158 179 0 241 242 249 0 242 243 250 0 243 244 251 0 244 245 252 0
    245 246 253 0 246 247 254 0 247 248 255 0 160 161 180 0 162 163 181 0
    163 164 182 0 165 166 183 0 166 167 184 0 167 168 185 0 169 170 186 0
    170 171 187 0 171 172 188 0 172 173 189 0 174 175 190 0 175 176 191 0
    176 177 192 0 177 178 193 0 178 179 194 0 249 250 256 0 250 251 257 0
    251 252 258 0 252 253 259 0 253 254 260 0 254 255 261 0 181 182 195 0
    183 184 196 0 184 185 197 0 186 187 198 0 187 188 199 0 188 189 200 0
    190 191 201 0 191 192 202 0 192 193 203 0 193 194 204 0 256 257 262 0
    257 258 263 0 258 259 264 0 259 260 265 0 260 261 266 0 196 197 205 0
    198 199 206 0 199 200 207 0 201 202 208 0 202 203 209 0 203 204 210 0
    262 263 267 0 263 264 268 0 264 265 269 0 265 266 270 0 206 207 271 0
    208 209 272 0 209 210 273 0 267 268 274 0 268 269 275 0 269 270 276 0
    0 0 0 0 0 0 0 0 0 0 0 0 0 0 0 0 0 0 0 0
    0 0 0 0 0 0 0 0 0 0 0 0 0 0 0 0 0 0 0 0
```

```
    0 0 0 0 0 0 0 0 0 0 0 0 0 0 0 0 0 0 0 0
    0 0 0 0 0 0 0 0 0 0 0 0 0 0 0 0 0 0 0 0
    0 0 0 0 0 0 0 0 0 0 0 0 0 0 0 0 0 0 0 0
    0 0 0 0 0 0 0 0 0 0 0 0 0 0 0 0 0 0 0 0
    0 0 0 0 0 0 0 0 0 0 0 0 0 0 0 0 0 0 0 0
    0 0 0 0 0 0 0 0 0 0 0 0 0 0 0 0 0 0 0 0
    0 0 0 0 0 0 0 0 0 0 0 0 0 0 0 0 0 0 0 0
    0 0 0 0 0 0 0 0 0 0 0 0 0 0 0 0 0 0 0 0
    0 0 0 0 0 0 0 0 0 0 0 0 0 0 0 0 0 0 0 0
    0 0 0 0 0 0 0 0 0 0 0 0 0 0 0 0 0 0 0 0
    0 0 0 0 0 0 0 0 0 0 0 0 0 0 0 0 0 0 0 0
    0 0 0 0 0 0 0 0 0 0 0 0 0 0 0 0 0 0 0 0
    0 0 0 0 0 0 0 0 0 0 0 0 0 0 0 0 0 0 0 0
    0 0 0 0 0 0 0 0 0 0 0 0 0 0 0 0 0 0 0 0
    0 0 0 0 0 0 0 0 0 0 0 0 0 0 0 0 0 0 0 0
    0 0 0 0 0 0 0 0 0 0 0 0 0 0 0 0 0 0 0 0
```

```
A   17                         IRNA (default from sys$gettim)
B   mass2003.dat
C   rb81.tls
D   rb81_.out
E   rb81.evp
F   rb81_.prt
G    3L M cascade  --  153 MeV 37cl+44ca
H   17,37,20,44,150.0 IZP,IAP,IZT,IAT,ELAB
I   3,0,-1,-1,0,0,0,0,0 JP,JT,IP12,JCN,ITZT,INDPAR,INDIS,AMIX,BMIX
J   99,196,262,7,7,7 KOPTK,IPS1,IPSMAX,NNX,NPX,NAX
K   0,0,0,0,0,0,0,0,0.,1 IZE4,IAE4,JE4,IPE4,EXC4,IZFF,DAF,FFB
L   0.,2.,0. CL0,DIFF,SIGMCN
M   0,2              FTHETA,KOPTLD
N   -1,7.5,15.,7.5,15.,0,0   DALDM,UTR,ULDM,UJTR,UJLDM,KOPTLQ,KOPTEB
O   18.5,1.153,4,0,0,0 Reisdorf Coefficient eshell,r0reis,ipair,dareis,dalpha,dexpo
P   1.25,8.7e-6,2.6e-8 R0LDM,DEF,DEFS-def e def are no more used-use the file defdefs.dat
Q   -1,0,0,0.,0.,0,1.e-5         XYE1,XYM1,XYE2,CJG1,CJG2,XYENH,GMIN
R   0.8,16.0,9.0,0.,0.0,0.0,0.0,0.0,0.0 F1,E1,G1, F2,E2,G2, F3,E3,G3
S   0,0,0,0,0,0    ieop,igop,ifop,fde,fdf
T   0.0003,0.0,0.3,0.04,0.5,0.05   WGR,CGR,CVCBE,CVCB,VK,CVK
U   32,32,64,64.,1.          EXR0,EXH,CJC,LC0,ESTEP
V   60,60,80,1,3,3          KOUTW,KOUTL,KEVAP,KGAMMA,prio,iang
W   1000000000,30,29,2,0,0,0,0,0,0,0    N,JSTP,K0,IG,kp,br,thck,q2d,q2f,q2w,elfact
X   2 3 48 0 4 5 49 0 5 6 50 0 7 8 51 0 8 9 52 0
    9 10 53 0 11 12 54 0 12 13 55 0 13 14 56 0 14 15 57 0
```

```
16 17 58 0 17 18 59 0 18 19 60 0 19 20 61 0 20 21 62 0
22 23 63 0 23 24 64 0 24 25 65 0 25 26 66 0 26 27 67 0
27 28 68 0 197 29 69 0 29 30 70 0 30 31 71 0 31 32 72 0
32 33 73 0 33 34 74 0 34 198 75 0 35 36 76 0 36 37 77 0
37 38 78 0 38 39 79 0 39 40 80 0 40 41 81 0 199 42 82 0
42 43 83 0 43 44 84 0 44 45 85 0 45 46 86 0 46 47 87 0
47 200 88 0 201 202 211 0 202 203 212 0 203 204 213 0 204 205 214 0
205 206 215 0 206 207 216 0 49 50 89 0 51 52 90 0 52 53 91 0
54 55 92 0 55 56 93 0 56 57 94 0 58 59 95 0 59 60 96 0
60 61 97 0 61 62 98 0 63 64 99 0 64 65 100 0 65 66 101 0
66 67 102 0 67 68 103 0 69 70 104 0 70 71 105 0 71 72 106 0
72 73 107 0 73 74 108 0 74 75 109 0 208 76 110 0 76 77 111 0
77 78 112 0 78 79 113 0 79 80 114 0 80 81 115 0 81 209 116 0
82 83 117 0 83 84 118 0 84 85 119 0 85 86 120 0 86 87 121 0
87 88 122 0 210 211 220 0 211 212 221 0 212 213 222 0 213 214 223 0
214 215 224 0 215 216 225 0 216 217 226 0 90 91 123 0 92 93 124 0
93 94 125 0 95 96 126 0 96 97 127 0 97 98 128 0 99 100 129 0
100 101 130 0 101 102 131 0 102 103 132 0 104 105 133 0 105 106 134 0
106 107 135 0 107 108 136 0 108 109 137 0 110 111 138 0 111 112 139 0
112 113 140 0 113 114 141 0 114 115 142 0 115 116 143 0 218 117 144 0
117 118 145 0 118 119 146 0 119 120 147 0 120 121 148 0 121 122 149 0
122 219 150 0 220 221 228 0 221 222 229 0 222 223 230 0 223 224 231 0
224 225 232 0 225 226 233 0 124 125 151 0 126 127 152 0 127 128 153 0
129 130 154 0 130 131 155 0 131 132 156 0 133 134 157 0 134 135 158 0
135 136 159 0 136 137 160 0 138 139 161 0 139 140 162 0 140 141 163 0
141 142 164 0 142 143 165 0 144 145 166 0 145 146 167 0 146 147 168 0
147 148 169 0 148 149 170 0 149 150 171 0 227 228 235 0 228 229 236 0
229 230 237 0 230 231 238 0 231 232 239 0 232 233 240 0 233 234 241 0
152 153 172 0 154 155 173 0 155 156 174 0 157 158 175 0 158 159 176 0
159 160 177 0 161 162 178 0 162 163 179 0 163 164 180 0 164 165 181 0
166 167 182 0 167 168 183 0 168 169 184 0 169 170 185 0 170 171 186 0
235 236 242 0 236 237 243 0 237 238 244 0 238 239 245 0 239 240 246 0
240 241 247 0 173 174 187 0 175 176 188 0 176 177 189 0 178 179 190 0
179 180 191 0 180 181 192 0 182 183 193 0 183 184 194 0 184 185 195 0
185 186 196 0 242 243 248 0 243 244 249 0 244 245 250 0 245 246 251 0
246 247 252 0 188 189 253 0 190 191 254 0 191 192 255 0 193 194 256 0
194 195 257 0 195 196 258 0 248 249 259 0 249 250 260 0 250 251 261 0
251 252 262 0 0 0 0 0 0 0 0 0 0 0 0 0 0 0 0 0
0 0 0 0 0 0 0 0 0 0 0 0 0 0 0 0 0 0 0 0
0 0 0 0 0 0 0 0 0 0 0 0 0 0 0 0 0 0 0 0
0 0 0 0 0 0 0 0 0 0 0 0 0 0 0 0 0 0 0 0
0 0 0 0 0 0 0 0 0 0 0 0 0 0 0 0 0 0 0 0
0 0 0 0 0 0 0 0 0 0 0 0 0 0 0 0 0 0 0 0
0 0 0 0 0 0 0 0 0 0 0 0 0 0 0 0 0 0 0 0
```

```
0 0 0 0 0 0 0 0 0 0 0 0 0 0 0 0 0 0 0 0
0 0 0 0 0 0 0 0 0 0 0 0 0 0 0 0 0 0 0 0
0 0 0 0 0 0 0 0 0 0 0 0 0 0 0 0 0 0 0 0
0 0 0 0 0 0 0 0 0 0 0 0 0 0 0 0 0 0 0 0
0 0 0 0 0 0 0 0 0 0 0 0 0 0 0 0 0 0 0 0
0 0 0 0 0 0 0 0 0 0 0 0 0 0 0 0 0 0 0 0
0 0 0 0 0 0 0 0 0 0 0 0 0 0 0 0 0 0 0 0
0 0 0 0 0 0 0 0 0 0 0 0 0 0 0 0 0 0 0 0
0 0 0 0 0 0 0 0 0 0 0 0 0 0 0 0 0 0 0 0
0 0 0 0 0 0 0 0 0 0 0 0 0 0 0 0 0 0 0 0
0 0 0 0 0 0 0 0 0 0 0 0 0 0 0 0 0 0 0 0
0 0 0 0 0 0 0 0 0 0 0 0 0 0 0 0 0 0 0 0
0 0 0 0 0 0 0 0 0 0 0 0 0 0 0 0 0 0 0 0
0 0 0 0 0 0 0 0 0 0 0 0 0 0 0 0 0 0 0 0
```

Detailed instructions on how to run the CASCADE Monte-Carlo simulation can be found in [85]. We recall here the most important parameters and the ones that have to be modified according to the system under study. In order to easily find them we label the lines with a letter and the columns with a number.

- A1: seed for the random-number generator; Intel-Fortran random-number generator does not work properly with even numbers
- B2: name of the input file with nuclear masses
- E1: name of the event-by-event output file, written in list mode
- H1, H2, H3, H4: Z and A of projectile and target
- H5: beam energy in MeV
- J1, J5, J6: maximum number of decay steps and maximum number of neutrons, protons and α's emitted
- J2, J3: with J1=99, the cascade structure calculated with KASKAD.for is read in; IPS1 and IPSMAX are the number of decaying nuclei and the number of nuclei populated in the cascade (that can be found in *KASK.lst*). In order to read the whole decay cascade up to IPSMAX, the parameter `ipsm` has been incremented from 250 to 280 in the code cascadmc.for. This parameter corresponds to the maximum number of nuclei that can be populated in the decay.
- L1, L2, L3: maximum angular momentum, diffusivity and integral of the CN spin-population cross section; if CLO and SIGMCN are equal to zero, the maximum angular momentum and the total cross section are internally calculated
- N: level density parameterization; H1<0 sets Reisdorf parameterization, H1>0 is used to calculate a=A/H1 in the level density formula (see Eq. 7.4)

- R1, R2, R3: strength, centroid and width of the GDR
- W1: number of Monte-Carlo events
- W2: maximum number of decay steps
- W3: difference between Z of the CN and the final evaporation residue
- X and following: to be copied from KASKAD.dat

C.1 Implementation of reaction kinematics in CASCADE Monte-Carlo

The main output of Monte-Carlo CASCADE simulation is an event file ($*.evp$) written in list mode containing, event by event, the main variables describing the decay cascade. The event file can then be read and sorted with a proper sorting code ($sort\_cascade.f90$). This sorting code has been modified ($sort\_cascade\_AC.f90$) in order to add to each event information on reaction kinematics (in particular the directions of residues and emitted particles).[1]

The reconstruction of the reaction kinematics follows these steps:

- absolute value of the momentum of the emitted particle is calculated from its kinetic energy
- the three components of the momentum of the emitted particle are initialized after a random extraction of the angles θ_{CM} and ϕ_{CM} from a uniform distribution
- the momentum of the particle and of the recoiling nucleus in the center of mass of the emitting source are transformed to the laboratory frame
- the direction (θ_{LAB} and ϕ_{LAB}) of the particle is calculated from the components of its momentum in the laboratory frame
- at the end of the decay cascade, the direction (θ_{LAB} and ϕ_{LAB}) of the fusion-evaporation residue is calculated from the components of its momentum in the laboratory frame

The fraction of the ϕ angle covered by the PHOSWICH array as a function of the polar angle θ (see Fig. 3.11) is read in. For each particle and for the final residue it is compared with a random number extracted from a distribution uniform in the interval [0,1] in order to choose if the residue/particle enters one of the PHOSWICH detectors.

The changes made to the original sorting code are commented in italics within the modified code $sort\_cascade\_AC.f90$ which follows.

---

[1] Of course, it would be more straightforward to include reaction kinematics in the cascademc.for but this would be more time consuming and will give the same result. Actually this option is already implemented but not debugged in our version of cascademc.for.

```
!———————————————— here starts the unpacking part ——————————————————


10        READ(10,END=100,err=100) IPK


!        Reading the event-by-event file.
!
!        Event Structure:
!        - Number of emissions
!        - Not Used
!        - Not Used
!        - A residual Nucleus
!        - Z residual Nucleus
!        - Spin of the compound*2
!        - # of Step + 32*Particle emitted
!        - 0.5 + 10*(Energy of Decay)
!        - 2*(Spin del Figlio)+(Energia del Residuo)
!
!        Decay Types:
!
!         - 1 Neutron
!         - 2 Proton
!         - 3 Alpha
!         - 4 Particle X
!         - 5 Gamma E1
!         - 6 Gamma E2
!         - 7 Yrast
!


    IPK1=1
170 KI=IPK(IPK1)                                        !Number of emissions.

    IF(IPK1.GE.7996) GO TO 10

        nk1 = IPK(IPK1+1)


        ifj = ifj+1
        if (ifj.eq.20) estar = IPK(IPK1+2)
        estar=889
    est(0) = ipk(ipk1+2)
    IMN=IPK(IPK1+3)                                 !A of residual nucleus.
    IZZ=IPK(IPK1+4)                                 !Z of residual nucleus.
    IARRA5=IPK(IPK1+5)                              !2xJ of compound nucleus.

    if (mod(iarra5,2).eq.0) then
         CNS=iarra5/2
        else
         CNS=iarra5/2 + 1
    endif
```

```
CNS5=nint(float(CNS)/5)

residues(Izz,IMN) = residues(Izz,IMN)+1

IF(KI.LE.0.OR.IMN.LE.0.OR.IZZ.LE.0) THEN
      if (mod(float(ipk1),210.).eq.0.) then
       IPK1=IPK1+1
       write (*,*) ' errore irec # KI IMN IZZ',irec,ipk1,KI,IMN,IZZ
       IF(IPK1.GT.8000) GO TO 10
       GO TO 170
      endif
     GO TO 10
END IF

 IPK1=IPK1+6
 IREC=IREC+1

      do I=0,50
       ipar(i) = 0
       cce(i)  = 0
       est(i)  = 0
       caa(i)  = 0
       cab(i)  = 0
      enddo

      do I=1,10
       residue_ok(i) = .true.
      enddo

 NN = 0
      NA = 0
 NP = 0

mom_x_acc=0
mom_y_acc=0
mom_z_acc=0

mom_res_x=0
mom_res_y=0
mom_res_z=mom_res
massa_residuo=CN_MASS
z_residuo=CN_Z

do i=0,50
     alfa_phos(i)=.false.
     p_phos(i)=.false.
     itof(i)=0
enddo
ngamma=0
ngamma5=0
ngamma10=0
p_ev=0
alfa_ev=0
v_res_media=v_res_z
```

```
!     Emission loop -----------------

      DO I=1,KI

            k11 = IPK(IPK1)
            k1 = k11+32000
            k2 = k1/200
            k3 = k1-200*k2
        CAA(I)=float(k3)/2                          ! J of Residual
        CAB(i)= ((k1-k3)/200)/100                 ! J of particle-something is not under control
        CCE(I)=IPK(IPK1+1)/10.                      ! Energy of particle.
        ieking=cce(i_step)
        IF(CCE(I).LT.0.0)CCE(I)=0.1
        ibuff=ipk(ipk1+2)/16
        IPAR(I)= ipk(ipk1+2)-16*ibuff               ! Type of particle emitted.
        Est(i)=float(ipk(ipk1+2)/16)              ! Residual Excitation energy
                                                  ! this is the starting point
                                                  ! for reaction kinematics

        if (ipar(i).eq.1) NN = NN+1
            if (ipar(i).eq.2) NP = NP+1
        if (ipar(i).eq.3) NA = NA+1
        IPK1=IPK1+4



       if (ipar(i).lt.1.or.ipar(i).gt.7) then
        write (*,*) ' Strange Particle ',irec,ipar(i)
           endif

           if (ipar(i).gt.0.and.ipar(i).lt.10) Ipar_spc(ipar(i)) = Ipar_spc(ipar(i)) + 1

      IPAR_SPC(8) = iPAR_SPC(8) + 1

       !beginning of anna insertion


       if(ipar(i).ge.1.and.ipar(i).le.3) then

          massa_residuo=massa_residuo - ipart_s(2,ipar(i))
          z_residuo=z_residuo - ipart_s(1,ipar(i))
       ! Update A and Z of the residue after each emission

          mom_tot=( 2.*float(CCE(I))*float(ipart_s(2,ipar(i))) *float(massa_residuo)
      &/float(ipart_s(2,ipar(i))+massa_residuo) *amu)**0.5
       ! Calculate particle's momentum from kinetic energy CCE(I)

          theta_rand=acos(1-2*ran(iseed))
          phi_rand=ran(iseed)*2*pi
       ! Generate random theta a phi with an uniform distribution
       ! Isotropic emission in CM frame is assumed

          mom_x=mom_tot*sin(theta_rand)*cos(phi_rand)
          mom_y=mom_tot*sin(theta_rand)*sin(phi_rand)
```

```
       mom_z=mom_tot*cos(theta_rand)
  ! Particle's momentum in CM in components

       mom_x_lab=mom_x+mom_res_x*float(ipart_s(2,ipar(i)))/
     &float(massa_residuo + ipart_s(2,ipar(i)))
       mom_y_lab=mom_y+mom_res_y*float(ipart_s(2,ipar(i)))/
     &float(massa_residuo + ipart_s(2,ipar(i)))
       mom_z_lab=mom_z+mom_res_z*float(ipart_s(2,ipar(i)))/
     &float(massa_residuo + ipart_s(2,ipar(i)))

       mom_lab=(mom_x_lab**2.+mom_y_lab**2.+mom_z_lab**2.)**0.5
  ! Particle's momentum in LAB.

       mom_x_acc=mom_x_acc+mom_x_lab
       mom_y_acc=mom_y_acc+mom_y_lab
       mom_z_acc=mom_z_acc+mom_z_lab
  !Accumulators of the momentum of emitted particles

       itof(i)=nint( 160./(mom_lab/(float(ipart_s(2,ipar(i)))*amu)*30.) )
  !particle's ToF in phoswich (160 cm from target)

       theta_lab(i)=acos(mom_z_lab/mom_lab)
       phi_lab(i)=atan(mom_y_lab/mom_x_lab)
  !particle's theta and phi in LAB


       alfa_phosok(i)=.false.
       p_phosok(i)=.false.
       if(theta_lab(i).gt.phosmin.and.theta_lab(i).lt.phosmax) then
 ! theta angle within the angular coverage of phoswich
 ! For each theta, the coverage in phi is give by effiphos(index)
 ! effiphos(index) is read from input "effiphos_out" provided by G.Casini
               index=nint( (theta_lab(i)*180./pi-4.878) / 0.021220812 )
               if(ran(iseed).le.effiphos(index)) then
                       if(ipar(i).eq.3) then
                               alfa_phosok(i)=.true.
                               alfa_ev_int=alfa_ev_int+1
                               alfa_ev=alfa_ev+1
                       else if(ipar(i).eq.2) then
                               p_phosok(i)=.true.
                               p_ev_int=p_ev_int+1
                               p_ev=p_ev+1
                       endif
               endif
       endif
 ! to decide if, for a given theta, the particle entered phoswich compare
 ! a random number between 0 and 1 with effiphos(index)

       if(ipar(i).eq.3) alfa_em=alfa_em+1
       if(ipar(i).eq.2) p_em=p_em+1

       mom_res_x=mom_res_x*float(massa_residuo)/float(massa_residuo+ipart_s(2,ipar(i)))
     &- mom_x
       mom_res_y=mom_res_y*float(massa_residuo)/float(massa_residuo+ipart_s(2,ipar(i)))
```

```
   &- mom_y
      mom_res_z=mom_res_z*float(massa_residuo)/float(massa_residuo+ipart_s(2,ipar(i)))
   &- mom_z

      mom_res_new=(mom_res_x**2.+mom_res_y**2.+mom_res_z**2.)**0.5

   endif

  ENDDO
  ! Here end the loop on the decay cascade

  v_res_new=(v_res_x**2.+v_res_y**2.+v_res_z**2.)**0.5

  v_res_new=mom_res_new/(float(massa_residuo)*amu)
  iv_res_new=nint(v_res_new*500)

  phi_res=atan(mom_res_y/mom_res_x)
  theta_res=acos(mom_res_z/mom_res_new)

  | Compute ToF, and angles for the final residues (emission is instantaneous
  ! on the timescale of residues ToF so we assume that residue moves from
  ! target with the new velocity and direction due to the recoiling process)
  phos_ok=.false.

  if(theta_res.lt.phosmin.or.theta_res.gt.phosmax) go to 55

  index=nint((theta_res*180./pi-4.878)/0.021220812)
  itheta=nint(theta_res*180./pi*5.)
  if(ran(iseed).le.effiphos(index)) then
      phos_ok=.true.
      eff=eff+1
      angdis_res_effphos(itheta)=angdis_res_effphos(itheta)+1
  endif

  ! to decide if, for a given theta, the particle entered phoswich compare
  ! a random number between 0 and 1 with effiphos(index)

55    ......
```

Bibliography

[1] Wieland, O., Bracco, A., Camera, F., Benzoni, G., Blasi, N., Brambilla, S., Crespi, F., Giussani, A., Leoni, S., Mason, P., Million, B., Moroni, A., Barlini, S., Kravchuk, V. L., Gramegna, F., Lanchais, A., Mastinu, P., Maj, A., Brekiesz, M., Kmiecik, M., Bruno, M., Geraci, E., Vannini, G., Casini, G., Chiari, M., Nannini, A., and Ordine, A. *Phys. Rev. Lett.* **97**, 012501 (2006).

[2] Bini, M., Casini, G., Olmi, A., Poggi, G., Stefanini, A. A., Bardelli, L., Bartoli, A., Bidini, L., Coppi, C., Carmine, P. D., Mangiarotti, A., Maurenzig, P. R., Pasquali, G., Piantelli, S., Poggi, S., Taccetti, N., and Vanzi, E. *Nucl. Instr. Meth. Phys. Res. A* **515**, 497 (2003).

[3] Gramegna, F., Abbondanno, U., Andreano, A., Bassini, R., Bonutti, F., Bruno, M., Casini, G., D'Agostino, M., Manzin, G., Margagliotti, G. V., Mastinu, P. F., Milazzo, P. M., Moroni, A., Squarcini, M., Tonetto, F., Vannini, G., and Vannucci, L. *Nucl. Instr. Meth. Phys. Res. A* **389**, 474 (1997).

[4] Pühlhofer, F. *Nucl. Phys. A* **280**, 267 (1977).

[5] Bortignon, P. F., Braguti, M., Brink, D. M., Broglia, R. A., Brusati, C., Camera, F., Cassing, W., Cavinato, M., Giovanardi, N., and Gulminelli, F. *Nucl. Phys. A* **583**, 101 (1995). Nucleus-Nucleus Collisions.

[6] Baran, V., Cabibbo, M., Colonna, M., Di Toro, M., and Tsoneva, N. *Nucl. Phys. A* **679**, 373 (2001).

[7] Baran, V., Brink, D. M., Colonna, M., and Di Toro, M. *Phys. Rev. Lett.* **87**, 182501 (2001).

[8] Baran, V., Rizzo, C., Colonna, M., Di Toro, M., and Pierroutsakou, D. *Phys. Rev. C* **79**, 021603 (2009).

[9] Harakeh, M. N., Dowell, D. H., Feldman, G., Garman, E. F., Loveman, R., Osborne, J. L., and Snover, K. A. *Phys. Lett. B* **176**, 297 (1986).

[10] Behr, J. A., Snover, K. A., Gossett, C. A., Kiciǹska-Habior, M., Gundlach, J. H., Drebi, Z. M., Kaplan, M. S., and Wells, D. P. *Phys. Rev. Lett.* **70**, 3201 (1993).

[11] Harney, H. L., Richter, A., and Weidenmüller, H. A. *Rew. Mod. Phys.* **58**, 607 (1986).

[12] Sagawa, H., Bortignon, P. F., and Colò, G. *Phys. Lett. B* **444**, 1 (1998).

[13] Kicin̂ska-Habior, M. *Nucl. Phys. A* **36**, 1133 (2005).

[14] Bass, R. *Nucl. Phys. A* **231**, 45 (1974).

[15] Cohen, S., Plasil, F., and Swiatecki, W. J. *Ann. Phys.* **82**, 557 (1974).

[16] Flibotte, S., Chomaz, P., Colonna, M., Cromaz, M., DeGraaf, J., Drake, T. E., Galindo-Uribarri, A., Janzen, V. P., Jonkman, J., Marshall, S. W., Mullins, S. M., Nieminen, J. M., Radford, D. C., Rodriguez, J. L., Waddington, J. C., Ward, D., and Wilson, J. N. *Phys. Rev. Lett.* **77**, 1448 (1996).

[17] Cinausero, M., Gelli, N., Viesti, G., and Lucarelli, F. *Il Nuovo Cimento* **111**, 613 (1998).

[18] Pierroutsakou, D., Martin, B., Inglima, G., Boiano, A., Rosa, A. D., Di Pietro, M., La Commara, M., Mordente, R., Romoli, M., Sandoli, M., Trotta, M., Vardaci, E., Glodariu, T., Mazzocco, M., Signorini, C., Stroe, L., Baran, V., Colonna, M., Di Toro, M., and Pellegriti, N. *Phys. Rev. C* **71**, 054605 (2005).

[19] Martin, B., Pierroutsakou, D., Agodi, C., Alba, R., Baran, V., Boiano, A., Cardella, G., Colonna, M., Coniglione, R., De Filippo, E., Del Zoppo, A., Di Toro, M., Inglima, G., Glodariu, T., La Commara, M., Maiolino, C., Mazzocco, M., Pagano, A., Piattelli, P., Pirrone, S., Rizzo, C., Romoli, M., Sandoli, M., Santonocito, D., Sapienza, P., and Signorini, C. *Phys. Lett. B* **664**, 47 (2008).

[20] Pierroutsakou, D., Martin, B., Agodi, C., Alba, R., Baran, V., Boiano, A., Cardella, G., Colonna, M., Coniglione, R., De Filippo, E., Del Zoppo, A., Di Toro, M., Inglima, G., Glodariu, T., La Commara, M., Maiolino, C., Mazzocco, M., Pagano, A., Parascandolo, C., Piattelli, P., Pirrone, S., Rizzo, C., Romoli, M., Sandoli, M., Santonocito, D., Sapienza, P., and Signorini, C. *Phys. Rev. C* **80**, 024612 (2009).

[21] Corsi, A., Wieland, O., Kravchuk, V. L., Bracco, A., Camera, F., Benzoni, G., Blasi, N., Brambilla, S., Crespi, F. C. L., Giussani, A., Leoni, S., Million, B., Montanari, D., Moroni, A., Gramegna, F., Lanchais, A., Mastinu, P., Brekiesz, M., Kmiecik, M., Maj, A., Bruno, M., D'Agostino, M., Geraci, E., Vannini, G., Barlini, S., Casini, G., Chiari, M., Nannini, A., Ordine, A., Di Toro, M., Rizzo, C., Colonna, M., and Baran, V. *Phys. Lett. B* **679**, 197 (2009).

[22] Simenel, C., Chomaz, P., and de France, G. *Phys. Rev. Lett.* **86**, 2971 (2001).

[23] Simenel, C., Chomaz, P., and de France, G. *Phys. Rev. C* **76**, 024609 (2007).

[24] Papa, M., Tian, W., Giuliani, G., Amorini, F., Cardella, G., Di Pietro, A., Figuera, P. P., Lanzalone, G., Pirrone, S., Rizzo, F., and Santonocito, D. *Phys. Rev. C* **72**, 064608 (2005).

[25] Li, G. Q. and Machleidt, R. *Phys. Rev. C* **48**, 1702 (1993).

[26] Li, G. Q. and Machleidt, R. *Phys. Rev. C* **49**, 566 (1994).

[27] Jackson, J. D. *Classical Electrodynamics.* Wiley, (1962).

[28] Rizzo, C., Baran, V., Colonna, M., Corsi, A., and Di Toro, M. (2010). arXiv:1010.2927v1.

[29] Baran, V., Colonna, M., Greco, V., and Di Toro, M. *Phys. Rep.* **410**, 335 (2005).

[30] Auerbach, N., Hüfner, J., Kerman, A. K., and Shakin, C. M. *Phys. Rev. Lett.* **23**, 484 (1969).

[31] Wilkinson, D. H. *Phil. Mag.* **1**, 379 (1956).

[32] Behr, J. A. *Giant Dipole Radiation and Isospin Purity in Highly Excited Compound Nuclei.* PhD thesis, University of Washington, (1991).

[33] Bohr, A. and Mottelson, B. *Nuclear Structure I.* (W.A. Benjamin, Inc., New York, 1969).

[34] Hamamoto, I. and Sagawa, H. *Phys. Rev. C* **48**, R960 (1993).

[35] Dobaczewski, J. and Hamamoto, I. *Phys. Lett. B* **345**, 181 (1995).

[36] Colò, G., Nagarajan, M. A., Van Isacker, P., and Vitturi, A. *Phys. Rev. C* **52**, R1175 (1995).

[37] Satuła, W., Dobaczewski, J., Nazarewicz, W., and Rafalski, M. *Phys. Rev. Lett.* **103**, 012502 (2009).

[38] Suzuki, T., Sagawa, H., and Colò, G. *Phys. Rev. C* **54**, 2954 (1996).

[39] Harakeh, M. N. and van der Woude, A. *Giant Resonances.* Oxford University Press, (2001).

[40] Jänecke, J., Harakeh, M. N., and van der Werf, S. Y. *Nucl. Phys. A* **463**, 571 (1987).

[41] Mottelson, B. *Elementary features of nuclear structure, Les Houches, Session LXVI, 1996.* Elsevier, (1998).

[42] Morrissey, D. J., Benenson, W., and Friedman, W. A. *Ann. Rev. Nucl. Part. Sci.* **44**, 27 (1994).

[43] Reisdorf, W. *Z. Phys. A* **300**, 227 (1981).

[44] Diószegi, I., Mazumdar, I., Shaw, N. P., and Paul, P. *Phys. Rev. C* **63**, 047601 (2001).

[45] Wójcik, E., Kicìnska-Habior, M., Kijewska, O., Kowalczyk, M., Kisielìnski, M., and Choìnski, J. *Acta Phys. Pol. B* **37**, 207 (2006).

[46] Wójcik, E., Kiciǹska-Habior, M., Kijewska, O., Kowalczyk, M., Kisieliǹski, M., and Choiǹski, J. *Acta Phys. Pol. B* **38**, 1496 (2007).

[47] Farnea, E., de Angelis, G., Gadea, A., Bizzeti, P. G., Dewald, A., Eberth, J., Algora, A., Axiotis, M., Bazzacco, D., Bizzeti-Sona, A. M., Brandolini, F., Colò, G., Gelletly, W., Kaci, M. A., Kintz, N., Klug, T., Kröll, T., Lenzi, S. M., Lunardi, S., Marginean, N., Martinez, T., Menegazzo, R., Napoli, D. R., Nyberg, J., Pavan, P., Podolyák, Z., Petrache, C. M., Quintana, B., Rubio, B., Spolaore, P., Steinhardt, T., Tain, J. L., Thelen, O., Ur, C. A., Venturelli, R., and Weiszflog, M. *Phys. Lett. B* **551**, 56 (2003).

[48] Berman, B. L. and Fultz, S. C. *Rev. Mod. Phys.* **47**, 713 (1975).

[49] Vergados, J. D. *Nucl. Phys. A* **239**, 271 (1975).

[50] Akyüz, R. O. and Fallieros, S. *Phys. Rev. Lett.* **27**, 1016 (1971).

[51] Gaardhøje, J. J. *Ann. Rev. Nucl. Part. Sci.* **42**, 483 (1992).

[52] Newton, J. O., Herskind, B., Diamond, R. M., Dines, E. L., Draper, J. E., Lindenberger, K. H., Schück, C., Shih, S., and Stephens, F. S. *Phys. Rev. Lett.* **46**, 1383 (1981).

[53] Kelly, M. P., Snover, K. A., van Schagen, J. P. S., Kiciǹska-Habior, M., and Trznadel, Z. *Phys. Rev. Lett.* **82**, 3404 (1999).

[54] Mattiuzzi, M., Bracco, A., Camera, F., Ormand, W. E., Gaardhøje, J. J., Maj, A., Million, B., Pignanelli, M., and Tveter, T. *Nucl. Phys. A* **612**, 262 (1997).

[55] Bracco, A., Camera, F., Wieland, O., and Ormand, E. *Mod. Phys. Lett. A* **97**, 2479 (2007).

[56] Chomaz, P. *Phys. Lett. B* **347**, 1 (1995).

[57] Kusnezov, D., Alhassid, Y., and Snover, K. A. *Nucl. Phys. A* **649**, 193 (1999).

[58] GEANT3, (2010). `http://wwwasd.web.cern.ch/wwwasd/geant/`.

[59] Bardelli, L., Poggi, G., Bini, M., and Pasquali, G. *Nucl. Instr. Meth. Phys. Res. A* **572**, 882 (2007).

[60] Pasquali, G., Ciaranfi, R., Bardelli, L., Bini, M., Boiano, A., Giannelli, F., Ordine, A., and Poggi, G. *Nucl. Instr. Meth. Phys. Res. A* **570**, 126 (2007).

[61] Bardelli, L., Bini, M., Poggi, G., and Taccetti, N. *Nucl. Instr. Meth. Phys. Res. A* **491**, 244 (2002).

[62] Casini, G., (2010). Private communication.

[63] Bardelli, L. A ROOT-based data-monitor software for the GARFIELD experiment, LNL Ann. Rep. 2007.

[64] Fotina, O., Kravchuk, V., Barlini, S., Gramegna, F., Eremenko, D., Parfenova, Y., Platonov, S., Yuminov, O., Bruno, M., DAgostino, M., Casini, G., Wieland, O., Bracco, A., and Camera, F. *Phys. At. Nuclei* **73**, 1317.

[65] Cabrera, J., Keutgen, T., El Masri, Y., Dufauquez, C., Roberfroid, V., Tilquin, I., Van Mol, J., Régimbart, R., Charity, R. J., Natowitz, J. B., Hagel, K., Wada, R., and Hinde, D. J. *Phys. Rev. C* **68**, 034613 (2003).

[66] Tarasov, O. B. and Bazin, D. *Nucl. Instr. Met. Phys. Res. B* **204**, 174 (2003).

[67] LISE++, (2010). `http://groups.nscl.msu.edu/lise/lise.html`.

[68] Mazurek, K., (2010). `http://jacobi.ifj.edu.pl/~mazurek/2/index_yrast.php`.

[69] Pomorski, K. and Dudek, J. *Phys. Rev. C* **67**, 044316 (2003).

[70] Kicin̉ska-Habior, M., Snover, K. A., Behr, J. A., Feldman, G., Gossett, C. A., and Gundlach, J. H. *Phys. Rev. C* **41**, 2075 (1990).

[71] Schiller, A., Thoennessen, M., and McAlpine, K. M. *Nucl. Phys. A* **788**, 231c (2007).

[72] Gaudefroy, L., Obertelli, A., Péru, S., Pillet, N., Hilaire, S., Delaroche, J. P., Girod, M., and Libert, J. *Phys. Rev. C* **80**, 064313 (2009).

[73] ROOT, (2010). `http://root.cern.ch/drupal/`.

[74] Morelli, L., Bruno, M., Baiocco, G., Bardelli, L., Barlini, S., Bini, M., Casini, G., D'Agostino, M., Degerlier, M., Gramegna, F., Kravchuk, V. L., Marchi, T., Pasquali, G., and Poggi, G. *Nucl. Instr. Meth. Phys. Res. A* **620**, 305 (2010).

[75] Abbondanno, U., Bruno, M., Casini, G., Cavaletti, R., Cavallaro, S., Chiari, M., D'Agostino, M., Gramegna, F., Lanchais, A., Margagliotti, G. V., Mastinu, P. F., Milazzo, P. M., Moroni, A., Nannini, A., Ordine, A., Vannini, G., and Vannucci, L. *Nucl. Instr. Meth. Phys. Res. A* **488**, 604 (2002).

[76] Nicolini, R., (2008). Peaks fitting manual.

[77] Janecke, J. *Isospin in nuclear physics. Systematics of Coulomb energies and excitation energies of isobaric analog states.* North-Holland Publishing Company, (1969).

[78] Kailas, S., Saini, S., Mehta, M., Veerabahu, N., Viyogi, Y., and Ganguly, N. *Nucl. Phys. A* **315**, 157 (1979).

[79] Raman, S., Malarkey, C. H., Milner, W. T., Nestor, C. W., and Stelson, P. H. *At. Data Nucl. Data Tab.* **36**, 1 (1987).

[80] Lister, C. J., Campbell, M., Chishti, A. A., Gelletly, W., Goettig, L., Moscrop, R., Varley, B. J., James, A. N., Morrison, T., Price, H. G., Simpson, J., Connel, K., and Skeppstedt, O. *Phys. Rev. Lett.* **59**, 1270 (1987).

[81] MacDonald, W. M. and Birse, M. C. *Phys. Rev. C* **29**, 425 (1984).

[82] Hofman, D. J. and Diószegi, I., (1999). Program CASSCIS input description.

[83] Herman, M. G., (1989). CASCADE.

[84] AME2003 `http://www.nea.fr/dbdata/data/structure.htm#masses`.

[85] Casati, P., (2009). Bachelor's Thesis, University of Milano.